

Characterization of Online Graphene Oxide and Reduced Graphene Oxide using optical diagnostics

by

Horace Ingram Looi

A thesis

presented to the University of Waterloo

in fulfillment of the

thesis requirement for the degree of

Master of Applied Science

in

Mechanical and Mechatronics Engineering (Nano)

Waterloo, Ontario, Canada, 2025

©Horace Ingram Looi 2025

Author's declaration

This thesis consists of material all of which I authored or co-authored: see Statement of Contributions included in the thesis. This is a true copy of the thesis, including any final revisions, as accepted by my examiners.

I understand that my thesis may be made electronically available to the public.

Statement of Contributions

Chapter 4 and 5 of this thesis consists of a paper that was co-authored by myself, Mr. Halil Ibrahim Yazici, Dr. Joel C. Corbin, Dr. Rym Mehri, Dr. Timothy Sipkens and Dr. Kyle Daun, my supervisor. Mr. Yazici and I worked with Dr. Corbin and Dr. Mehri to determine the methodology used as described in Chapter 4. Mr. Yazici and I worked together to implement the method and analyze the data from the experimental methods. Dr. Sipkens assisted with figure generation and analysis methods.

Abstract

Graphene is a promising nanomaterial due to its high electron mobility, large specific surface area, high thermal conductivity, high tensile strength, and flexibility. In electrical applications, pristine single-layer graphene (PG) offers superior properties compared to conventional materials in semi conductors, supercapacitors and batteries. However, since PG is difficult to manufacture at an industrial scale, there is a need for a graphene-like material that is amenable to high yield production. A promising candidate is the thermal reduction of graphene oxide (GO) into reduced graphene oxide (rGO), which allows for high throughput of material while minimizing human intervention. However, the properties of rGO are heavily dependent on the quality of incoming GO and the resulting morphology and composition of the rGO. Therefore, a method to measure the GO and rGO properties in real time is needed. Time-resolved laser-induced incandescence (TiRe-LII) and line-of-sight attenuation (LOSA) are two absorption-based measurements that are commonly used to characterize soot and other nanomaterials in real time. Consequently, these methods are thought to have high potential in characterizing GO and rGO.

In this work, *ex situ* methods were used to provide morphological and optical characteristics of GO. Additionally, TiRe-LII and LOSA testing were performed to assess their capabilities in measuring GO and rGO in real-time. The results show that TiRe-LII is capable of providing the relative specific surface area (SSA) of rGO, with accurate SSA trends and slight deviations in absolute value compared to *ex situ* testing. However, GO showed no incandescent signals due to its low absorption characteristics. LOSA testing showed that, by applying the Lorentz-Drude model, the electrical conductivity and degree of reduction of GO and rGO could be derived. The results indicated that the derived electrical conductivity matched expected trends and were similar in magnitude to literature results. This study found that TiRe-LII can be used to derive the SSA of rGO, and LOSA can be used to derive the electrical conductivity of GO and rGO, both in real time.

Acknowledgements

I would like to sincerely thank my supervisor, Dr. Kyle Daun, for introducing me to this project and letting me work on such an exciting topic with wonderful people. I am forever grateful for your patience and kindness in helping me with my many mistakes, whether during writing or research. I would not be the researcher that I am today without your support, and I am certain I will carry the skills I have learned from you and this project to any future work I undertake.

Additionally, I would like to thank all the researchers at the National Research Council of Canada. Dr. Joel Corbin, Dr. Rym Mehri, Dr. Tim Sipkens, Brett Smith, and Simon-Alexandre Lussier, I truly appreciated your expertise and guidance during my research stay, as well as your accommodation and hospitality. Joel, Rym, and Tim, your input and guidance on the *ex situ* characterization study we conducted together were invaluable. Tim, in particular, thank you for all your help in designing the plots and figures, I came out of this thesis with a much better picture of how to present scientific work, and I attributed that largely to you.

I would like to thank Dr. Michael Pope and Sarah Jankhani for all their help during this work. Sharing your equipment and allowing us to work on your rGO tube furnace reduction system made this project possible. I truly appreciated all the feedback the two of you provided, which helped to address any gaps in my chemistry knowledge. Working and collaborating together has made my work much more insightful.

I would like to thank Dr. Christof Schulz, Dr. Torsten Endres, and Mohamed Elashry for being so welcoming during my stay at the University of Duisburg-Essen (UDE). I learned a great deal from the amazing research team at UDE and greatly appreciate the opportunity to use the available equipment. A special thanks to Mohamed, who was patient and accommodating, when assisting me in running experiments and analyzing the data. I am grateful for your time and the expertise you shared with me while operating the plasma reactor.

I would like to thank all my wonderful colleagues at the Waterloo Laboratory for Inverse Analysis and Thermal Science (WatLIT): Ardhendu Shekhar Bahattacharya, Daniel Blackmore, Stephen Robinson-Enebeli, Ornel Padilla Estrada, Dr. Paule Lapeyre, Michiyo Kagaya, Nishant Sriram Narayanan, Avery Opalka, Arpan Singh, Mu-An Tsai, Fatima Suleiman, Jun Wang, and Halil Ibrahim Yazici. Thank you for all the laughs and continuous support. I could not imagine a better team/group to work with. In particular, I would like to thank Stephen and Halil, your expertise and patience were incredibly helpful when I first started in this role and have continued to help me throughout. Stephen, thank you for helping me familiarize myself with the TiRe-LII system. Your suggestions and advice for addressing any experimental hiccups were always appreciated. Halil, thank you for your assistance and support during this work. The studies we conducted together were always enhanced by your expertise and professionalism.

I would like to thank my committee members, Dr. Michael Pope and Dr. XiaoYu Wu, for their comprehensive feedback. Your questions and comments were greatly appreciated.

I am very thankful for the funding bodies: National Science and Engineering Research Council (NSERC), Scalable 2D-Materials Architectures (2D MATURE), National Research Council of Canada (NRC) for your generosity in funding this project.

Finally, I am deeply grateful to my family and partner for supporting me throughout this entire journey. Thank you to my parents, Cindy and Danny, for always cheering me on and helping in any way you could. Thank you to my brother, Jonathan, for always being there when I needed someone to talk to and for teaching me to strive for better. Thank you to my partner, Chantelle, for being there whenever I had a busy day and needed a friend. Thank you all, your continuous love and support were invaluable during this work.

Table of contents

Author's declaration	ii
Statement of Contributions	iii
Abstract.....	iv
Acknowledgements	v
List of figures.....	x
List of tables.....	xiv
Nomenclature	xv
Chapter 1 Introduction to reduced graphene oxide, and optical diagnostic techniques	1
1.1 Motivation.....	1
1.2 Literature review	3
1.2.1 GO and rGO synthesis	3
1.2.2 TiRe-LII analysis.....	6
1.2.3 LOSA Measurements	9
1.3 Present Work	10
Chapter 2 TiRe-LII and LOSA Theory and Modelling.....	13
2.1 Time-resolved laser-induced incandescence analysis	13
2.1.1 Optical Pyrometry	15
2.1.2 Conduction Heat Transfer	19
2.1.3 Specific Surface Area Analysis	23
2.2 Line-of-Sight Attenuation Analysis.....	25
2.3 Summary	28
Chapter 3 Reduced graphene oxide, TiRe-LII, and LOSA experimental apparatuses	30
3.1 In-line synthesis of reduced graphene oxide.....	30
3.1.1 Synthesis of graphene oxide.....	30
3.1.2 Thermal reduction to rGO.....	32
3.2 TiRe-LII four colour experimental apparatus	34
3.2.1 TiRe-LII excitation system.....	35
3.2.2 TiRe-LII detection apparatus.....	39
3.3 Plasma reactor-LOSA experimental apparatus.....	43
3.4 Summary	46
Chapter 4 GO ex-situ characterization experimental methods	48
4.1 Preparation and nebulization of GO particles	48
4.1.1 Preparation of GO particles.....	48
4.1.2 Nebulization of GO particles	49
4.2 Ex-situ experimental methods.....	50

4.2.1 Morphological analysis	50
4.2.2 Optical analysis	54
4.3 Summary	60
Chapter 5 GO ex-situ results and analysis.....	61
5.1 Particle morphology	61
5.1.1 TEM results.....	61
5.1.2 Mobility diameter distribution	62
5.1.3 Effective density and mass mobility exponent.....	63
5.2 Particle optical characteristics results and discussion	66
5.2.1 Spectral absorption coefficient and absorption Ångström exponent.....	66
5.2.2 Mass absorption cross-section and Mass scattering cross-section	68
5.2.3 TiRe-LII validation and verification	71
5.3 Summary	75
Chapter 6 Online TiRe-LII characterization of thermal reduction of rGO	77
6.1 Experimental set-up	77
6.1.1 Tube furnace and LII system integration	77
6.1.2 Experimental procedures.....	79
6.1.3 BET-SSA measurements	81
6.2 SSA results and discussion.....	82
6.2.1 TiRe-LII results.....	82
6.2.2 BET-SSA results.....	87
6.3 Summary	89
Chapter 7 Online extinction characterization of plasma reduction of rGO	91
7.1 Experimental Set-up.....	91
7.1.1 Gas-phase LOSA measurements.....	91
7.1.2 Colloidal UV-Vis spectroscopic analysis	93
7.1.3 Lorentz-Drude modelling.....	95
7.2 Results and discussion	97
7.2.1 LOSA online measurement	97
7.2.2 Colloidal UV-Vis spectroscopic measurement.....	99
7.2.3 Lorentz-Drude model validation	102
7.3 Summary	109
Chapter 8 Conclusions and Future work.....	111
8.1 Summary and conclusions	111
8.2 Future Work	115
8.2.1 TiRe-LII improvements.....	115
8.2.2 LOSA improvements.....	116
8.2.3 Additional diagnostics	117
8.3 Impact	117
References.....	119
Appendices.....	131
Appendix A Calibration Procedures.....	132
A.1 TiRe-LII relative calibration.....	132
A.1.1 Calibration procedure	132
A.1.2 Gülder burner fabrication	139

A.1.3 Calibration constants validation	141
A.2 LOSA calibration.....	144
Appendix B.....	146
B.1 Effective density calibration.....	146
B.2 Vertical error bar determination.....	147

List of figures

Figure 1-1: Schematic of standard TiRe-LII operation	7
Figure 1-2: Schematic of standard LOSA operation	10
Figure 2-1: Visual representation of heating and cooling process of nanoparticle	15
Figure 2-2: Heat conduction as defined by three regimes: free molecular, transition, and continuum [78]	20
Figure 2-3: Schematic of Boundary Sphere Method (Fuchs's Method)	23
Figure 2-4: Linear regression of TiRe-LII conduction cooling [71]	24
Figure 2-5: Visual representation of Lorentz-Drude model	28
Figure 3-1: Evolution of SSA for a) crumpled GO particles and b) sheet-like GO throughout processing conditions: heating, solution processing, and mechanical compression [14]	31
Figure 3-2: Schematic of GO powder synthesis: Note (1) is not currently used but can be used to connect to tube furnace reduction in the future	32
Figure 3-3: Schematic of Dry Nebulizer Fan	33
Figure 3-4: Physical image of the nebulizer	33
Figure 3-5: Schematic for thermal reduction	34
Figure 3-6: Schematic of excitation system of TiRe-LII	35
Figure 3-7: Physical image of the LII detection set-up	36
Figure 3-8: Laser temporal profile [74]	37
Figure 3-9: Aerosol Sample Cell: Side and Top View	38
Figure 3-10: Three-colour LII detection apparatus [74]	39
Figure 3-11: Schematic of PMT [94]	40
Figure 3-12: a) schematic of PMT tube housing. b) schematic of full detection apparatus	41
Figure 3-13: Physical image of LII detection system	42
Figure 3-14: Plasma-synthesized rGO on collection filter	43
Figure 3-15: a) Glowing plasma of Ar/H ₂ b) Schematic of plasma reactor [73]	44

Figure 3-16: Schematic of Plasma-LOSA optical setup. LDLS: laser-drive light source, PM: Parabolic Mirror (effective focal length 50mm), A = Apertures, B = Plano-convex lens (focal length 50mm), M = 90° mirror, IS = integrating sphere, A = aperture, C = Plano-convex lens (focal length 300 mm), D = Plano-convex lens (focal length 100 mm), E = Plano-convex lens (focal length 150 mm). Spectrograph used is a IsoPlane SCT 320.....	45
Figure 3-17: EMCCD colourmap of wavelength vs y-pixels in terms of intensity (counts)	46
Figure 4-1: a) GO powder after spray drying and b) GO colloid after the powder is dispersed in water...	49
Figure 4-2: Nebulization apparatus of GO particles	50
Figure 4-3: TEM present in University of Waterloo [105]	51
Figure 4-4: Schematic of mobility diameter distribution study.....	52
Figure 4-5: Schematic of effective density measurement apparatus.....	53
Figure 4-6: Schematic of absolute absorption coefficient at 450nm measurement (CAPS PM _{SSA, 450nm}) ...	55
Figure 4-7: Schematic of spectral absorption coefficient measurement (Aethalometer).....	56
Figure 4-8: Schematic of mass absorption cross-section measurement (CERMS).....	57
Figure 4-9: Schematic of LII 300 internal workings.....	59
Figure 4-10: Schematic of LII-300 experimental procedure.....	60
Figure 5-1: TEM image of (a) multiple GO particles, (b) higher magnification of a single GO particle, (c) diffraction pattern from the GO particle	62
Figure 5-2: Mobility diameter vs number concentration for aqueous aerosolized GO colloid in water.....	63
Figure 5-3: Effective density vs mobility diameter of aqueous aerosolized GO: One-dimensional plot with the average effective density.....	65
Figure 5-4: Effective density vs mobility diameter of aqueous aerosolized GO: Two-dimensional distribution with ellipses representing standard deviation from the mean bivariate fit (yellow: this study, white: M9 soot data from Trivanovic et al. [108]	66
Figure 5-5: Normalized wavelength-resolved absorption coefficient vs wavelength of nebulized GO	67

Figure 5-6: MAC at 450nm vs average single particle mass + fitted data using Mie Theory and Rayleigh theory	70
Figure 5-7: MSC at 450nm vs average single particle mass + fitted data using Mie Theory and Rayleigh theory	71
Figure 5-8: Temporal evolution of pyrometric temperature and signal intensity of GO.....	72
Figure 5-9: Mobility diameter distribution during LII-300 experiment.....	73
Figure 5-10: Temporal evolution of normalized temperature for GO, rGO, FLG, and Soot [58]	75
Figure 6-1: Schematic of tube furnace & TiRe-LII set-up. Note, the probe volume is connected to the rest of the system described in Figure 3-6.	78
Figure 6-2: Physical image of tube furnace & TiRe-LII set-up	78
Figure 6-3: TEM images of drop cast tube furnace synthesized rGO.....	80
Figure 6-4: Schematic of the Gemini VII 2390a [146]	81
Figure 6-5: Pyrometrically determined temperatures for all five experiments	83
Figure 6-6: Linear regression of $\ln[\theta(t)]$ vs time	84
Figure 6-7: LII-inferred SSA vs Reduction temperature.....	87
Figure 6-8: SSA vs Reduction temperature comparing TiRe-LII and BET derived results.....	89
Figure 7-1: Image of heated aerosol flow through plasma reactor	92
Figure 7-2: rGO colloids after different reduction durations	94
Figure 7-3: Raw intensity images of the four settings: L1P0 (LDLS unblocked, gas only), L0P0 (LDLS blocked, gas only), L1P1 (LDLS unblocked, GO aerosol), L0P1 (LDLS blocked, GO aerosol).....	97
Figure 7-4: Spectral Absorbance plot derived from LOSA of rGO	98
Figure 7-5: Spectral absorbance plot comparing binned data to experimental data – 60 min reduction time	100
Figure 7-6: Spectral absorbance of GO after different reduction durations: a) from this experiment b) presented by Li et al. [140]	101
Figure 7-7: Comparison of experimental data vs Lorentz-Drude fit: a) GO (0 min) b) rGO (60 min).....	103

Figure 7-8: Normal distribution of the six fitted parameters with a 95% credibility interval - GO (0 min reduction duration).....	105
Figure 7-9: Normal distribution of the six fitted parameters with a 95% credibility interval - rGO (60 min reduction duration).....	106
Figure 7-10: Spectral electrical conductivity for rGO (60 min reduction duration)	107
Figure 7-11: DC conductivity versus reduction duration.....	109
Figure 8-1: Schematic of in situ and online diagnostics of rGO synthesis	115
Figure A-1: Schematic of calibration setup.....	134
Figure A-2: Physical image of calibration setup.....	134
Figure A-3: Measured voltage vs gain for PMT 1 – Halogen-Tungsten lamp.....	137
Figure A-4: Measured voltage vs gain with different ND filters applied.....	138
Figure A-5: Measured voltage vs gain for PMT 1 - LDLS	138
Figure A-6: Technical drawing of the burner.....	140
Figure A-7: Physical image of Gülder Burner	141
Figure A-8: Maximum temperature vs fluence: Gray solid line and open circles are studies at 1064 nm [167].....	142
Figure A-9: Maximum temperature vs Fluence: Halogen-Tungsten Lamp vs LDLS.....	144
Figure A-10: Pixel image of pen-ray lamp.....	145
Figure B-1: Fitted Santovac calibration curve	146

List of tables

Table 1: Gain values for each PMT	79
Table 2: Derived Lorenz-Drude Parameters	103
Table A-1 PMT maximum output voltage ratings.....	133
Table A-2: PMT naming convention.....	136
Table A-3: Calibration constants derived at each PMT – Halogen-Tungsten lamp	137
Table A-4: Calibration constants derived at each PMT – LDLS.....	139
Table A-5: ND filter constants	142

Nomenclature

This section provides a summary of the nomenclature used in this thesis. There are overlapping symbols with are differentiated by subscripts and superscripts which help to specify the definition.

Latin characters

Symbol	Unit	Definition
A	-	Absorbance
A_{cond}	m^2	Conduction particle surface area
A_g	-	Gain exponential constant
a_s	-	Scattering coefficient
b_s	-	Scattering coefficient
C	-	Calibration constant
C_{abs}	m^2	Absorption cross-section
C_n	-	Nuisance parameter
c_g	m/s	Mean thermal speed of a gas
c_p	$\text{J}/(\text{kg}\cdot\text{K})$	Specific heat capacity
D	-	Intensity calibration factor
D^{ref}	-	Relative intensity calibration factor
d_p	m	Particle diameter
d_m	m	Mobility diameter
d_{ve}	m	Volume-equivalent diameter
$E(m_\lambda)$	-	Spectral absorption function
E_0	J	Pre-collision energy

E_i	J	Post-collision energy
E^{ref}	W/m ²	Irradiance of reference light source
e	C	Charge of an electron
$F(m_\lambda)$	-	Spectral scattering function
$F(t)$	-	Laser temporal profile
F_0	J/cm ²	Laser fluence
G	-	Gain correction factor
ΔH_v	J/mol	Molar latent heat of vaporization
h	J·s	Planck's constant
I_λ	W/(m ² ·μm)	Transmitted spectral light intensity
$I_\lambda(0)$	W/(m ² ·μm)	Incident spectral light intensity
$I_{\lambda,b}$	W/(m ² ·μm)	Blackbody spectral light intensity
J_f	-	Jacobian for Lorentz-Drude fit
J_{corr}	-	Corrected intensity signal
J_{exp}	-	Experimentally determined intensity signal
J_{mod}	-	Modelled intensity signal
k	W/(m·K)	Thermal conductivity
k_λ	-	Imaginary component of the complex index of refraction
k_B	(m ² ·kg)/(s ² ·K)	Boltzmann's constant
k_c	-	Mass mobility pre-factor
\bar{k}	W/(m·K)	Average thermal conductivity
Kn	-	Knudsen number
L	m	Characteristic length

l_0	m	Mean free path of conduction electrons
M	kg/m ³	Mass concentration
m^*	kg/C	Mass-to-charge ratio
\bar{m}	kg	Average single particle mass
m_λ	-	Complex refractive index
M_0	kg/m ³	Mass concentration of uncharged particles
m_d	kg	Effective electron mass
m_e	kg	Mass of an electron in a vacuum
m_g	kg	Mass of gas molecules
m_p	kg	Mass of the particle
m_v	kg	Molecular mass of the evaporated species
N''	molecules/(m ² ·s)	Molecular number flux
n_λ	-	Real component of complex refractive index
n_c	electrons/m ³	Electron number density
n_g	molecules/m ³	Molecular number density
n_{it}	ions/(m ³ ·s)	Ion concentration-time product
n_p	particles/m ³	Number density of particles
$p(x)$	-	Probability density function
\dot{Q}_{abs}	J/s	Rate of laser heat transfer
\dot{Q}_c	J/s	Rate of continuum conduction heat transfer
\dot{Q}_{cond}	J/s	Rate of conduction heat transfer
\dot{Q}_{FM}	J/s	Rate of free-molecular conduction heat transfer
\dot{Q}_{rad}	J/s	Rate of radiation heat transfer

\dot{Q}_{sub}	J/s	Rate of sublimation/vaporization heat transfer
$Q_{\text{abs},\lambda}$	-	Spectral absorption efficiency
$Q_{\text{ext},\lambda}$	-	Spectral extinction efficiency
$Q_{\text{sca},\lambda}$	-	Spectral scattering efficiency
q_0	C	Average charge
T_{Δ}	K	Temperature at Knudsen shell surface
T_g	K	Gas temperature
T_p	K	Particle temperature
$T_{p,\text{eff}}$	K	Effective particle temperature
T_s	K	Temperature at location s
t	s	Time
U_{int}	J	Internal energy
V^{gain}	-	Gain
$V^{\text{gain,ref}}$	-	Reference gain
V^{meas}	V	Measured voltage
v_a	m^2/s	Aerosol flow rate
v_c	-	Exponent describing average charge and particle mass relationship
W	-	Weighting matrix
W_1	J	Laser energy
x_p	-	Size parameter
x_{MLE}	-	Maximum likelihood estimate

Greek characters

Symbol	Unit	Definition
α_c	-	Geometry correction factor
α_T	-	Thermal accommodation coefficient
β_c	-	Scattering cross-correction factor
Γ_x	-	Covariance matrix of Lorentz-Drude fit
γ	s ⁻¹	Dampening factor
γ_0	F/m	Permittivity constant in a vacuum
γ_c	-	Truncation correction factor
Δ	m	Thickness of Knudsen shell
ε_λ	-	Complex dielectric function
ε'_λ	-	Real component of complex dielectric function
ε''_λ	-	Complex component of complex dielectric function
ε_0	-	Higher frequency oscillator constant
ξ	-	Mass mobility exponent
ζ_{rot}	-	Rotational energy modes
θ	K	Difference between particle and gas temperature
$\kappa_{abs,\lambda}$	m ⁻¹	Spectral absorption coefficient
$\kappa_{ext,\lambda}$	m ⁻¹	Spectral extinction coefficient
$\kappa_{sca,\lambda}$	m ⁻¹	Spectral scattering coefficient
λ	m	Wavelength
λ_{MFP}	m	Mean free path of gas molecules

μ	Pa·s	Viscosity
μ_b	-	Mean of bins
ξ_s	-	Riccati-Bessel function of order s
ρ_g	kg/m ³	Gas density
ρ_m	kg/m ³	Material density
ρ_p	kg/m ³	Particle density
ρ_{eff}	kg/m ³	Effective density
$\sigma_{\lambda,e}$	S/m	Spectral electrical conductivity
σ_b	-	Standard deviation of bins
σ_x	-	Standard deviation of Lorentz-Drude fit
σ_{DC}	S/m	DC conductivity
τ	-	Transmissivity
ψ_s	-	Riccati-Bessel function of order s
ω	s ⁻¹	Frequency of incident wave
ω_0	s ⁻¹	Resonant frequency
ω_p	s ⁻¹	Plasma frequency

Abbreviations

Abbreviation	Definition
--------------	------------

AAE	Absorption Ångström exponent
-----	------------------------------

AFM	Atomic force microscopy
-----	-------------------------

BC	Black carbon
----	--------------

BET	Brunauer-Emmett-Teller
brC	Brown carbon
CAPS PM _{SSA}	Cavity attenuated phase shift instrument
CCD	Charge-coupled device
CERMS	CPMA-Electrometer Reference Standard
CMD	Count mean diameter
CPC	Condensation particle counter
CPMA	Centrifugal particle mass analyzer
CVD	Chemical vapor deposition
CW-LII	Continuous wave laser-induced incandescence
DC	Direct Current
DI	Deionized
DMA	Differential mobility analyzer
EELS	Electron energy loss spectroscopy
EMCCD	Electron-multiplying charge-coupled device
FCAE	Faraday cup aerosol electrometer
FLG	Few-layer graphene
FWHM	Full-width half max
GO	Graphene oxide
GSD	Geometric standard deviation
GTO	Graphitic oxide
ICE	Integrated cooling and electronics
INTAC	Interpolated average charge
IS	Integrating sphere

LDLS	Laser-drive light source
LIF	Laser-induced fluorescence
LOSA	Line-of-sight attenuation
MAC	Mass absorption cross-section
MQ	Milli-Q
MSC	Mass scattering cross-section
ND	Neutral density
Nd:YAG	Neodymium-doped yttrium aluminum garnet
PDF	Probability density function
PG	Pristine single-layer graphene
PMT	Photomultiplier tube
PRF	Pulse repetition frequency
rGO	Reduced graphene oxide
SAED	Selected area diffraction
SEM	Scanning electron microscopy
SMPS	Scanning mobility particle sizer
SSA	Specific surface area
SWCNT	Single-walled carbon nanotube
TEM	Transmission electron microscopy
TiRe-LII	Time-resolved laser-induced incandescence
UDAC	Unipolar diffusion aerosol charger
UDE	University of Duisburg-Essen
UV	Ultraviolet
UW	University of Waterloo

Chapter 1

Introduction to reduced graphene oxide, and optical diagnostic techniques

1.1 Motivation

Graphene was discovered by Novoselov et al. [1] in 2004; since then, the properties and utility of graphene and graphene derivatives have been researched heavily. Increasingly, graphene nanoparticles/nanosheets are in high demand in electrical [2,3], biomedical [4], and mechanical [5] applications due to their high electron mobility, large specific surface area, high thermal conductivity, high tensile strength, and flexibility [6]. In electrical applications, graphene has demonstrated superior properties compared to conventional materials in conductive films, semi-conductors, supercapacitors, and batteries [2]. In the context of energy-storage devices, a specific form of graphene known as pristine single layer graphene (PG) (i.e., single atom thick graphene with no defects) is desired due to its high electrical conductivity and mechanical and electrochemical stability [7]. The most common method of producing PG is through chemical vapor deposition (CVD), a process in which carbon-based vapors are deposited on a substrate forming the desired single layered graphene; however, this process is expensive, creates toxic byproducts, and is difficult to scale to industrially relevant levels [8]. An alternative to PG that has similar physical and chemical properties and is more amenable to high yield production is reduced graphene oxide (rGO).

Reduced graphene oxide (rGO) is a graphene-like material that is produced by first synthesizing an intermediate material, graphene oxide (GO), through the oxidation and exfoliation of graphite. The introduction of oxygen to the graphite increases the interlayer spacing between the graphitic layers, creating a material known as graphitic oxide (GTO). The increased interlayer spacing and hydrophilicity due to the oxygen functional groups, allow for easy separation of the graphitic layers (exfoliation) by dispersing the GTO in water to synthesize GO [9]. As a known insulator, GO is unsuitable for energy

storage. After removing the oxygen functional groups, the single layer sheets form a graphene-like material. It should be noted that this process is susceptible to defects and remaining oxygen functional groups, leading to reduced properties. Nonetheless, the rGO synthesized is an attractive alternative to PG due to its amenability to large scale production and tunability.

One of the leading candidates for large scale production of rGO is thermal reduction [10]. There have been many different types of thermal reduction described in the literature such as: heating on a hot plate [11], reduction using hot water [12], and, the most common method of thermal reduction, a furnace [13–15]. An industrially promising variation on the latter is a continuous process that aerosolizes dried GO powder and thermally reduces it using a tube furnace. This process allows for minimal human intervention and high throughput of material. Although this process has high potential, the electrical properties of rGO depend heavily on size, composition, and morphology [16]. Consequently, to make it industrially viable, quality checks must be done on the incoming and produced material to ensure consistent production. Established techniques normally used to characterize nanomaterials include Raman scattering, transmission electron microscopy (TEM), scanning electron microscopy (SEM), and X-ray diffraction (XRD); however, these methods are *ex situ* making them inappropriate for rapid characterization in an industrial setting. As a result, there is a need for *in situ* or online characterization methods that can make temporally and spatially resolved measurements to ensure consistent industrial production of rGO.

A promising subset of candidate techniques is absorption-based optical diagnostics. Absorption-based methods have been heavily utilized to characterize carbon-based materials, such as soot, due to their high absorption characteristics. Two prevalent optical diagnostic methods are time-resolved laser-induced incandescence (TiRe-LII) and line of sight attenuation (LOSA). Time-resolved laser-induced incandescence is a technique that uses a pulsed laser to heat up nanoparticles within a probe volume. The spectral incandescence is recorded over time, usually at several wavelengths, as the nanoparticles return to their initial resting temperature through conductive, radiative, and sublimation-based cooling. The

observed incandescence is a phenomenon resulting from thermal emission of electromagnetic radiation from the hot particle at high temperatures. From the heating and cooling of the particle, common parameters that can be derived are primary particle diameter, volume fraction, and specific surface area [17].

Light of sight attenuation is an extinction-based technique that measures the transmissivity defined as the ratio of light intensity before and after passing through an attenuating medium. Transmissivity is commonly used to derive volume fraction [18], and if spectrally resolved measurements are conducted, LOSA can be used to identify the chemical composition of the medium [19]. The utilization of both techniques in measuring GO and rGO *in situ*/online shows promise; however, there have been no prior studies that have looked into these two materials specifically.

This study reviews the feasibility of utilizing TiRe-LII and LOSA to monitor GO and rGO in real time during their synthesis process. The next section details the current understanding of these techniques and provides an insight into the development and present state of each method.

1.2 Literature review

1.2.1 GO and rGO synthesis

Graphitic oxide (GTO) was first discovered by Broadie in 1859 via the addition of potassium chlorate (KClO_3) to a slurry of graphite while fuming in nitric acid (HNO_3) [20]. This process was then improved upon by Saudenmaier in 1898 by using concentrated sulfuric acid (H_2SO_4) as well as nitric acid and adding the chlorate in batches, making the production of GTO practical with a simple protocol [21]. Presently, the most commonly used method of synthesizing GTO was developed by Hummers and Offerman in 1958 [22], which is now known as Hummer's method. This method consists of oxidizing the graphite with KMnO_4 and NaNO_3 in concentrated H_2SO_4 . Although Hummer's method is very popular, toxic gases such as NO_2 , N_2O_4 , and ClO_4 are generated, motivating research into new, safer methods. Marcano et al. [23] developed the improved Hummer's method, which consists of oxidizing the graphite

in a 9:1 H₂SO₄/H₃PO₄ solution without NaNO₃. The lack of NaNO₃ prevents the creation of toxic NO_x gases and improves the efficiency of the oxidation. Marcano et al. [23] found that their method produces a higher fraction of well-oxidized hydrophilic GTO and possesses a more regular structure compared to Hummer's method. Although the improved Hummer's method reduced toxic gas emission and improved efficiency, a drawback with the process was that it required a high ratio of auxiliary agents (oxidizing agents and acids) to graphite and is very time-intensive, making the large-scale production of GTO difficult. Yu et al. [24] developed a method of reducing the ratio of auxiliary agents and reaction time by partly replacing the KMnO₄ with K₂FeO₄ and reducing the amount of H₂SO₄. The reaction time could be reduced to five hours with a material ratio of 1:1.5:10 (graphite: oxidant: solvents/acid) compared to the 12+ hour method developed by Marcano et al. [23] with a material ratio of 1:6:133.

The exfoliation of GTO into graphene oxide (GO) was first carried out by Boehm et al. [25]; however, GO was not properly explored until after the discovery of graphene by Novoselov and Geim [1]. Titelman et al. [26] investigated the GO synthesis process and GO properties in colloidal form. They found that GO films may be easily prepared by aqueous dispersion and a continuous film-like structure can be achieved by fully eliminating the water remaining in the GO particles. The increased interlayer spacing, coupled with the hydrophilic nature of GTO, makes for easy exfoliation in aqueous media, leading to stable colloidal suspensions. It was noted by Stankovich et al. [27] that, although GO had a single layer similar to graphene, GO is electrically insulating due to the oxygen functional groups disrupting the graphitic network. As the electrical conductivity can be recovered by removing the oxygen functional groups and restoring the graphitic network, the reduction of GO is one of its most important applications.

The first reported reduction method was the chemical reduction of colloidally dispersed GO using hydrazine monohydrate. Stankovich et al. [28] found that over 24 hours the colloidal GO solution transitions from brown to black and precipitates out as randomly aggregated, thin, crumpled sheets of reduced graphene oxide (rGO). They showed that the conductivity of the rGO is five orders of magnitude

better than GO and comparable to the conductivity of pristine graphene (PG). Other chemicals have also been tested such as sodium borohydride (NaBH_4), organic solvents (dimethylformamide, methanol, ethanol), gaseous hydrogen, ascorbic acid and strong alkaline solutions [29–33]. More common methods of chemical reduction (hydrazine and sodium borohydride) produce highly electrically conductive rGO, similar in magnitude to PG; a drawback, however, is that they use hazardous reactants. Additionally, there is a lack of understanding of the mechanisms of reduction making it difficult to tailor rGO characteristics.

Electrochemical reduction was developed as an attempt to improve chemical reduction by bypassing the need for hazardous reactants (e.g., hydrazine) and directly depositing the rGO on the sample. It was found that the rGO coatings can reach a conductivity of 8500 S/m; however, electrochemical reduction only works on the surface of electrodes and cannot mass produce rGO powder [32,34]. Moreover, similar to chemical reduction, the mechanisms of reduction are not well understood, making it difficult to predict how changes in reduction parameters, such as reduction agents and reduction potential, will affect rGO characteristics.

Thermal reduction is another common method that shows promise in producing large batches of rGO powder. Schniepp et al. [35] showed that both thermal exfoliation and reduction of GO into single rGO sheets can be achieved due to the expansion of CO_2 in between the graphitic layers during rapid heating. They achieved the thermal exfoliation by placing GO powder into a quartz tube and rapidly heating it to 1050 °C. Further studies by Luo et al. [14] and Ma et al. [15] showed that aerosolized GO can be transported into a heated tube furnace to produce crumpled rGO. Crumpled rGO particles are more stable than sheets due to chemical bonding at folded ridges. The crumpled particles have a consistently higher surface area, making them beneficial for applications that rely on the high surface area of graphene, like energy storage.

The thermal reduction process has been examined extensively. Huh [36] determined that at different temperature ranges certain oxygen functional groups evaporate, increasing interlayer spacing, and at higher temperatures (~1000 °C) the removal of the groups can cause cracking, which introduces

structural defects. Sengupta et al. [37] showed that the most important parameter in the kinetics of thermal reduction is temperature, so the characteristics of rGO can be easily tuned by adjusting the temperature.

Thermal reduction shows high potential for high throughput synthesis due to the speed of reduction and tunability of final rGO parameters; however, to manufacture rGO at an industrial scale, the functionality of the rGO produced must be thoroughly characterized, including its morphology, electrical conductivity, and specific surface area. Two optical techniques that show promise are time-resolved laser induced incandescence (TiRe-LII) and line of sight attenuation (LOSA).

1.2.2 TiRe-LII analysis

The basis of TiRe-LII relies on analyzing the laser-induced incandescence of aerosolized particles to derive information on particle size, volume fraction, and optical characteristics. This phenomenon was first documented by Weeks and Duley [38] in 1974 where they established that laser-induced incandescence using 10.6 μm laser pulses can provide information on the size of aerosolized atmospheric particles. This phenomenon was then expanded upon by Eckbreth [39] and Melton [40], who revealed that this procedure can be used to analyze the size distribution and volume fraction of soot particles. Eckbreth [39] showed that the incandescence from soot particles can overpower signals from Raman measurements and showed the time dependence of the incandescence to laser heating, particle vaporization, and conduction heat transfer to the surrounding medium. Melton [40] took the general framework presented by Eckbreth [39] and expanded it to include radiation, deriving a general equation to describe the energy balance of the incandesced particle. Since these pioneering works, LII has grown to be the standard process used to determine size distributions and volume fraction of soot particles from combustion processes [41–45]. A schematic of standard LII operation is shown in Figure 1-1.

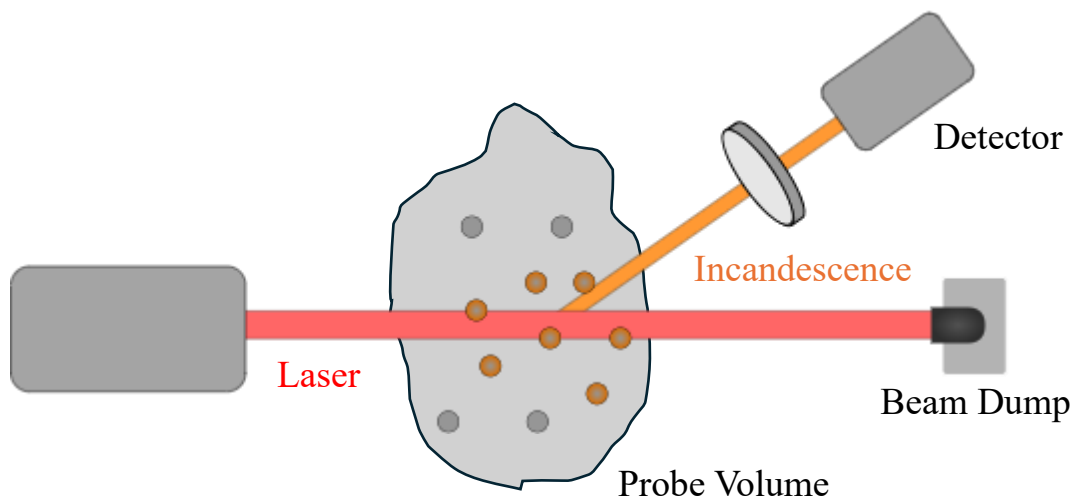


Figure 1-1: Schematic of standard TiRe-LII operation

There are two main variants of LII: pulsed-laser heating, which is primarily used for combustion diagnostics, and continuous-wave (CW-LII) laser heating which is mainly applied in atmospheric measurements [17]. Both methods rely on energy and mass balances derived from the absorption of laser energy, conduction, radiation, and vaporization. This work focuses on the pulsed-laser variation of LII due to the desire to examine the particle size distribution, as compared to the emphasis of CW-LII on particle composition as outlined in Stephens et al. [46]. In pulse-laser LII, many models have been developed to derive different characteristics of the targeted particles. Kock et al. [47], Will et al. [48], and Woiki et al. [49], contributed heavily to the development of a model that focused on using time-resolved signals to derive primary-particle sizing; this approach is commonly referred to as TiRe-LII.

During this period, as many models were being developed, works by Schulz et al. [41] and Michelsen et al. [45], aimed to consolidate and compare multiple LII models used on soot nanoparticles. Through these studies, they determined that while the underlying models were similar, slight differences in the treatment of sublimation and uncertainties in the physical and thermophysical properties of soot led to a broad range of inferred nano aerosol properties, even under well-defined input conditions (i.e smooth laser temporal profile). The comparison by Schulz et al. [41] determined that differences in the thermal

accommodation coefficient (α_T), complex refractive index (m_λ), treatment of aggregation size and structure, and sublimation models contributed the most to variations. The study by Michelsen et al. [45] further confirmed this by simulating LII models with a defined thermal accommodation coefficient (α_T) and complex refractive index (m). It was found that the models were much more consistent when defining these parameters at low fluences (laser powers) where the lower temperatures did not allow for the particle to sublimate. On the other hand, at higher fluences where sublimation occurred the models still differed heavily, showing the effect of sublimation model selection.

Additionally, TiRe-LII has been used to characterize a variety of non-soot materials [50]. Vander Wal et al. [51] used LII to characterize and measure nanoparticle concentration of iron (Fe), titanium (Ti), molybdenum (Mo), and tungsten (W). The work showed linearity between particle mass concentration and incandescence and showed the applicability of double pulse experiments to measure change in particle mass due to vaporization. At a similar time, Filipov et al. [52] showed that the size distribution of silver (Ag) and titanium nitride (TiN) can be resolved from TiRe-LII by numerically solving a Fredholm integral equation of the first kind. Metal nanoparticles continue to be a topic of high interest with studies into aggregate structures, sintering, signal corruptions, and more [53–55]. Vander Wal et al. [56] further looked into using LII to analyze carbon nanotubes doped with Fe nanoparticles and nanofibers doped with Ni particles. It was determined from two-pulsed laser studies that the material provides strong signals at low fluences, and vaporization occurs at higher laser fluences similar to soot. Cau et al. [57] looked at utilizing TiRe-LII in conjunction with laser-induced fluorescence (LIF) *in situ* to measure the evolution of carbon-based gas when forming carbon nanotubes. Through this method they were able to determine the temperatures and steps involved in single-walled carbon nanotube (SWCNT) production. Musikhin et al. [58] looked into using TiRe-LII to characterize aerosolized few layer graphene (FLG) in hopes of validating the method for *in situ* diagnostics. They aerosolized the FLG and determined that it reaches a higher temperature than soot, therefore having higher absorption characteristics, and is linearly dependent on FLG particle concentration, suggesting that TiRe-LII may be suitable for *in situ* characterization of

FLG. In a subsequent study, *in situ* characterization was carried out by López-Cámara et al. [59] by analyzing the FLG synthesized directly after a plasma reactor. In this study, the incandescent data was analyzed to derive the SSA for the soot and FLG synthesized and was validated from subsequent Brunauer-Emmett-Teller (BET) analysis.

TiRe-LII is the standard process for characterizing the particle size and volume fraction for carbon-based materials, making it a promising method for GO and rGO; however, other characteristics, such as composition and functionalization, are desired to derive a comprehensive understanding of the material produced. To provide these characteristics, the feasibility of using line of sight attenuation (LOSA) will be studied.

1.2.3 LOSA Measurements

Extinction measurements have been prevalent as an optical diagnostic tool in the combustion community. Extinction refers to the attenuation of light due to absorption and scattering from a participating medium. The Bouguer-Beer-Lambert Law describes this phenomenon [60]:

$$I_{\lambda}(S) = I_{\lambda}(0) \exp \left[- \int_0^S \beta_{\lambda}(S^*) dS^* \right] \quad (2.1)$$

where I_{λ} is the intensity of the light, S is the target location and, β_{λ} is the extinction coefficient. This relationship was first proposed by Bouguer in 1729 and then cited by Lambert in 1760 [60]. Beer further expanded on it in 1852 where his work detailed how light is attenuated as it passes through a medium [61]. Extinction measurements of soot were first documented in 1932 by Hottel and Broughton [62], where they measured the attenuation of light by soot particles in flames to determine flame temperatures and radiation properties.

A common form of extinction measurements used for online analysis is known as line-of-sight attenuation (LOSA). This method consists of directing a light beam through a medium and measuring the attenuation to determine the properties of the medium. A schematic of an LOSA system is shown in

Figure 1-2. Greenberg and Ku [63] introduced a variation to this method known as two-dimensional LOSA (2D-LOSA). This method spatially resolves the measurement by mapping the light onto a charge-coupled device (CCD) detector with each pixel being spatially independent and inverts the data to provide two-dimensional soot volume fraction maps. Thomson et al. [64] developed a variation to the 2D-LOSA method using a diffuse light source, allowing more sensitive measurements. Thomson [65] then developed a new method of analysis called Spec-LOSA that is able to spectrally resolve the data with the help of an imaging spectrometer. Using spatially and spectrally resolved LOSA, there have been many studies to investigate the composition of the participating media. Examples of this are the studies by Liu et al. [66] and Asif et al. [67], which utilized spatially and spectrally resolved LOSA *in situ* to measure the extinction coefficient during the gas-phase synthesis of germanium (Ge) and silicon (Si) nanoparticles, respectively. Liu et al. [66] verified the feasibility of LOSA in measuring germanium and Asif et al. [67] obtained qualitative information of the fraction of liquid and solid phase Si nanoparticles, thereby elucidating the particle synthesis process.

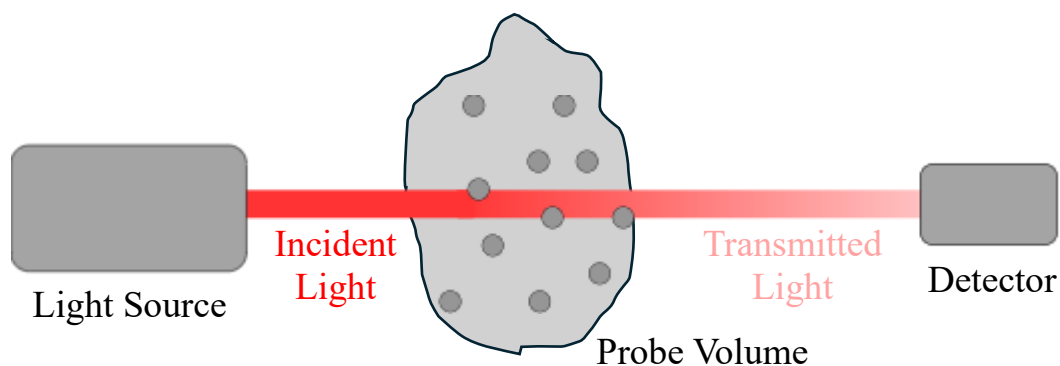


Figure 1-2: Schematic of standard LOSA operation

1.3 Present Work

Reduced graphene oxide remains an attractive material in energy storage applications due to its amenability to high-yield production and similar properties to graphene. Thermal reduction of rGO shows

the most promise for large-scale synthesis due to its speed of reduction and high throughput. To realize this process at an industrial scale, the process parameters must be well understood and the produced rGO must be well characterized to ensure the functionality of the synthesized material in its end application. TiRe-LII and LOSA are used heavily in soot characterization; consequently, they show promise for *in situ* characterization of the particle size, reduction level and functional parameters of GO and rGO. The overall goal of the present work is to identify the feasibility of absorption-based diagnostics for *in situ* characterization of GO and rGO. This will be done by analyzing and connecting the optical and morphological characteristics of GO and rGO, followed by experimental TiRe-LII and LOSA testing of the material to determine feasibility.

The subsequent sections of the thesis are arranged as follows: Chapter 2 describes the theoretical framework for the heat transfer sub-model in TiRe-LII, the spectrally resolved extinction model used in LOSA, and the Lorentz-Drude model that is used to further analyze the data from UV-Vis spectroscopy and LOSA.

Chapter 3 describes the thermal reduction system, the four-colour TiRe-LII system at the University of Waterloo (UW), and the plasma reactor and LOSA present at the University of Duisburg-Essen (UDE).

Chapter 4 details the experimental set-up and methods used at the NRC for characterizing and connecting the optical properties of GO to morphology, including TiRe-LII measurements made on GO with a commercial device (LII-300).

Chapter 5 presents morphological and optical properties of GO derived from the visit at the NRC. Mobility diameter distribution, effective density, mass-mobility exponent, wavelength-resolved absorption coefficient, mass absorption cross-section (MAC), and mass scattering cross-section (MSC) are presented. Results from this study are contrasted against studies done by Ma et al. [15,68] and MAC and MSC are compared against a fitted Mie model to derive trends.

Chapter 6 presents *in situ* TiRe-LII measurements on aerosolized rGO. A detailed explanation of the analysis of the data is presented and compared against literature results. Additionally, *ex situ* measurements conducted using a Brunauer-Emmett-Teller specific surface area (BET-SSA) tester were examined to validate the TiRe-LII results.

Chapter 7 presents UV-Vis spectroscopic analysis of colloidal GO and rGO alongside LOSA measurements of aerosolized rGO using a plasma reactor in UDE. A model developed using the Lorentz-Drude approach to derive the electrical conductivity from the spectrally resolved extinction data is also presented and compared to results present in the literature.

Chapter 8 provides a summary of the research and future work that can be done. This will include a rough plan on what characterization methods may be suitable for *in situ* diagnostics and what future work needs to be done to realize these methods.

Chapter 2

TiRe-LII and LOSA Theory and Modelling

As evident from the previous chapter, time-resolved laser-induced incandescence (TiRe-LII) and line of sight attenuation (LOSA) have been used heavily in particle optical diagnostics. Consequently, both characterization methods involve different analytical techniques depending on the particle and particle environment examined. This chapter focuses on the analytical methods employed in this study, detailing the theory and application of both the TiRe-LII and LOSA models.

2.1 Time-resolved laser-induced incandescence analysis

The theoretical framework that defines TiRe-LII is based on the energy and mass conservation of nanoparticles being heated up and cooling down after laser interaction [41]. The energy-balance equation of the particle can be represented by [17]:

$$\frac{dU_{\text{int}}}{dt} = \dot{Q}_{\text{abs}} - \dot{Q}_{\text{rad}} - \dot{Q}_{\text{cond}} - \dot{Q}_{\text{sub}} \quad (3.1)$$

The left side of Eq. (3.1) represents the rate of change of internal energy in the particle and is commonly expressed as:

$$\frac{dU_{\text{int}}}{dt} = m_p c_p \frac{dT_p}{dt} \quad (3.2)$$

where U_{int} is the internal energy of the particle, m_p is the mass of the particle, c_p is the specific heat of the particle, T_p is the particle temperature and t is time. The right side of Eq. (3.1) represents the different heat transfer terms that influence the change in temperature over time. Additional mechanisms that are considered in the literature are oxidative heating, thermionic cooling, and heating due to annealing [45]; however, these terms will be omitted in this study.

Equation (2.3) is visually depicted in Figure 2-1. The heating rate of the particle due to particle absorption of incident laser is represented by \dot{Q}_{abs} ; similarly, \dot{Q}_{rad} represents the particle's cooling rate due

to radiation, \dot{Q}_{cond} represents the cooling rate due to conduction, and \dot{Q}_{sub} represents the cooling rate of the particle associated with vaporization/sublimation. Vaporization not only cools the nanoparticle but also leads to mass loss. This mass loss can be accounted for by [69]:

$$\frac{dm_p}{dt} = -m_v \frac{\dot{Q}_{\text{vap}}(t)}{\Delta H_v} \quad (3.3)$$

where m_v is the molecular mass of the evaporated species, and ΔH_v is the molar latent heat of vaporization.

One of the goals of the present analysis is to derive the specific surface area (SSA), which is the ratio of surface area (A_{cond}) to mass for a particle (m_p) [59]:

$$SSA = \frac{A_{\text{cond}}}{m_p} \quad (3.4)$$

The simplest approach to achieve this is to identify regions of the particle cooling that are predominately governed by conduction. Under these conditions Eq. (3.1) can be further simplified to:

$$\rho_p c_p \frac{\pi d_p^3}{6} \frac{dT_p}{dt} = \dot{Q}_{\text{cond}} \quad (3.5)$$

where ρ_p is the particle density and d_p is the particle diameter. This will be the basis of our analysis moving forward and focus of the subsequent model examination.

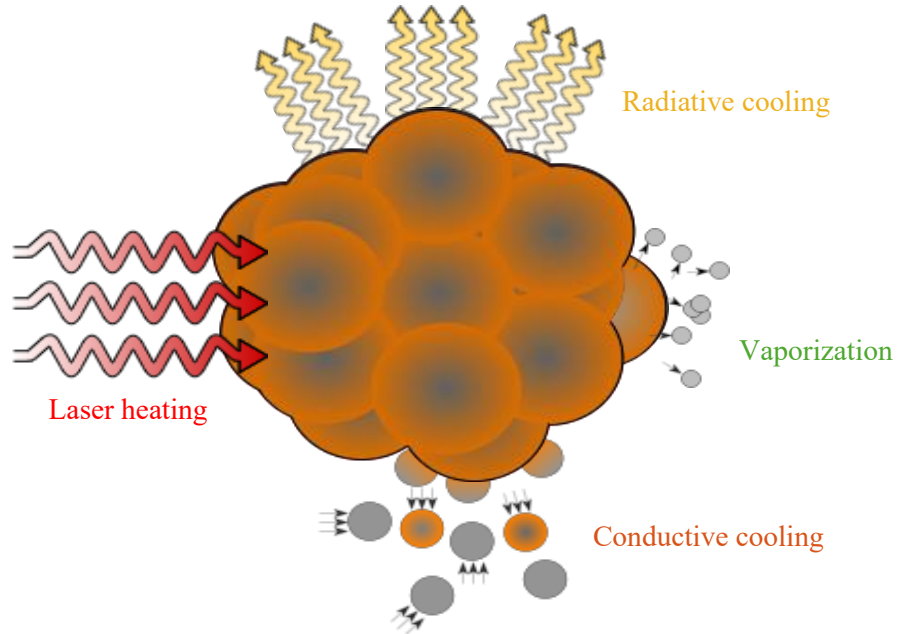


Figure 2-1: Visual representation of heating and cooling process of nanoparticle

2.1.1 Optical Pyrometry

Figure 1-1 illustrates that TiRe-LII operates by detecting the incandescence of the particles after they are heated by a laser. Typically, this is done using a photomultiplier tube (PMT), which amplifies incident photons into an electrical signal through photoemission [70]. As shown in Eq. (3.1), TiRe-LII measures the time-resolved incandescence of aerosolized particles heated with a laser pulse and models the heating and cooling dynamics of the particle to derive their characteristics. To do this, the electrical signal derived from the PMTs must be converted to temperature readings. This is done through optical pyrometry [58,59,71,72].

Optical pyrometry determines the temperature of a particle by measuring the intensity of its emitted radiation at specific wavelengths, as described by Planck's law. This is done by fitting a modelled intensity signal (J_{mod}) to an experimentally determined intensity signal (J_{exp}) allowing for the derivation of the effective temperature ($T_{\text{p,eff}}$) of particles within the probe volume. A challenge with this technique during TiRe-LII is that particles within the probe volume are generally at different temperatures at any

instant due to variations in their sizes. Nevertheless, a common approach is to approximate the size distribution, which is dependent on the synthesis process of the particles, as narrow, thereby allowing for the assumption that the particle temperature is uniform.

To determine the pyrometric temperature, incandescent signals at two or more wavelengths are required. The incandescent signals (J_{exp}) can be fitted against a modelled intensity signal (J_{mod}) as defined as [73–75]:

$$J_{\text{mod},\lambda}(t) = C_\lambda n_p \int_0^\infty p(d_p) \frac{\pi d_p^2}{4} Q_{\text{abs},\lambda}(d_p, m_\lambda) I_{\text{b},\lambda} [T_{\text{p,eff}}(t, d_p)] d(d_p) \quad (3.6)$$

where C_λ is a calibration constant, n_p is the number density of the particles, $p(d_p)$ is the probability density function (pdf) of the particle size distribution, $Q_{\text{abs},\lambda}$ is the spectral absorption efficiency of the particle, m_λ is the complex refractive index and $I_{\text{b},\lambda}$ is the blackbody spectral intensity as defined by [60]:

$$I_{\text{b},\lambda} = \frac{2\pi h c_0^2}{\lambda^5 \left[\exp\left(\frac{hc_0}{m_\lambda k_B \lambda T_{\text{p,eff}}}\right) - 1 \right]} \quad (3.7)$$

where h is the Planck's constant, k_B is the Boltzmann's constant, and c_0 is the speed of light. It is important to note that there are two common forms of $Q_{\text{abs},\lambda}$ depending on the size and m_λ of the particle. The general solution for $Q_{\text{abs},\lambda}$ is derived from the Mie theory, developed independently by Ludwig Lorenz and Gustav Mie, which describes the interaction of an electromagnetic wave with a spherical particle [76]. The theory can be described as [76]:

$$Q_{\text{ext},\lambda}^{\text{Mie}} = \frac{2}{x_p^2} \sum_{s=1}^{\infty} (2s+1) \text{Re}(a_s + b_s) \quad (3.8)$$

$$Q_{\text{sca},\lambda}^{\text{Mie}} = \frac{2}{x_p^2} \sum_{s=1}^{\infty} (2s+1) (|a_s|^2 + |b_s|^2) \quad (3.9)$$

where $Q_{\text{ext},\lambda}^{\text{Mie}}$ and $Q_{\text{sca},\lambda}^{\text{Mie}}$ are the spectral extinction and scattering efficiencies, respectively, and a_s and b_s are the scattering coefficients as defined as [76]:

$$a_s = \frac{m_\lambda \psi_s(m_\lambda x_p) \psi'_s(x_p) - \psi_s(x_p) \psi'_s(m_\lambda x_p)}{m_\lambda \psi_s(m_\lambda x_p) \xi'_s(x_p) - \psi_s(x_p) \xi'_s(m_\lambda x_p)} \quad (3.10)$$

$$b_s = \frac{\psi_s(m_\lambda x_p) \psi'_s(x_p) - m_\lambda \psi_s(x_p) \psi'_s(m_\lambda x_p)}{\psi_s(m_\lambda x_p) \xi'_s(x_p) - m_\lambda \psi_s(x_p) \xi'_s(m_\lambda x_p)} \quad (3.11)$$

where $x_p = \pi d_p / \lambda$ is the size parameter, and ψ_s and ξ_s are the Riccati-Bessel functions of order s .

When $x_p \ll 1$ (size parameter criterion) and $|m_\lambda x_p| \ll 1$ (phase-shift criterion), Mie theory converges to the Rayleigh limit [76,77]. The Rayleigh approximation assumes that the dipoles within the particles “see” a uniform fluctuation in the electric field, so absorption depends only on the number and susceptibility of dipoles within the particle volume. This assumption is commonly applicable in TiRe-LII studies of carbon-based nanomaterials due to the small size of particles analyzed [41,45,58,59,72]. The Rayleigh approximation is given by [76]:

$$Q_{\text{abs},\lambda}^{\text{Ray}} = 4x_p E(m_\lambda) \quad (3.12)$$

$$Q_{\text{sca},\lambda}^{\text{Ray}} = \frac{8}{3} (x_p)^4 F(m_\lambda) \quad (3.13)$$

where $E(m_\lambda)$ and $F(m_\lambda)$ are the spectral absorption function and spectral scattering function, respectively, given by:

$$E(m_\lambda) = \text{Im} \left(\frac{m_\lambda^2 - 1}{m_\lambda^2 + 2} \right) \quad (3.14)$$

$$F(m_\lambda) = \left| \frac{m_\lambda^2 - 1}{m_\lambda^2 + 2} \right|^2 \quad (3.15)$$

Due to a lack of knowledge of the particle size distribution, a common approximation is to approximate the particle as being monodisperse, so that Eq. (3.6) simplifies into [73]:

$$J_{\text{mod},\lambda}(t) = C_\lambda n_p \frac{\pi d_p^2}{4} Q_{\text{abs},\lambda}(d_p, m_\lambda) I_{\text{b},\lambda} [T_{\text{p,eff}}(t, d_p)] \quad (3.16)$$

Additionally, during the pyrometric analysis, n_p , $Q_{\text{abs},\lambda}$ and d_p can be integrated into C_λ due to the fact that $T_{\text{p,eff}}$ is the only parameter of interest. This further simplifies $J_{\text{mod},\lambda}$ to:

$$J_{\text{mod},\lambda}(t) = C_\lambda I_{\text{b},\lambda} [T_{\text{p}}(t, d_p)] \quad (3.17)$$

Utilizing $J_{\text{exp},\lambda}$ and $J_{\text{mod},\lambda}$ the effective temperature can be derived using a non-linear minimization:

$$\begin{bmatrix} T_{\text{p,eff}} \\ C_\lambda \end{bmatrix} = \arg \min_{T_{\text{p,eff}}, C_\lambda} \left\{ \left\| \begin{array}{c} J_{\text{exp},\lambda_1} - J_{\text{mod},\lambda_1} \\ \vdots \\ J_{\text{exp},\lambda_n} - J_{\text{mod},\lambda_n} \end{array} \right\|_2^2 \right\} \quad (3.18)$$

where λ_n is the n^{th} wavelength. Solving this provides $T_{\text{p,eff}}$ over the total time of the experimental signal giving a history of the particle's effective temperature over time. For a pair of wavelengths in the Rayleigh limit, by using Wien's approximation [60], where $\exp(hc_0/m_\lambda k_B \lambda T_{\text{p,eff}}) \gg 1$, Eq. (3.7) becomes

$$I_{\text{b},\lambda} = \frac{2\pi hc_0^2}{\lambda^5 \left[\exp\left(\frac{hc_0}{m_\lambda k_B \lambda T_{\text{p,eff}}}\right) \right]} \quad (3.19)$$

Using Eq. (3.19), the minimization can be simplified into a closed form solution [69]:

$$T_{\text{p,eff}} = \frac{hc_0}{k_B} \left(\frac{1}{\lambda_2} - \frac{1}{\lambda_1} \right) \left[\ln \left(\frac{J_{\lambda,1} E(m_{\lambda,2}) \left(\frac{\lambda_1}{\lambda_2} \right)^6}{J_{\lambda,2} E(m_{\lambda,1}) \left(\frac{\lambda_2}{\lambda_1} \right)^6} \right) \right]^{-1} \quad (3.20)$$

2.1.2 Conduction Heat Transfer

In TiRe-LII, conductive heat transfer dominates particle cooling, especially under low laser power conditions (low fluences (F_0)). Fluences are defined by taking a ratio between the laser energy (W_l) and cross-sectional area of the laser beam at the probe volume (A_{laser}):

$$F_0 = \frac{W_l}{A_{\text{laser}}} \quad (3.21)$$

and are commonly used to identify the laser power applied.

The mechanism for conductive-heat-transfer varies based on the mean free path of the motive gas (λ_{MFP}) and the characteristic length (L) of the particles. The mean free path of the motive gas is ambiguous as it can be defined in multiple ways [78]. In this study, the Maxwell mean free path equation, based on dynamic viscosity, is employed [79]:

$$\lambda_{\text{MFP}} = \frac{\mu(T_g)}{\rho_g(T_g, P_g) \sqrt{2k_B T_g / (\pi m_g)}} \quad (3.22)$$

Where T_g is the temperature of the gas, $\mu(T_g)$ is the gas viscosity, $\rho_g(T_g, P_g)$ is the gas density, and m_g is the average mass of the gas molecules. The characteristic length of the particle is commonly taken to be the radius of the particle. The ratio between the mean free path and characteristic length is the Knudsen number (Kn). The Kn number defines the conduction regime by indicating whether conduction heat transfer occurs in the continuum, free-molecular, or transition regime. The Kn ranges that define the three regimes are shown in Figure 2-2.

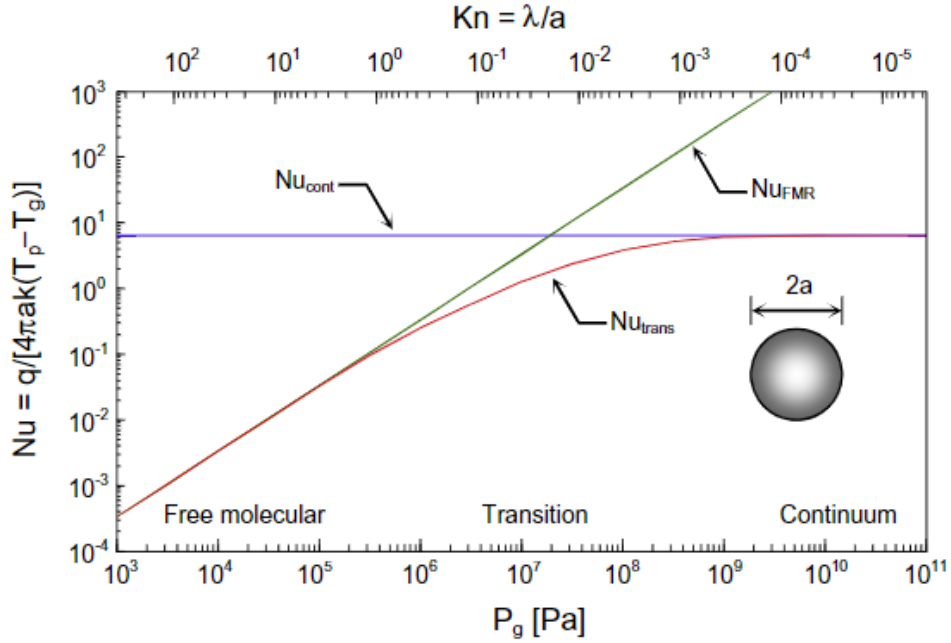


Figure 2-2: Heat conduction as defined by three regimes: free molecular, transition, and continuum [78]

At high Kn numbers ($\gg 10$) the primary mechanism of heat conduction is dominated by collisions between the gas molecules and particle with negligible inter-gas collisions. In this regime, the gas molecules can be described as travelling ballistically between the particle surface and equilibrium gas without undergoing intermolecular collisions. This is known as the free molecular regime and is the dominant regime in LII applications. The heat and mass transfer processes in this regime can be described by [78]:

$$\dot{Q}_{FM} = \pi d_p^2 N'' \langle E_0 - E_i \rangle \quad (3.23)$$

where N'' is the incident molecular number flux and $\langle E_0 - E_i \rangle$ is the average energy change of a gas molecule scattering from the particle surface. A subsequent study by Daun [80] used molecular dynamic simulations to model free molecular conduction between soot particles and the gas. From this study, it was determined that the gas molecules preferentially accommodate normal-translational modes of the gas molecule, followed by the rotational energy modes. Applying this and further simplifications, Eq. (3.23) can be modified to become [59,80]:

$$\dot{Q}_{\text{FM}} = \alpha_{\text{T}} A_{\text{cond}} N'' k_{\text{B}} \left(2 + \frac{\zeta_{\text{rot}}}{2} \right) \left(\frac{T_{\text{p}}}{T_{\text{g}}} - 1 \right) \quad (3.24)$$

where α_{T} is the thermal accommodation coefficient, A_{cond} is the surface area of the particle available for conduction cooling, ζ_{rot} are the particle rotational energy modes, and N'' is the molecular number flux of the ambient gas molecules as given by:

$$N'' = \frac{1}{4} n_{\text{g}} c_{\text{g}} = \frac{1}{4} \frac{P_{\text{g}}}{k_{\text{B}} T_{\text{g}}} \sqrt{\frac{8k_{\text{B}} T_{\text{g}}}{\pi m_{\text{g}}}} \quad (3.25)$$

where n_{g} is the molecular number density and c_{g} is the mean thermal speed of the gas molecules as defined as:

$$c_{\text{g}} = \sqrt{\frac{8k_{\text{B}} T_{\text{g}}}{\pi m_{\text{g}}}} \quad (3.26)$$

At lower Kn numbers ($\ll 0.01$) the gas molecules can no longer be described as ballistic between the surface of the particle to the equilibrium gas. Instead, they collide multiple times with other gas molecules before colliding with the particle. The transport of energy is impeded by collisions between separate gas molecules. Consequently, in this regime, known as the continuum regime, the microscopic behaviour of the gas molecules can be ignored, and Fourier's law can be used to describe the heat conduction:

$$\dot{Q}_{\text{C}} = 2\pi d_{\text{p}} \bar{k} (T_{\text{p}} - T_{\text{g}}) \quad (3.27)$$

where

$$\bar{k} = \frac{1}{T_{\text{p}} - T_{\text{g}}} \int_{T_{\text{g}}}^{T_{\text{p}}} k(T) dT \quad (3.28)$$

is the average thermal conductivity of the gas between T_p and T_g , and k is the thermal conductivity of the gas. In LII measurements, particles are rarely in this regime due to their small sizes, and they only enter this regime at extremely high pressures [79].

When Kn is greater than 0.01 and less than 10, heat conduction occurs within the transition regime, where a collisionless Knudsen layer of thickness Δ forms around the surface of the particle causing a shift in the macroscopic properties of the gas. A temperature jump arises as gas molecules are unlikely to collide with one another within the Knudsen layer, having no effect on the equilibrium gas temperature. Unlike the free molecular and continuum regime, the transition regime cannot be solved analytically as it is governed by the nonlinear Boltzmann equation [79]. To address this, various solution methods, including approximate analytical approaches and diffusion approximations, have been developed and used in LII analysis. A widely used and accurate method is the boundary sphere method, also known as Fuchs' method [81]. In this approach, the gas surrounding a particle is divided into two regions: a shell surrounding the particle where gases behave like free molecular gases and a region outside that shell where gases behave like continuum gases. This concept is schematically shown in Figure 2-3. At the edge of the shell, defined by a thickness of Δ , applying conservation of energy leads to:

$$4\pi a \bar{k} (T_\Delta - T_g) = \alpha_T A_{\text{cond}} N_g'' k_B \left(2 + \frac{\zeta_{\text{rot}}}{2} \right) \left(\frac{T_p}{T_\Delta} - 1 \right) \quad (3.29)$$

where T_Δ is the temperature at the shell and \bar{k} is evaluated in between T_Δ and T_g . The main concern when using this method is determining what Δ should be used. A common choice is to set $\Delta = \lambda_{\text{MFP}}$ as justified by Kennard [82] and Goodman [83] and further validated by Daun [78]. The temperature at the shell can be derived implicitly, and the rate of conduction can be computed by solving either the free-molecular or continuum regime using the derived T_Δ .

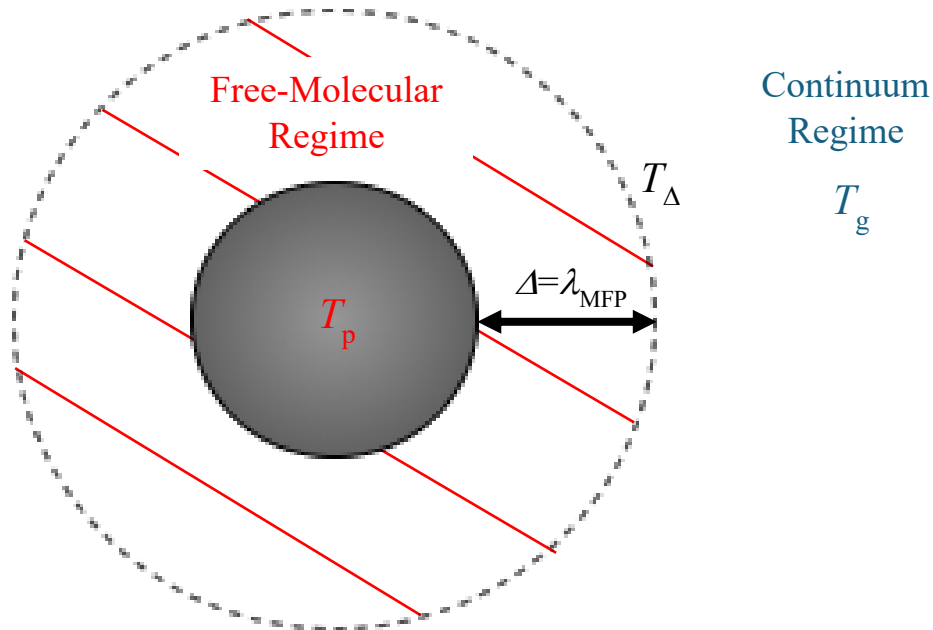


Figure 2-3: Schematic of Boundary Sphere Method (Fuchs's Method)

2.1.3 Specific Surface Area Analysis

A valuable property that can be derived from TiRe-LII is the primary particle size. For spherical particles or agglomerates with point contact (soot), the primary particle diameter d_p can be found by solving Eq. (3.1) using the experimental temperature; however, for non-spherical particles, defining a “physical” primary particle diameter is challenging due to the complex relationship between volume and diameter. In such cases, a characteristic length is often chosen based on the particle’s volume-to-surface ratio [84]. The specific surface area (SSA), as defined in Eq. (3.4), is the ratio of the particle’s cross-sectional area to its mass. The SSA provides information on the particle’s packing density and surface characteristics, such that a higher SSA indicates a greater surface area available for interactions influencing the material’s functional properties, including specific capacitance, electrical conductivity, orientation, and structural quality [85,86]. Understanding SSA is helpful to characterize and tailor a material’s functional properties.

To derive the SSA from TiRe-LII, the simplest method is to operate under conditions where the cooling rate is dominated by conduction heat transfer. This allows the use of Eq. (3.5), greatly simplifying

the solution. For higher fluences ($> 0.2 \text{ J/cm}^2$), vaporization/sublimation heat transfer occurs alongside conduction heat transfer directly after the laser pulse [41]. Vaporization leads to loss in mass, reducing the overall specific surface area of the particle, making the SSA analysis inaccurate for the produced material. However, at low fluences ($< 0.2 \text{ J/cm}^2$), the cooling signal is dominated by exponential decay, characteristic of conduction cooling, after a short period of non-exponential anomalous cooling ($\sim 10\text{-}25 \text{ ns}$) after the laser pulse [71]. At long cooling times, nonuniform cooling of different-sized particles lead to another non-exponential cooling period. As a result, conduction heat transfer should be analyzed over this time period.

To conduct the analysis, the temperature plot is converted to a semilog plot by taking $\theta(t) = T_p(t) - T_g$. On a semilog scale, the $\theta(t)$ will be linear, allowing a simple linear regression to be applied. This is visualized in Figure 2-4, where Daun et al. [71] shows a linear regression applied to the “exponential range” of $\ln[\theta(t)]$.

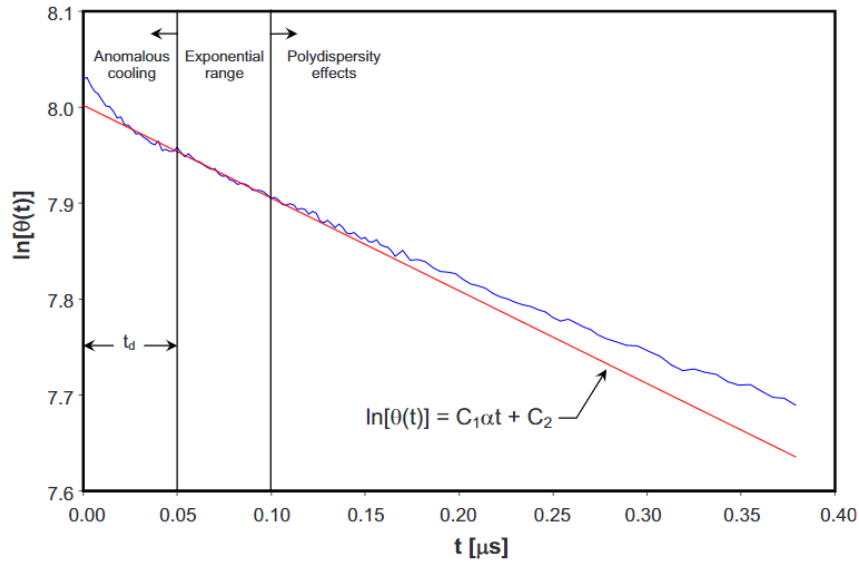


Figure 2-4: Linear regression of TiRe-LII conduction cooling [71]

In the free molecular regime, the SSA can be determined analytically by rearranging Eq. (3.5). Using the definition of U_{int} as described by Eq. (3.2) and \dot{q}_{FM} as described by Eq. (3.24) the SSA can be solved for using [59]:

$$\text{SSA} = \frac{A_{\text{cond}}}{m_p} = - \frac{d \left[\ln(T_p - T_g) \right]}{dt} \frac{c_p 4k_B T_g}{\alpha_T k_B \sqrt{8k_B T_g / (\pi m_g)} \left(2 + \frac{\zeta_{\text{rot}}}{2} \right)} \quad (3.30)$$

The following section describes the analysis method used with LOSA characterization in this study.

2.2 Line-of-Sight Attenuation Analysis

A commonly used method of line-of-sight attenuation (LOSA) is spectrally resolved LOSA, which employs a detector capable of recording transmitted light over a wide wavelength range [65–67]. The change in intensity is described by the radiative transfer equation [60]:

$$I_\lambda(L) = I_{\lambda,0} \exp \left(- \int_0^L \kappa_{\text{ext},\lambda}(s) ds \right) + \int_0^L \kappa_{\text{abs},\lambda}(s) I_{\lambda,b} [T_s(s)] ds \quad (3.31)$$

where $I_\lambda(L)$ is the transmitted light, $I_{\lambda,0}$ is the incident light, $\kappa_{\text{ext},\lambda}(s)$ is the location-dependent extinction coefficient, $\kappa_{\text{abs},\lambda}(s)$ is the location-dependent absorption coefficient, $I_{\lambda,b}$ is the blackbody intensity, and T_s is the temperature of the particle at location s . The location-dependent properties are important when

attempting to map the particle concentration and when the emission term $\left(\int_0^L \kappa_{\text{abs},\lambda}(s) I_{\lambda,b} [T_s(s)] ds \right)$ is

non-negligible or subtracted [63]; however, in this study, the emission term is subtracted and spatially resolved data is not desired. Consequently, assuming a constant absorption coefficient, a constant extinction coefficient, and sufficient mono-dispersity of the particles, Eq. (3.31) can be simplified to:

$$I_\lambda(L) = I_\lambda(0) \exp(-\kappa_{\text{ext},\lambda} L) \quad (3.32)$$

In the Rayleigh regime, $\kappa_{\text{ext},\lambda} = \kappa_{\text{abs},\lambda}$ as scattering is negligible compared to absorption for the particles in this work. The absorption coefficient is defined by [67]:

$$\kappa_{\text{abs},\lambda} = C_{\text{abs},\lambda} n_p \quad (3.33)$$

where $C_{\text{abs},\lambda}$ is the absorption cross-section of the particle as defined by:

$$C_{\text{abs},\lambda} = \frac{\pi d_p^2}{4} Q_{\text{abs},\lambda} \quad (3.34)$$

From Eq. (3.12) it can be seen that $Q_{\text{abs},\lambda}$ is a function of x_p and $E(m_\lambda)$ which is a function of m_λ . This relationship can be further expanded to include the complex dielectric function (permittivity) of the particle, $\varepsilon_\lambda = \varepsilon_\lambda' + i\varepsilon_\lambda''$, where ε_λ' and ε_λ'' are the real and imaginary indices of the dielectric function. The complex refractive index, $m_\lambda = n_\lambda + ik_\lambda$, where n_λ and k_λ are the real and complex indices of refraction, can be related to ε_λ by [76]:

$$n_\lambda = \sqrt{\frac{\sqrt{(\varepsilon_\lambda')^2 + (\varepsilon_\lambda'')^2} + \varepsilon_\lambda'}{2}} \quad (3.35)$$

$$k_\lambda = \sqrt{\frac{\sqrt{(\varepsilon_\lambda')^2 + (\varepsilon_\lambda'')^2} - \varepsilon_\lambda'}{2}} \quad (3.36)$$

The complex dielectric function for particles is effectively described using the Lorentz-Drude model: where the Lorentz component treats the electrons and ions of the particles as harmonic oscillators (springs) driven by electromagnetic fields and the Drude component accounts for free electrons by modelling the spring with a vanishing spring constant [76]. In this model, the Lorentz component accounts for the behaviour of bound electrons, with each electron transition described by:

$$\varepsilon_\lambda = \varepsilon_0 + \frac{\omega_p^2}{\omega_0^2 - \omega^2 - i\gamma\omega} \quad (3.37)$$

where ϵ_0 is a constant representing the effect of higher frequency oscillators, ω_0 is the resonant frequency, ω is the frequency of the incident wave, γ is the damping factor, and ω_p is the plasma frequency as described by:

$$\omega_p = \sqrt{\frac{e^2 n_c}{m_e \gamma_0}} \quad (3.38)$$

where e is the electron charge, n_c is the electron number density, m_e is the electron mass in vacuum, and γ_0 is the permittivity constant in a vacuum. The plasma frequency is the natural frequency at which free electrons oscillate at, while the resonance frequency is the frequency at which the electron will oscillate with the maximum amplitude. For particles with multiple resonance frequencies a multiple-oscillator model can be used [76]:

$$\epsilon_\lambda = \epsilon_0 + \sum_j \frac{\omega_{p,j}^2}{\omega_{0,j}^2 - \omega^2 - i\gamma_j \omega} \quad (3.39)$$

where the j^{th} term refers to a specific resonant frequency of the particle. For mobile electrons, the electrons can be excited with small energies. This can be modelled by “clipping the spring” or setting the resonant frequency to be 0, modifying Eq. (3.37) to:

$$\epsilon_\lambda = \epsilon_0 - \frac{\omega_p^2}{\omega^2 + i\gamma\omega} \quad (3.40)$$

which is the Drude component of the model. For ω_p in the Drude component, Eq. (3.38) still applies; however, an effective electron mass (m_d) is used. A visual representation of the Lorentz-Drude model is shown in Figure 2-5.

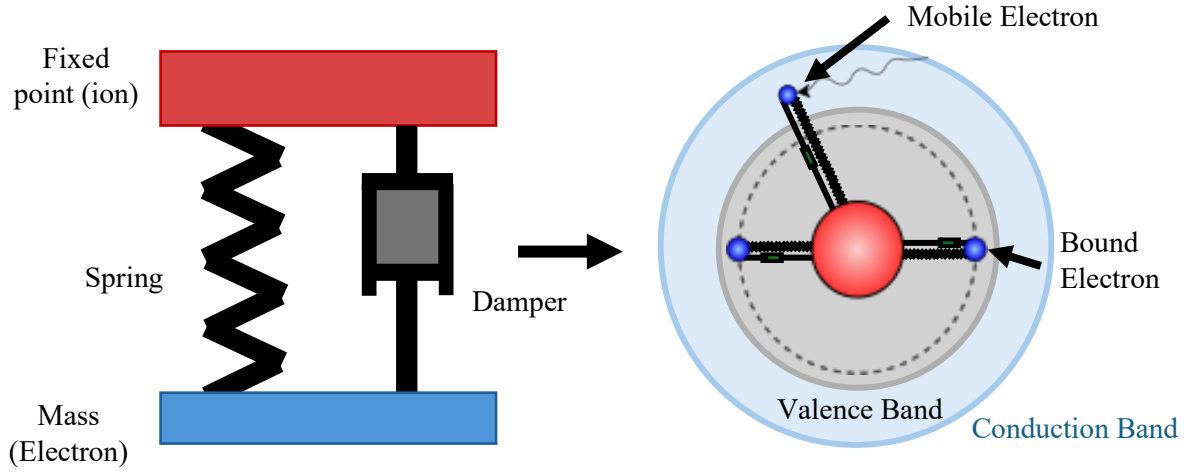


Figure 2-5: Visual representation of Lorentz-Drude model

Together the Lorentz-Drude model for a particle can be described by [76]:

$$\varepsilon_{\lambda} = \varepsilon_0 - \frac{\omega_{p,d}^2}{\omega^2 - i\gamma_d\omega} + \sum_j \frac{\omega_{p,j}^2}{\omega_{0,j}^2 - \omega^2 - i\gamma_j\omega} \quad (3.41)$$

The functionality of a particle can be derived using the relationship between the dielectric function and electrical conductivity [87]:

$$\varepsilon_{\lambda}'' = \frac{\sigma_{\lambda,e}}{2\pi\omega\gamma_0} \quad (3.42)$$

where σ_e is the electrical conductivity of the particle. The electrical conductivity is a function of wavelength and changes over time until the long wavelength limit ($\lambda > 6 \mu\text{m}$) where $\sigma_{\lambda,e}$ converges to a constant value known as the direct current (DC) conductivity (σ_{DC}).

2.3 Summary

This chapter has detailed the TiRe-LII heat transfer model and described the use of optical pyrometry to determine particle temperatures from the incandescent signals. It has also discussed the Mie and Rayleigh

theories as methods of determining the scattering and absorption efficiencies of a particle. The heat transfer model was simplified to focus on low fluence TiRe-LII and heat conduction, aligning with the primary objective of determining the specific surface area (SSA). The SSA was simplified to present a closed-form method applicable within the free molecular and Rayleigh regimes, as will generally be the case in this work. This model will be applied in conjunction with the experimental apparatus described in the following chapter.

Additionally, the LOSA extinction/absorption model was presented, based on the radiative transfer equation. The equation was simplified removing the spatially resolved aspect, deemed unnecessary for this work. The radiative transfer equation was then connected to the dielectric function, with the Lorentz-Drude model employed to connect the dielectric function to electrical conductivity of the particles. This relationship will be utilized to derive and compare the electrical conductivity of particles directly from LOSA measurements, as discussed in the context of a UV-vis spectroscopic study and an LOSA set-up with a plasma reactor described in the next chapter.

Chapter 3

Reduced graphene oxide, TiRe-LII, and LOSA experimental apparatuses

Four main experimental systems were used in this work. These include the apparatus used to synthesise reduced graphene oxide (rGO), a four-colour time-resolved laser induced incandescence (TiRe-LII) apparatus, a plasma reactor line of sight attenuation (LOSA) apparatus, and series of *ex situ* characterization systems. This chapter details the design and set-up of the rGO synthesis apparatus, TiRe-LII apparatus, and plasma reactor LOSA apparatus, while the *ex situ* characterization systems are detailed in Chapter 4.

3.1 In-line synthesis of reduced graphene oxide

A method for synthesizing reduced graphene oxide (rGO) was developed with the goal of designing a fully in-line system for producing graphitic oxide (GTO). However, in this work, a two-step process was utilized as a proof-of-concept: graphene oxide (GO) powder was first synthesized and then thermally reduced into rGO using a tube furnace. This approach allowed the separate synthesis of GO and rGO, facilitating the development and optimization of each step before implementation of the fully integrated in-line system.

3.1.1 Synthesis of graphene oxide

Graphene oxide (GO) was synthesized using graphite flakes. The graphite flakes were oxidized following the improved Hummer's method, involving the dispersion of a mixture of graphite flakes and potassium permanganate (KMnO_4) into a 9:1 acidic solution of sulfuric acid (H_2SO_4) and phosphoric acid (H_3PO_4) [23]. This produces a slurry that is stirred for 12 hours. Subsequently, the mixture is sifted through a U.S standard sieve, filtered, and centrifuged. The resulting solid material is washed with water, HCL, and ethanol to yield graphitic oxide (GTO).

The GTO is then dispersed in water and processed through a spray drier. Spray drying effectively exfoliates the GTO [88], leading to the formation of 3D crumpled structures due to the capillary compression during aerosol evaporation [14,89]. Crumpled GO is desirable due to its aggregation and compression resistance in powder form, facilitating easy redispersion and aerosolization for subsequent measurements without forming aggregate structures. This characteristic makes it ideal for external characterization.

Furthermore, the crumpled morphology ensures that during processes such as thermal reduction in a tube furnace, reaggregation is minimized, resulting in individual crumpled rGO particles. Crumpled rGO structures have been shown to possess higher specific surface areas and greater stability, as shown in Figure 3-1, making them desirable for energy storage applications such as batteries and superconductors [14].

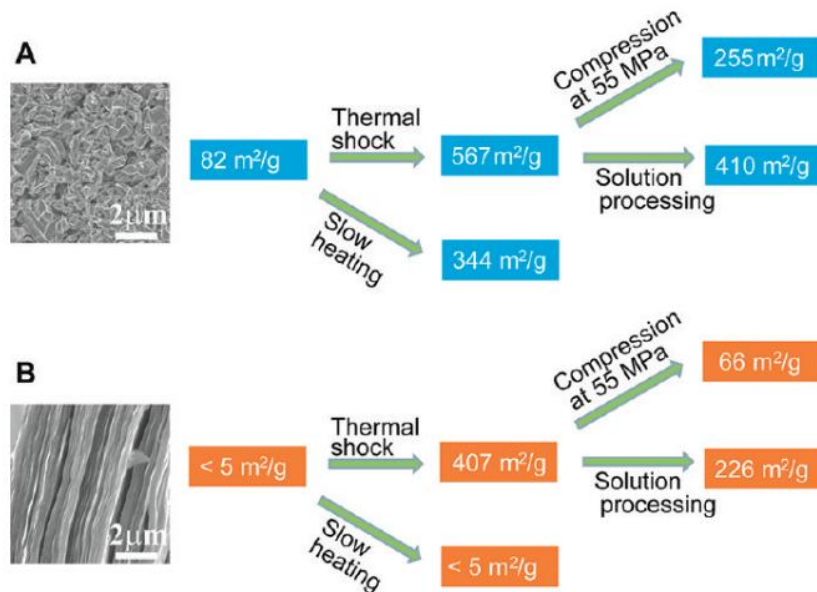


Figure 3-1: Evolution of SSA for a) crumpled GO particles and b) sheet-like GO throughout processing conditions: heating, solution processing, and mechanical compression [14]

A schematic of the process used to develop the GO powder is shown in Figure 3-2:

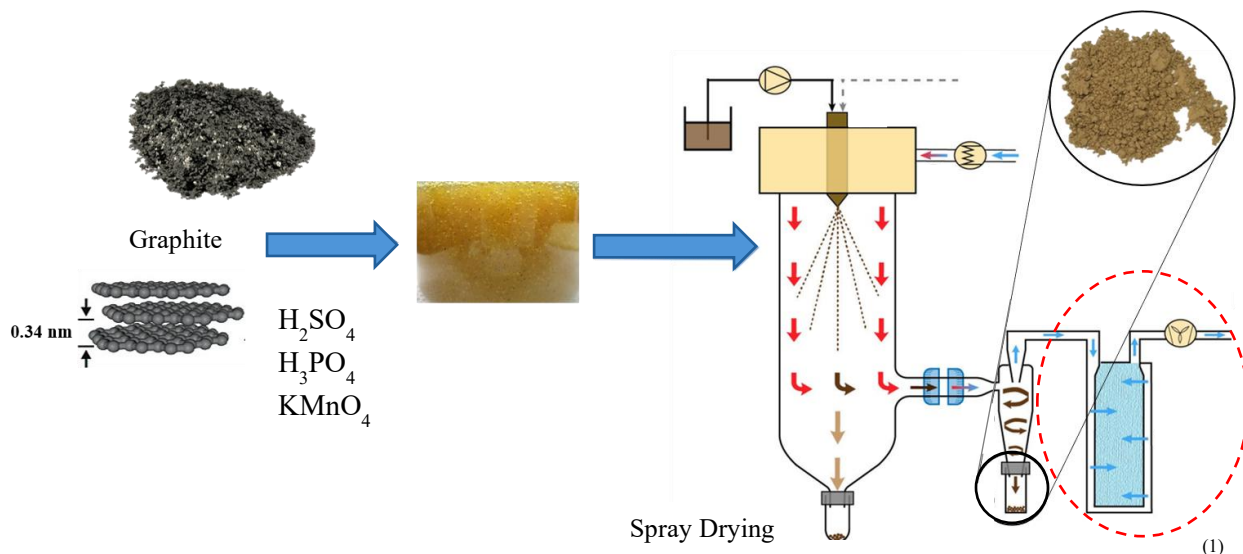


Figure 3-2: Schematic of GO powder synthesis: Note (1) is not currently used but can be used to connect to tube furnace reduction in the future

The powder produced through this method was utilized for *ex situ* characterization, as described in Chapter 4, and served as the starting material for thermal reduction.

3.1.2 Thermal reduction to rGO

The synthesized GO powder can be used for external characterization or aerosolized for thermal reduction. This aerosolization process was carried out using a custom dry powder nebulizer, which consists of three distinct stages. The initial stage is a large conical section that houses the GO powder atop a semi-permeable filter. A 2.8-watt DC computer fan is centrally installed within the conical section to assist the flow of argon gas which serves as the motive force. As argon passes the filter, it entrains the GO powder, creating an aerosol. The fan operates at 12V supplied by a DC power source. After aerosolization, the flow through the subsequent two stages gradually decreases in size to minimize particle losses. Clamps and gaskets securely connect the components, ensuring no leakage. Figure 3-3 and Figure 3-4 provide a schematic and a physical image of the nebulizer, respectively.

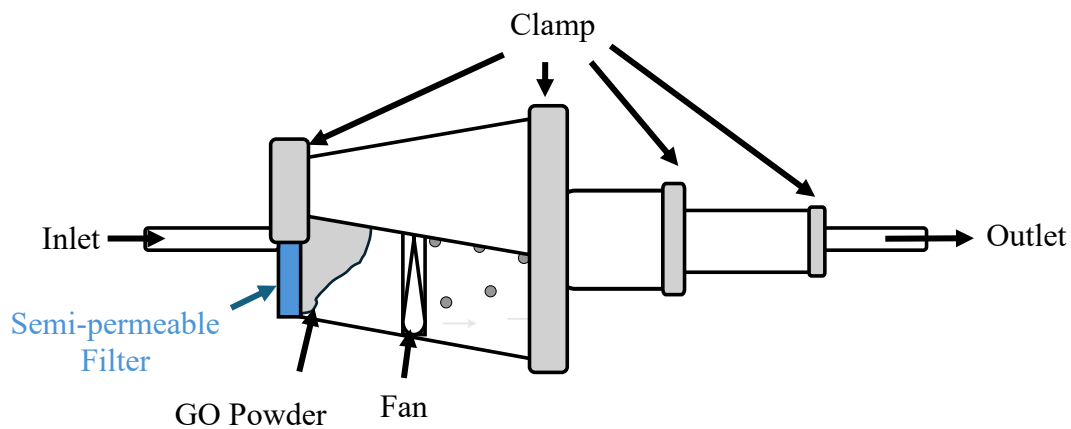


Figure 3-3: Schematic of Dry Nebulizer Fan



Figure 3-4: Physical image of the nebulizer

The aerosolized GO is directed through a ceramic tube encased within a tube furnace (Carbolite STF 16/180), which can reach 1500°C. The furnace utilizes silicon carbide elements arranged around the

ceramic tube, ensuring uniform heating of the tube surface [90]. This set-up facilitates rapid reduction of the GO into rGO.

Subsequently, the rGO is collected on a semi-permeable filter. The collection system consists of two stages that gradually increase the piping diameter to accommodate a larger filter, thereby maximizing the collected rGO. Note that some material loss may occur due to rGO adhering to the tubing at all stages of the reduction, particularly at points where the tubing diameter changes. The argon gas is vented directly into an exhaust system. A schematic representation of the entire thermal reduction process is shown in Figure 3-5.

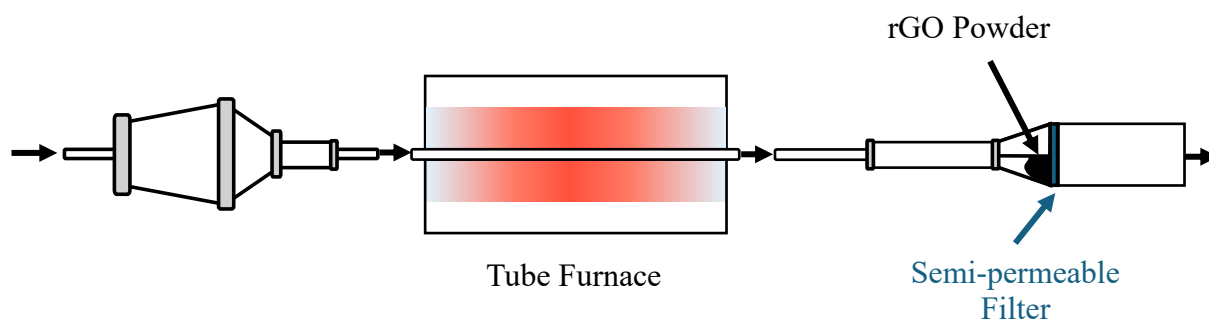


Figure 3-5: Schematic for thermal reduction

The thermal reduction process was connected to a four-colour TiRe-LII apparatus positioned downstream of the tube furnace for online analysis.

3.2 TiRe-LII four colour experimental apparatus

The TiRe-LII experimental apparatus used in this work is a two-colour TiRe-LII system obtained from the National Research Council of Canada (NRC). The characterization and initial modification into a three-colour TiRe-LII system was carried out by a prior student, Stephen Robinson-Enebeli, and is detailed in his thesis [74]. This section will detail the components of the excitation and detection system, the modification of the system into a four-colour TiRe-LII system and a brief description of its operation.

3.2.1 TiRe-LII excitation system

The TiRe-LII system consists of an excitation system and detection apparatus. The excitation system includes a pulsed laser, an optical chain, a sample cell where the aerosol is introduced, and detection optics. A schematic of the excitation system is shown in Figure 3-6 and an image of the actual system is shown in Figure 3-7.

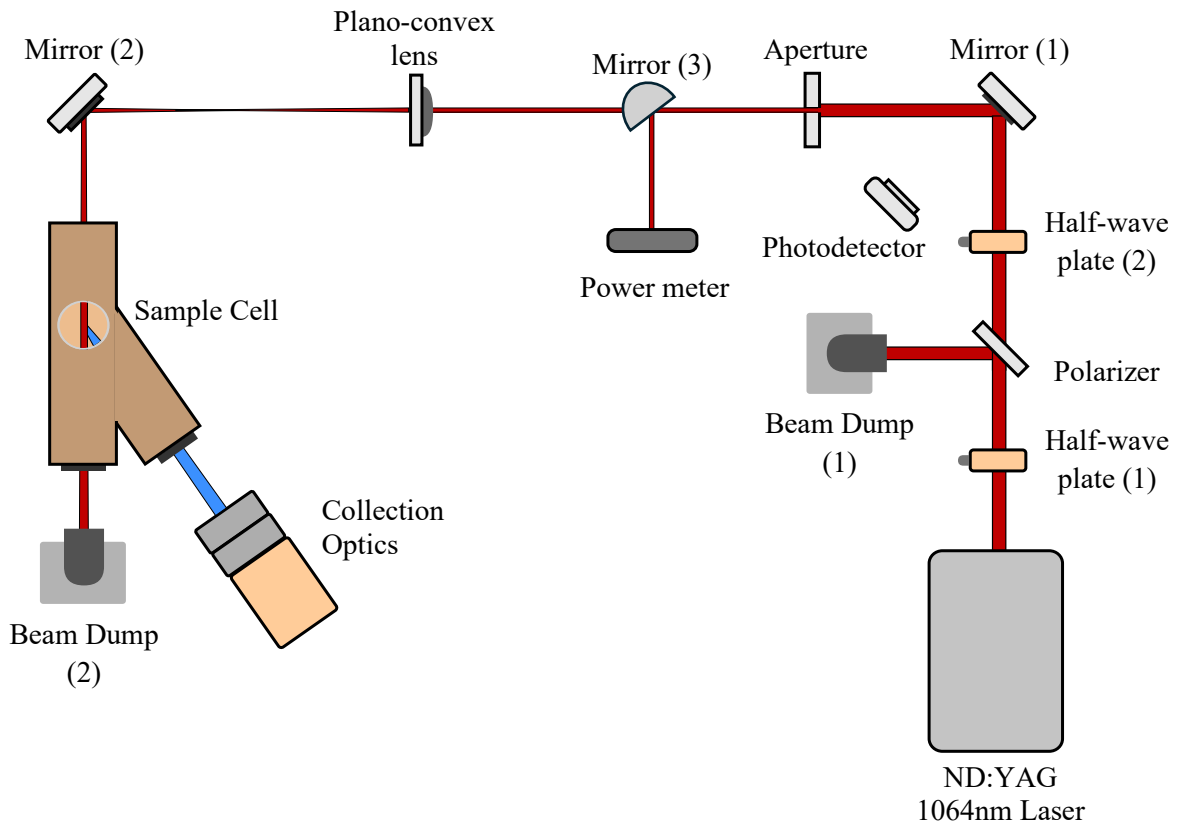


Figure 3-6: Schematic of excitation system of TiRe-LII

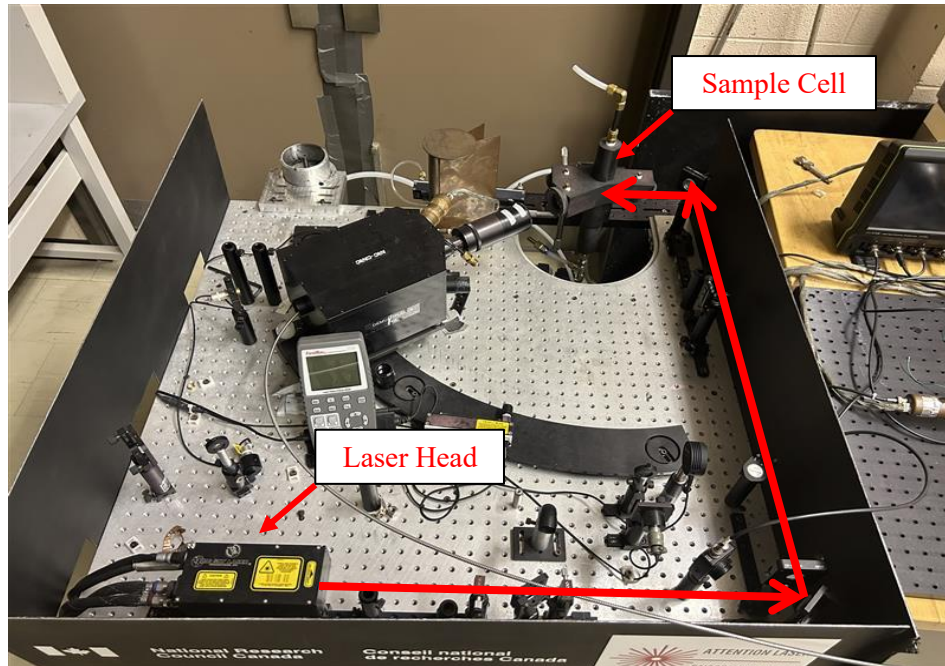


Figure 3-7: Physical image of the LII detection set-up

The laser source is a neodymium-doped yttrium aluminum garnet (Nd:YAG) 1064 nm pulsed laser (Big Sky Ultra CFD laser system), which operates by flashing a rare gas-filled lamp at a controlled pulse repetition frequency (PRF) near a Nd:YAG laser rod. The radiation from the lamp is partially absorbed by the laser rod, converting it into stored energy within the excited state of the neodymium ion. The energy can be extracted through control of the spontaneous emission (hold off) and stimulated emission (Q-Switching). The delay of the Q-switch allows laser energy to accumulate within the system overcoming losses within the oscillator. The laser output consists of identical photons, making the beam highly directional, pure, and coherent [91]. The laser system consists of a laser head and an integrated cooling and electronics (ICE) unit, which is used to set the Q-switch delay and PRF. The Q-switch is set to 135 μs while the PRF is set to 20 Hz. As tested by Robinson-Enebeli [74], the maximum output energy is approximately 7.5 mJ at the particle location (probe volume) and a laser time profile $F(t)$ with a full-width half-max (FWHM) of 8 ns is found. This is shown in Figure 3-8.

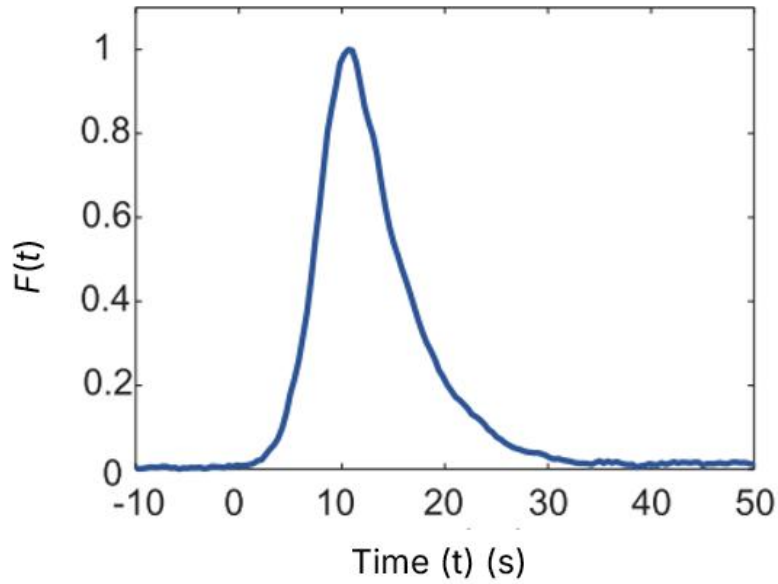


Figure 3-8: Laser temporal profile [74]

The laser is directed to the probe volume using a series of optical components. Two half-wave plates and a polarizer are employed to attenuate the laser power. The first half wave plate converts the vertical polarization of the laser into both horizontal and vertical components; this can be adjusted using a control knob. The polarizer then directs the vertically polarized light to a beam dump while allowing the horizontally polarized light to pass through. The second half wave plate modifies the horizontally polarized light back into vertically polarized light, aligning with the design of the sample cell to minimize the reflectivity of vertically polarized light. The laser beam is then reflected off a 90° mirror where a photodetector is positioned. This photodetector triggers whenever the laser beam passes, prompting the detector system to record a signal. The laser beam then passes through an aperture consisting of a $2 \text{ mm} \times 1.5 \text{ mm}$ ceramic slit. The slit serves to reduce the size of the beam, allowing only the center portion of the beam through. This promotes a spatially uniform beam fluence, as the edges are more prone to diffraction. Such uniformity ensures uniform heating of the particles at the probe volume, thus maintaining the accuracy of the TiRe-LII measurement [92]. A plano-convex lens with a focal length of 250 mm is then placed half-way between the slit and the probe volume to achieve a 1:1 magnification. Consequently, the cross-sectional area at the probe volume is approximately $2 \text{ mm} \times 1.2 \text{ mm}$. This was validated using a

coherent beam laser-cam as demonstrated by Robinson-Enebeli [74]. A second 90° mirror was placed to direct the laser beam into the sample cell. An additional movable 90° mirror is positioned between the aperture and plano-convex lens. This mirror can be flipped to redirect the laser beam into a power meter (Coherent FieldMax II TOP) for measuring the laser power. When performing TiRe-LII measurements, the mirror is folded down to allow the beam to pass.

The sample cell consists of a laser beam inlet, laser beam outlet, detection optics outlet, aerosol inlet and aerosol outlet. The laser beam inlet, laser beam outlet, and detection optics outlet are each fitted with fused silica glass windows set at Brewster's angle to minimize reflection. The laser beam inlet and outlet are aligned along the same path, while the detection optics outlet is positioned at a 35° forward scattering angle relative to the beam's direction. The aerosol inlet and outlet are perpendicular to the laser beam inlet and outlet with the inlet at the top of the cell and the outlet at the bottom of the cell. Figure 3-9 provide top and side views showing the design of the sample cell.

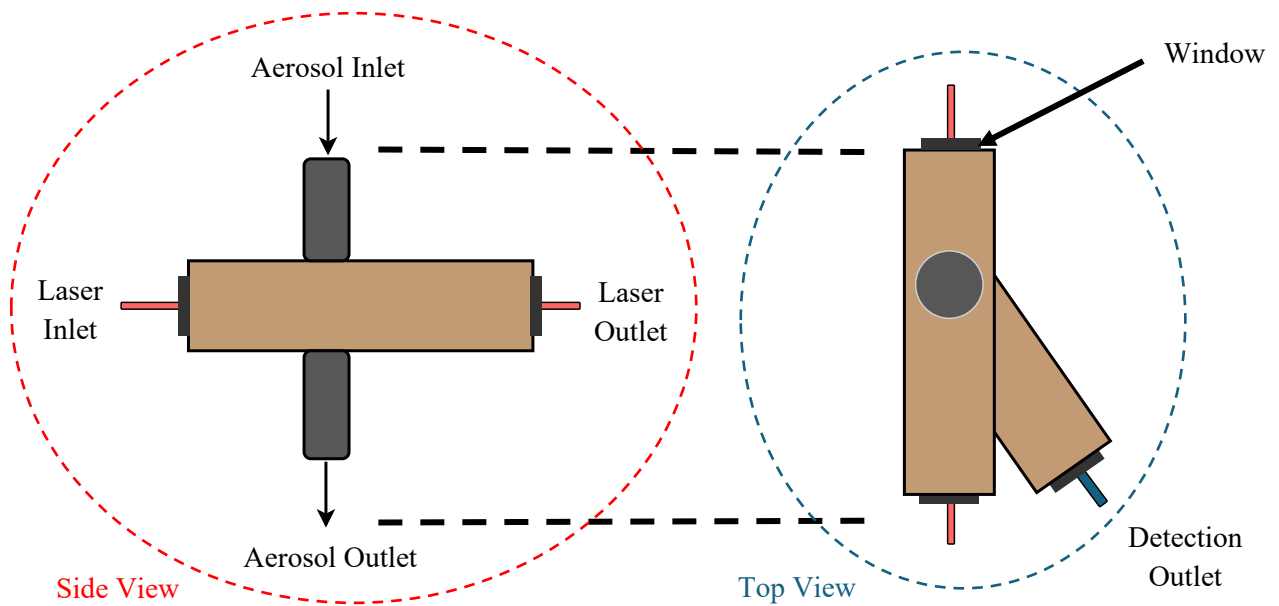


Figure 3-9: Aerosol Sample Cell: Side and Top View

The collection optics focus on the probe volume and consist of two 50 mm diameter achromatic lenses with focal lengths of 210 mm and 100 mm. The signal is magnified by a factor of two and focused onto a

40 mm diameter lens which collimates and further images the signal into a fibre optic cable, transmitting it to the detection apparatus.

3.2.2 TiRe-LII detection apparatus

The original detection apparatus consisted of three photomultiplier tubes (PMTs) equipped with bandpass filters centered at wavelengths 447 nm, 625 nm, and 747 nm; however, it was determined by Robinson-Enebeli that the PMT at 625 nm was ineffective due to unreliable calibration and high noise. The original set-up is shown in Figure 3-10.

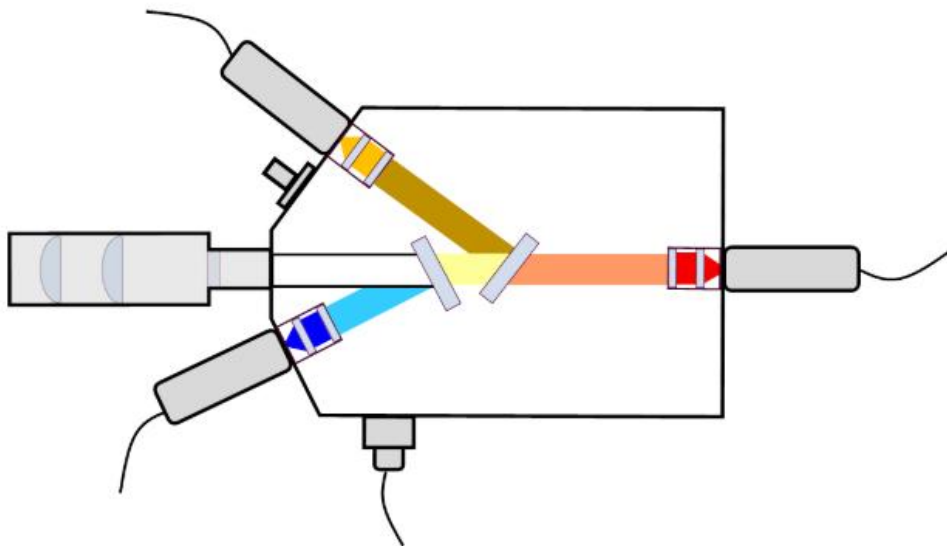


Figure 3-10: Three-colour LII detection apparatus [74]

Subsequent modifications were implemented to enhance the system's sensitivity and accuracy by reconfiguring the apparatus and adding a fourth PMT. The updated detection apparatus consists of a four-colour PMT set-up, voltage gains boxes, and an oscilloscope.

Photomultiplier tubes amplify the incident light signal based on the photoelectric effect and secondary emissions. As the light enters the PMT, it strikes a photocathode, causing the release of electrons (photoemission). The electrons are then focused and accelerated by electrodes onto dynode stages, which subsequently excite more and more electrons resulting in signal amplification. The

electrons are then collected at an anode, inducing a measurable current [93]. A schematic of a PMT is shown in Figure 3-11.

Each PMT contains a power supply and voltage divider circuit. Ideally, PMT signal output is proportional to the intensity of the incident light. However, PMTs can exhibit non-linear behaviour due to factors such as photocathode resistivity increasing with incident photon flux, excessive electron multiplier gain leading to space-charge effects limiting the anode current [94], and non-linear responses at low levels of light intensity [95].

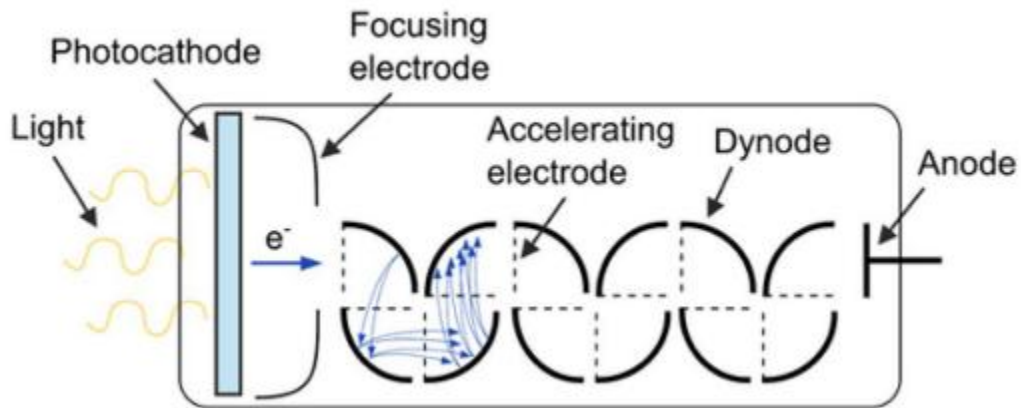


Figure 3-11: Schematic of PMT [94]

Four PMTs (Hamamatsu H5783-01/03 bialkali photosensor module) are used in the detection apparatus to capture signals at four distinct wavelengths. Incoming light is first separated into specific wavelength ranges and further narrowed using sets of dichroic mirrors and bandpass filters. Dichroic mirrors divide light into two wavelength ranges by utilizing thin-film interference to reflect light below a certain threshold while transmitting longer wavelengths. In this apparatus, three dichroic mirrors are used with cutoff wavelengths at 490 nm, 567 nm, and 685 nm. The light is then directed into the PMT tube housing.

To further refine the wavelengths selection, bandpass filters are placed at the entrance of each PMT housing. The bandpass filters are centered at 447 nm, 545 nm, 645 nm, and 747 nm, with spectral

widths of ± 16 nm, ± 32.5 nm, ± 45 nm, and ± 35 nm, respectively. Following the filters, plano-convex lenses with 50 mm focal lengths focuses the light onto the corresponding PMTs. The PMTs are encased in a copper housing to minimize electrical noise. A schematic of the PMT tube housing is shown in Figure 3-12 (a).

Neutral density (ND) filters are positioned before the dichroic mirrors to allow for additional attenuation of the light if necessary. The ND filters have transmission levels of 86%, 57%, 29%, 11%, and 2% are mounted on a wheel for quick modification and selection of the desired filter. Note that the 2% ND filter was not used due to non-linearities across different wavelengths. The overall schematic for the detection apparatus is shown in Figure 3-12 (b) and a physical image of the detection apparatus is shown in Figure 3-13.

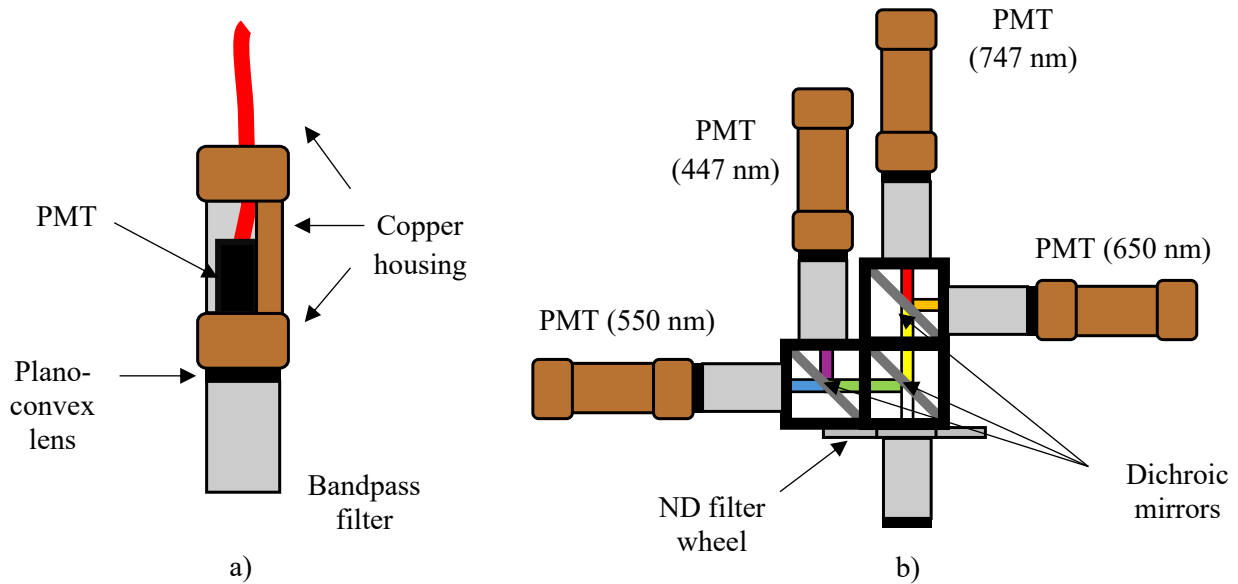


Figure 3-12: a) schematic of PMT tube housing. b) schematic of full detection apparatus

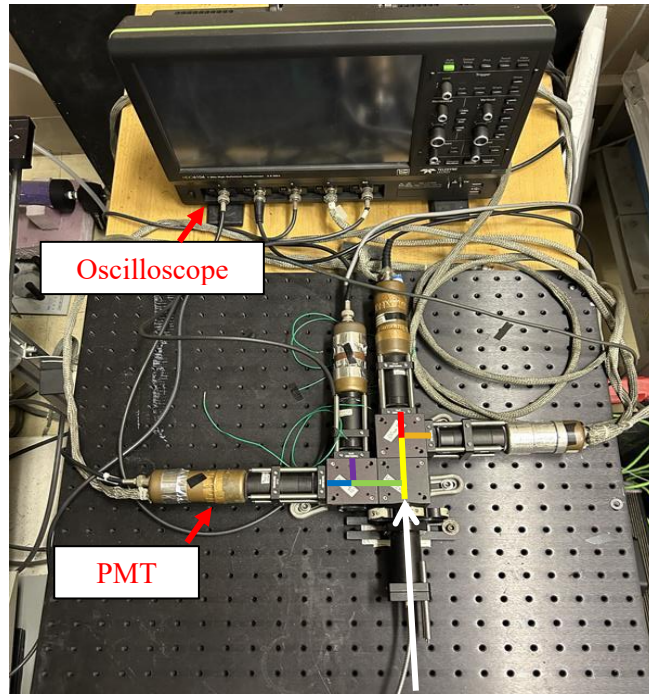


Figure 3-13: Physical image of LII detection system

The PMTs are connected to a voltage box and an oscilloscope (HDO6104 1 GHz High-Definition Oscilloscope – Teledyne). The voltage box applies a set voltage to the voltage divide circuit within the PMTs, adjusting the electron gains and, consequently, the output signal. The oscilloscope converts the PMT induced currents into digitized voltage readings using a 50 Ω coupling. It is externally triggered by the photodetector, as shown in Figure 3-6, and records all four PMT signals until the subsequent laser pulse, producing temporally resolved signals for each laser pulse. Calibration is essential to correlate the voltage readings from each PMT and their respective voltage gains. The calibration method applied to the system is discussed in Appendix A.1.

While the TiRe-LII system was established in the University of Waterloo, the necessary equipment to develop an LOSA experimental apparatus was unavailable. Consequently, a research trip was undertaken to the University of Duisburg-Essen (UDE) in Duisburg, Germany to conduct an online study on plasma-reduced graphene oxide (rGO).

3.3 Plasma reactor-LOSA experimental apparatus

The line-of-sight attenuation (LOSA) measurements conducted in this study used a plasma reactor apparatus at the University of Duisburg-Essen (UDE). Synthesis of rGO via a plasma reactor is a candidate route for scalable production and is currently being studied at UDE. Consequently, only minor modifications to the plasma inlet was required, while the LOSA system remained unchanged.

The plasma region generates a high-temperature environment sufficient to transform GO to rGO. However, accurately determining the plasma region's temperature is challenging due to complex interactions between the motive gas and plasma. Additionally, little is known about how the plasma may affect the mechanisms of GO reduction and the resulting rGO. Nevertheless, the successful reduction of GO to rGO is evident from the collected powder's characteristics; the resulting powder was black (as opposed to GO being light brown) as shown in Figure 3-14. Additionally, elemental analysis was carried out using an elemental analyzer (Eltra ELEMENTRAC ONH-p), revealing an oxygen percentage of 8.27%, whereas the GO prior to reduction had an oxygen percentage of 33.81%. While the rGO synthesized using the plasma reactor may differ from that of the tube furnace in some unknown way, this method serves as a valid proof of concept for employing the LOSA technique to characterize rGO.

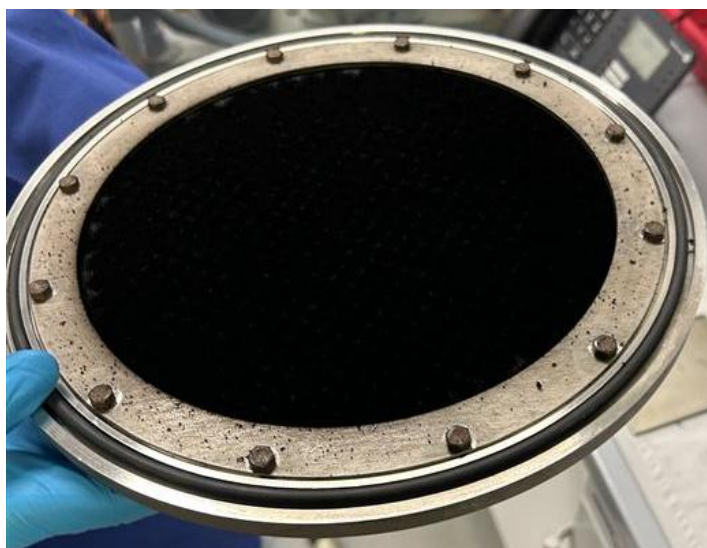
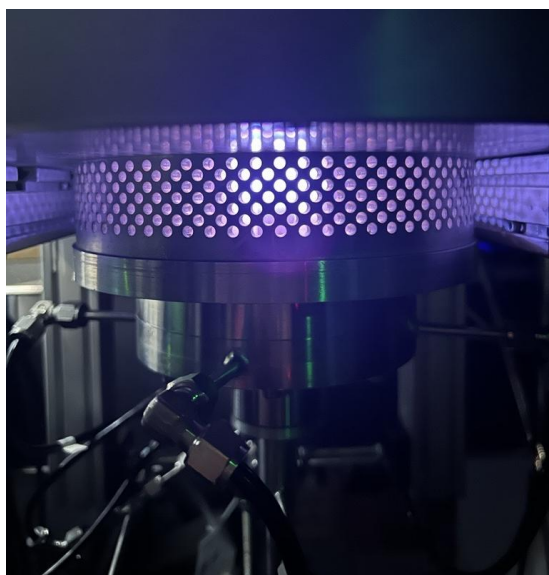
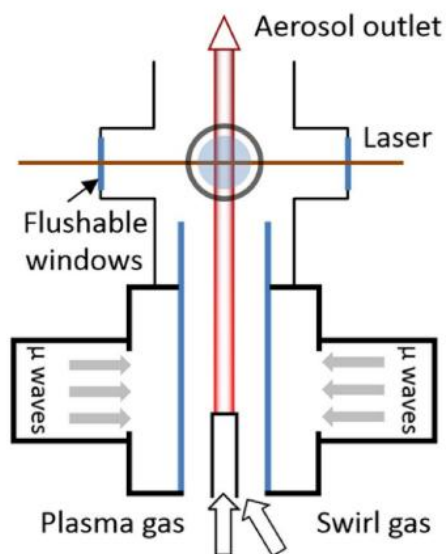


Figure 3-14: Plasma-synthesized rGO on collection filter

The plasma reactor used is described in detail by Sipkens et al. [96] and Menser et al. [73]. To accommodate graphene oxide (GO), the inlet of the plasma gas was modified to integrate a nebulizer identical to the one depicted in Figure 3-3. The nebulizer dispersed GO powder using argon and nitrogen as the motive gases during the reaction. A bypass was incorporated upstream of the nebulizer, allowing argon and nitrogen to flow without carrying GO powder. The reactor itself remained unaltered, operating with plasma gas exiting a nozzle into the main chamber, which consists of a quartz tube. The plasma gas is stabilized into a 12 mm diameter cylindrical torch using a mixture of argon and hydrogen gas (swirl gas). A circular microwave resonator (IPLAS, Cyrannus) generates microwave radiation at the center of the 7.7 cm quartz tube, producing a visible purple plasma as shown in Figure 3-15 (a). The plasma gas then travels 300 mm downstream to the probe volume, located at the intersection of four optical access windows. These windows facilitate the entry and exit of incident light used for LOSA measurements, allowing for interaction with the gas at the probe volume. A schematic of the reactor is shown in Figure 3-15 (b). Beyond the probe volume, the plasma gas exits the reactor, the motive gas is exhausted, and the powder is collected onto a semi-permeable filter.



a)



b)

Figure 3-15: a) Glowing plasma of Ar/H₂ b) Schematic of plasma reactor [73]

The laser system consists of a laser drive light source (LDLS), and optical components for directing light to the probe volume and magnifying and focusing the transmitted light. Additionally, a spectrograph was used for recording the spectrally resolved transmitted light. The LDLS (Energetiq, EQ-77) is a stable broadband lamp source that operates by using a focused laser beam to sustain a plasma within a xenon filled bulb, thereby exciting the gas [97]. Light from the LDLS is collimated using an off-axis parabolic mirror and directed into an aperture that reduces beam size. The light is then focused onto a 90° mirror using a plano-convex lens (50mm focal length). This mirror reflects the light into an integration sphere (IS) which collimates the incoming light. An adjustable aperture is placed directly after the IS allowing the incident light to be blocked when necessary. When opened, the light from the IS is focused into the probe volume using two plano-convex lenses with focal lengths of 300 and 100 mm, respectively. The transmitted light is subsequently focused onto a periscope assembly using two plano-convex lenses with 150 mm and 50 mm focal lengths, respectively. The periscope assembly consists of two 90° mirrors to lower the height of the light beam. A final plano-convex lens with a focal length of 20 mm is used to focus the light into the spectrograph (Teledyne IsoPlane SCT 320). A schematic of the optical set-up is shown in Figure 3-16.

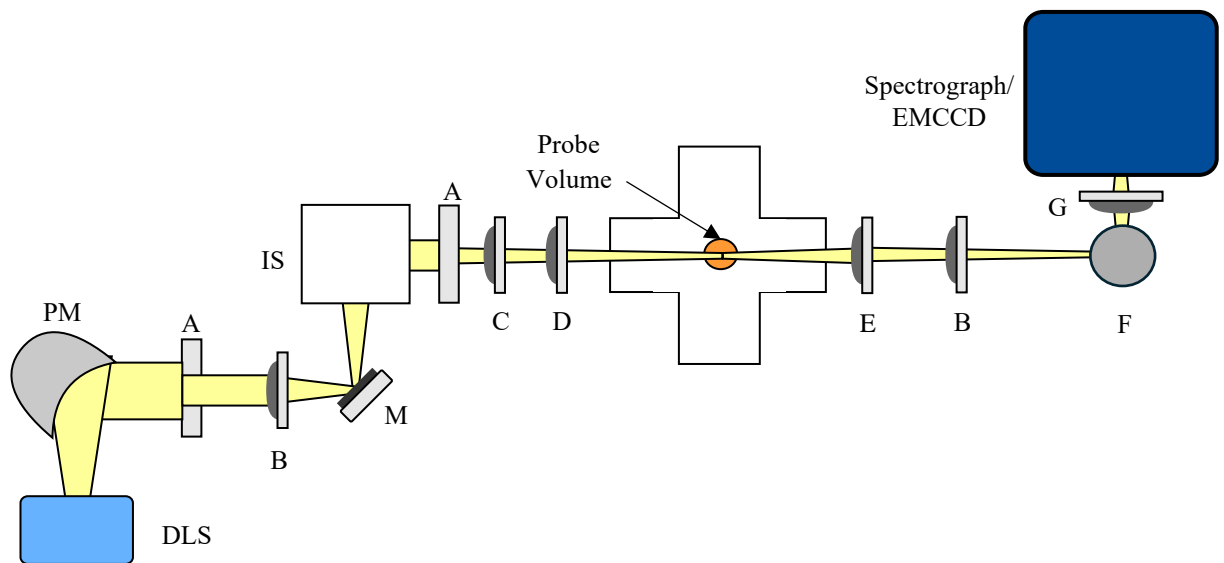


Figure 3-16: Schematic of Plasma-LOSA optical setup. LDLS: laser-drive light source, PM: Parabolic Mirror (effective focal length 50mm), A = Apertures, B = Plano-convex lens (focal length 50mm), M = 90° mirror, IS = integrating sphere, A = aperture, C = Plano-convex lens (focal length 300 mm), D = Plano-convex lens (focal length 100 mm), E = Plano-convex lens (focal length 150 mm). Spectrograph used is a IsoPlane SCT 320

The IsoPlane SCT 320 is a spectrograph with a 320 nm focal length designed to minimize optical aberrations and enhance spectral resolution [98]. It uses gratings to split the incoming light into its constituent wavelengths, which are spatially separated and directed onto the attached electron-multiplying charge-coupled device (EMCCD) camera (Princeton Instruments, ProEM 1600x400BX3). This configuration allows the light signal to be spectrally imaged, with each wavelength corresponding to a value on the x-axis. By averaging the pixel values on the y-axis, the light intensity can be estimated at different wavelengths [99]. A sample plot from the EMCCD camera can be seen in Figure 3-17. The calibration procedure needed to correlate the x-axis pixels to the corresponding wavelength is detailed in Appendix A.2.

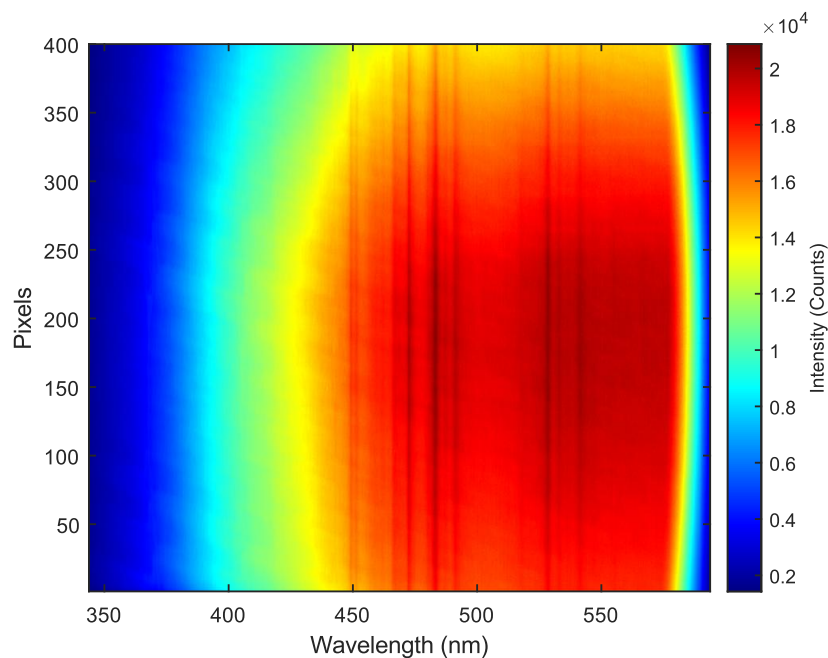


Figure 3-17: EMCCD colourmap of wavelength vs y-pixels in terms of intensity (counts)

3.4 Summary

This chapter outlined the method for synthesizing reduced graphene oxide from graphite, detailed the four colour TiRe-LII set-up used, and described the plasma reactor-LOSA apparatus. The GO oxidation and drying processes produced the GO powder used for characterization in this work. The tube furnace

reduction system shows high potential for large scale rGO synthesis; therefore, it will serve as the primary system for testing and designing *in-situ* methods. The TiRe-LII set-up was elaborated upon, including the optical network within the excitation and detection systems. The modification from a three-colour set-up to a four-colour set-up was discussed, with re-calibration and validation of the new set-up presented in Appendix A.1. The TiRe-LII set-up was employed to verify whether GO and rGO can undergo incandescence, as detailed in Section 4.3, and was integrated with the tube furnace reduction system for *in-situ* measurements of rGO, as detailed in Chapter 6.

The LOSA validation was carried out at the UDE using a plasma-reactor system, as the necessary testing equipment was unavailable in Waterloo. Plasma-reactor reduction is a feasible synthesis route for high-yield production of rGO; however, is not the focus of this study. Although plasma-reactor reduction differs from tube furnace reduction, both are thermal reduction methods and share similar operating conditions. Therefore, it is believed that the LOSA experiments on the rGO will provide insights applicable to the tube furnace reduction process in addition to the plasma reduction process. The plasma reactor-LOSA experimental apparatus was detailed, including the plasma generation and reduction system, along with the optical components in the LOSA detection system. Calibration procedures for the spectrograph and EMCCD detection are presented in Appendix A.2. The LOSA and plasma-reactor measurements are described in detail in Chapter 7.

Chapter 4

GO ex-situ characterization experimental methods

A study conducted at the National Research Council of Canada (NRC) aimed to characterize and connect the morphology and optical properties of GO particles. Understanding these optical properties is essential to determine the applicability of absorption-based diagnostics for GO particle characterization.

Furthermore, elucidating the relationship between morphology and optical properties of the GO particles, helps determine which morphological attributes can be derived from the optical diagnostic. The focus was placed on GO rather than rGO due to the unavailability of rGO powder for analysis. The GO study serves to both enhance the understanding of GO powder and to develop a framework, identifying the most effective experimental methods and their outcomes for future rGO study.¹ This chapter describes the experimental apparatus, devices, and procedures used in this study.

4.1 Preparation and nebulization of GO particles

4.1.1 Preparation of GO particles

The material used in this study was GO powder obtained from the synthesis process outlined in Section 3.1.1. To facilitate wet nebulization, the powder was prepared into a colloid suspension following the method outlined by Paredes et al. [100]. Specifically, the GO was dispersed in deionized (DI) water at a concentration of 0.05 wt%. To ensure stability and prevent precipitation during experiments, the colloid was ultrasonicated in a bath ultrasonicator for one hour at room temperature (20°C) after initial suspension and was ultrasonicated again for 5 minutes before any subsequent measurements. Figure 4-1 presents images of both the original GO powder and subsequent colloid.

¹ This study has been submitted to the Journal of Aerosol Science in the manuscript “Investigation of morphology and optical properties of graphene oxide for online diagnostics”, co-authored by Halil Ibrahim Yazici, Dr. Joel Corbin, Dr. Rym Mehri, Dr. Timothy Sipkens, and Dr. Kyle Daun



a)



b)

Figure 4-1: a) GO powder after spray drying and b) GO colloid after the powder is dispersed in water

A sample of the colloid was drop-casted onto a holey carbon transmission electron microscopy (TEM) grid.

4.1.2 Nebulization of GO particles

The colloid was nebulized using a Collison nebulizer. A syringe pump (NewEra Instruments, Syringe ONE) controlled the flow of the colloid to the nebulizer (Blaustein Atomizing Modules (BLAM), CH technologies). Flow rate testing confirmed that particle concentration remained constant across different flow rates, leading to the selection of a constant rate of 0.1 mL/min chosen for all experiments. The atomizer was modified in-house to increase and stabilize the concentration of particles [101].

Air was used as the motive gas for aerosolization, supplied to the nebulizer at 310 kPa, resulting in an aerosol flow rate of 2.7 standard litres per minute (slpm). To reduce water concentration and remove unwanted particles, the flow was diluted with heated HEPA-filtered air at 90°C. Dilution was adjusted as needed based on the sensitivity of the downstream optical equipment, with a nominal dilution of 1:10. The diluted flow was then mixed using a static mixer and passed through a Nafion dryer (PermaPure

Polytube Dryer 070) and catalytic stripper (Catalytic Instruments CS015) at 350°C. The Nafion dryer removed water particles through two countercurrent gas streams, with the dry purge gas extracting water via the difference in water concentration [102]. The catalytic stripper removed semi-volatile compounds from the aerosol through oxidation while leaving solid particles unaffected [103]. This nebulization apparatus, shown in Figure 4-2, was used for all subsequent experiments and will hereby be referred to as “Nebulization”.

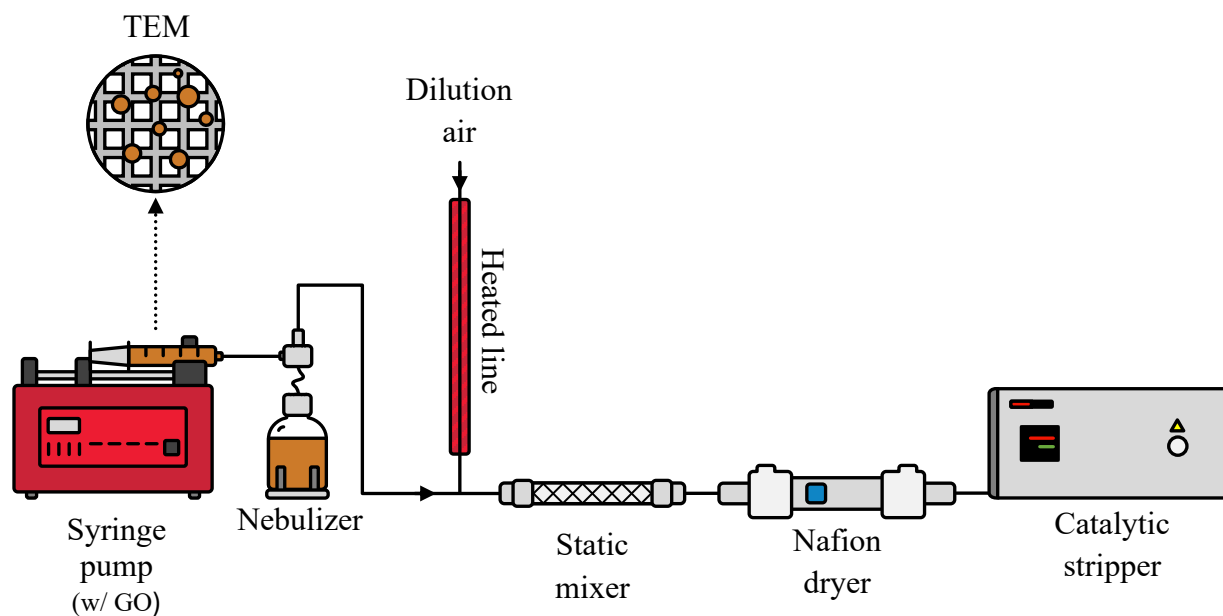


Figure 4-2: Nebulization apparatus of GO particles

4.2 Ex-situ experimental methods

4.2.1 Morphological analysis

Transmission electron microscopy (TEM, JEOL, Ltd, F200) was carried out on the drop-cast colloid prior to nebulization. Transmission electron microscopy operates by directing a beam of electrons emitted from a cold field-emission electron gun through a specimen. As the electrons interact with the sample, they are either scattered, absorbed, or transmitted, allowing for the formation of an image based on these interactions [104]. In this study, three TEM analysis methods were employed: standard bright-field TEM

imaging, selected area electron diffraction (SAED), and electron energy loss spectroscopy (EELS), which provide information on the particle morphology, crystallinity, and composition, respectively. Standard bright-field TEM imaging operates by collecting unscattered electrons that pass through the sample to form an image. Regions where electrons are transmitted with minimal scattering appear brighter, whereas regions with high scattering or absorption appear darker. This allows for the determination of particle thickness, shape, and size. Selected area electron diffraction imaging operates by using an aperture to select a small area on the sample and analyze the diffracted electrons in this area, forming a diffraction pattern. This provides information on the crystallinity and lattice parameters of the sample. Electron energy loss spectroscopy operates by firing a beam of electrons with a known energy and measuring the loss of energy through inelastic scattering. The sample composition and bonding states can be inferred from the energy loss spectrum. The TEM device used for this study is shown in Figure 4-3:

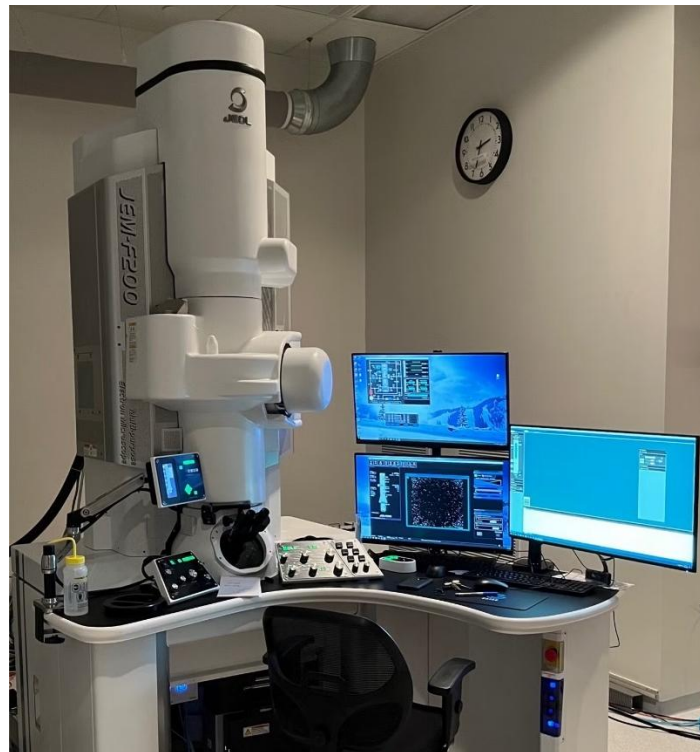


Figure 4-3: TEM present in University of Waterloo [105]

To measure the size distribution of the aerosolized GO, a scanning mobility particle sizer (SMPS, TSI Inc. 3938) is employed, consisting of an electrostatic classifier with a neutralizer (TSI Inc. 3082), a differential mobility analyzer (DMA, TSI Inc. 3081A), and a condensation particle counter (CPC, TSI Inc. 3752) [106]. The SMPS provides the mobility diameter distribution of the incoming particles by charging them using the neutralizer, whereby the DMA can then select particles of a specific size by applying a voltage. The particles enter the CPC where they are condensed onto a supersaturated vapor and counted using a light scattering detector [107]. Note that the specificity of the DMA is limited, i.e., instead of a single mobility diameter, particles of a narrow range of mobility diameters will persist through the DMA column. This can be quantified using an instrument kernel function. The components for this study are shown in Figure 4-4.

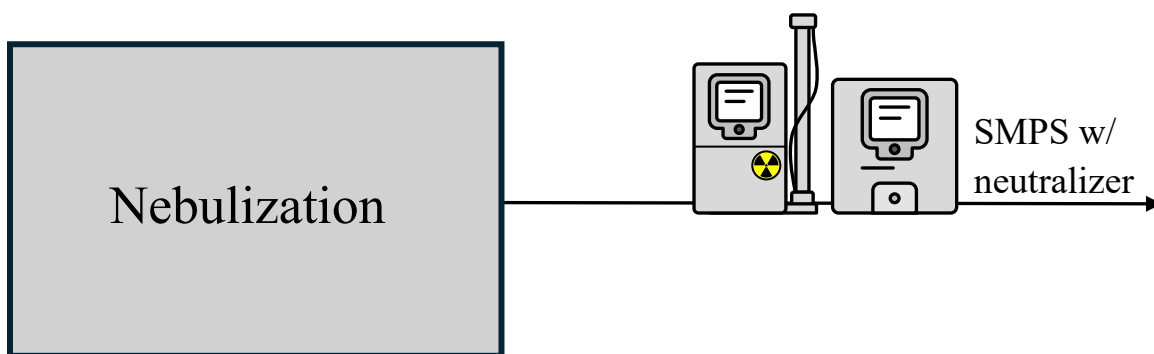


Figure 4-4: Schematic of mobility diameter distribution study.

The mobility diameter is defined as the diameter of a hypothetical sphere that exhibits the same electrical mobility as the particle in question. This parameter is widely used to determine the morphology of aerosol particles and can be utilized in conjunction with mass and material density to derive the effective density, mass mobility exponent, volume equivalent diameter, dynamic shape factor, and aerodynamic diameter [108,109]. The material density of GO is notably variable, due to differences in the number density of oxygen-containing functional groups and the presence of structural defects. Reported densities range from 1.36 g/cm³ [110] to 1.80 g/cm³ [111]. In this study, the material density of the GO

powder was not characterized. This parameter is unnecessary for determining the effective density and mass mobility exponent of the powder. Consequently, the material density is omitted from consideration, and the particle morphology was described using the effective density and mass mobility exponent.

To determine the effective density and mass mobility exponent, the mass of the particles must be known. This parameter is found using a centrifugal particle mass analyzer (CPMA, U111, Cambustion Ltd.) in conjunction with the SMPS as shown in Figure 4-5.

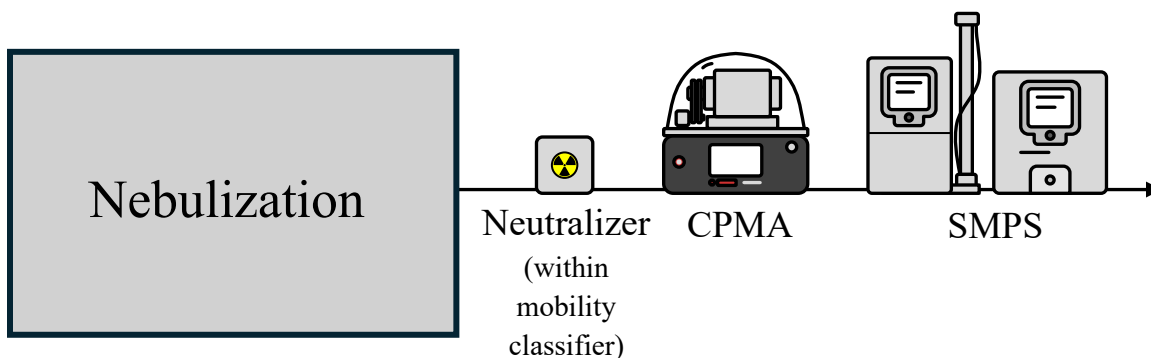


Figure 4-5: Schematic of effective density measurement apparatus.

Prior to entering the CPMA, particles are charged according to an equilibrium charge distribution by the neutralizer of the electrostatic classifier. The CPMA then classifies the particles based on their mass-to-charge ratio (m^*). The CPMA consists of two concentric rotating cylinders through which the particles flow. A voltage difference applied between the cylinders causes particles with lower m^* values to precipitate onto the inner cylinder due to charge attraction, while particles with higher m^* are driven to the outer cylinder by centrifugal forces. Only particles with a specific m^* , as determined by the instrument, will persist through the system [112]. Similar to the DMA, the CPMA's selectivity is limited and can be quantified using a kernel function. In the context of neutralizers, since a large fraction of the particles contain single charges at equilibrium, the smallest peak in the measurement corresponds to the singly charged particles, such that the m^* ratio is approximately equal to the particle mass ($m_p = m^*$). Accordingly, the CPMA may be used to generate a roughly monodisperse aerosol with a narrow mass

distribution. The classified particles then enter the SMPS, giving a mobility size distribution for each particle mass. This process allows for the determination of the effective density at different mobility diameters and the mass-mobility exponent. The effective density is derived using

$$\rho_{\text{eff}} \equiv \frac{m^*}{(\pi/6)d_m^3} = \rho_{\text{eff},100} \cdot \left(\frac{d_m}{100 \text{ nm}} \right)^{\zeta-3} \quad (5.1)$$

where d_m is the mobility diameter, $\rho_{\text{eff},100}$ is the effective density for a particle having a mobility diameter of 100 nm, and ζ is the exponent as defined by the mass-mobility relationship (mass-mobility exponent):

$m^* \propto d_m^\zeta$. This system was corrected using nebulized Santovac 5P Diffusion Pump Fluid

(Chromatographic Specialties Inc.), a perfectly spherical particle that has a defined material density [113].

The correction procedure is presented in Appendix B.1.

4.2.2 Optical analysis

The optical parameters derived from this study were the spectral absorption coefficient ($\kappa_{\text{abs},\lambda}$), the absorption Ångström exponent (AAE), the mass absorption cross-section (MAC), and the mass scattering cross-section (MSC). To determine the spectral absorption coefficient and the AAE, a combination of a cavity attenuated phase shift instrument (CAPS PM_{SSA} 450nm, Aerodyne Inc.) and an aethalometer were used.

The CAPS PM_{SSA}, 450nm works by using an LED to direct a light centered at 450 nm through the aerosol. The extinction coefficient is inferred through the phase shift of the output signal relative to the input light, while the scattering coefficient can be measured independently by collecting scattered light using a photomultiplier tube (PMT) [114,115]. The absorption coefficient of subsequent samples, $b_{\text{abs},450\text{nm}}$, is found by subtracting the scattering coefficient from the extinction coefficient,

$$\kappa_{\text{abs}} = \frac{1}{\alpha_c} \left(\kappa_{\text{ext}} - \frac{\gamma_c}{\beta_c} \kappa_{\text{sca}} \right) \quad (5.2)$$

where α_c is a geometry correction factor, β_c is a scattering cross-calibration factor, and γ_c is a truncation correction factor. The geometry correction factor is applied within the CAPS $PM_{SSA, 450nm}$ software. While the default factor is $\alpha_c = 0.73$, studies by Modini et al. [115] have determined that a factor of 0.78 is more appropriate for CAPS $PM_{SSA, 450nm}$ instruments and consequently, was used in this study. The scattering cross-calibration factor, β_c , was determined through a cross-calibration using a monodisperse aerosol of ammonium sulfate. For this material, light absorption at 450 nm is negligible, so the scattering coefficient is equal to the extinction coefficient. Truncation errors for GO scattering measurements were estimated for spherical particles at the given volume equivalent diameter, based on the model of Modini et al. [115]. A schematic of the CAPS $PM_{SSA, 450nm}$ is shown in Figure 4-6.

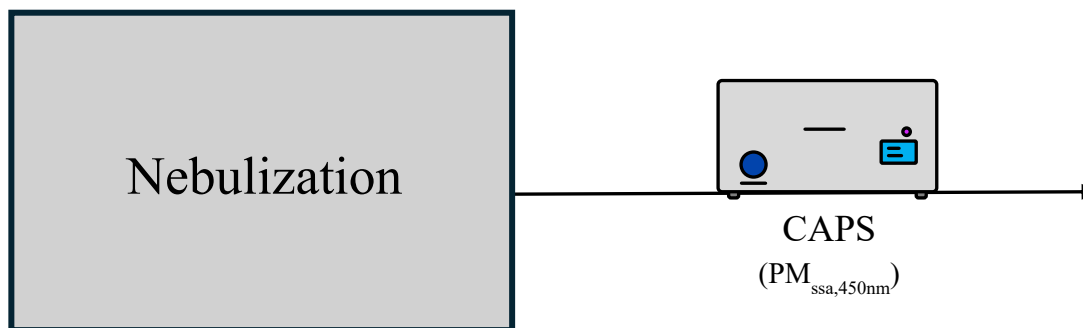


Figure 4-6: Schematic of absolute absorption coefficient at 450nm measurement (CAPS $PM_{SSA, 450nm}$)

The aethalometer (Magee Scientific, Model AE33) works by measuring the transmission of light through a sample of aerosol that is deposited onto a filter tape [116]. A second, unloaded section of the filter tape acts as a reference. The transmission of light is used to estimate $\kappa_{abs,\lambda}$ based on a calibration factor which may vary between samples, changing substantially for aerosols containing a high fraction of light-scattering material [117,118] or unusually large light-absorbing particles [117–119]. Since GO particles may be considered unusually large light-absorbing particles relative to the soot particles which are used to calibrate aethalometers, the aethalometer measurements was re-calibrated using the CAPS $PM_{SSA, 450 nm}$. This calibration factor has a negligible wavelength dependence for highly absorbing samples

[120] and was therefore also applied to the aethalometer measurements at 370 nm, 470 nm, 520 nm, 590 nm, 660 nm, 800 nm and 950 nm. A schematic of the measurement set-up is shown in Figure 4-7.

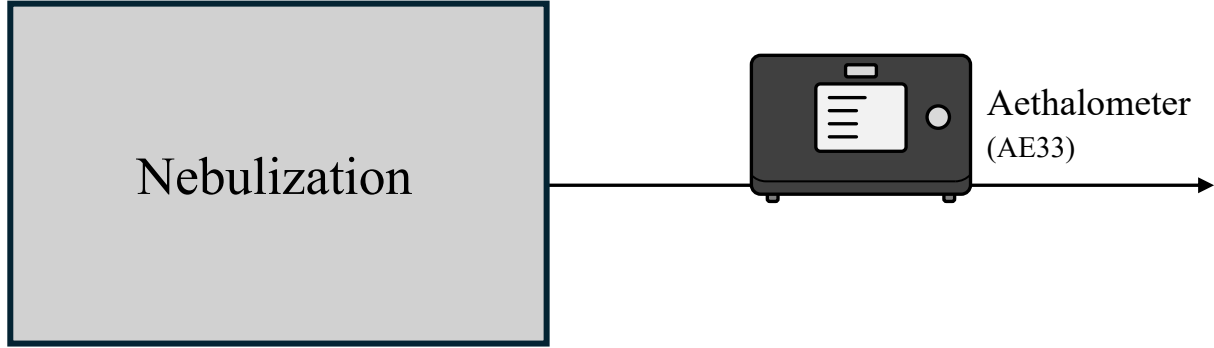


Figure 4-7: Schematic of spectral absorption coefficient measurement (Aethalometer)

The aethalometer data is used to derive the wavelength dependence of light absorption was measured via the AAE, defined as

$$\frac{\kappa_{\text{abs},\lambda_1}}{\kappa_{\text{abs},\lambda_2}} = \left(\frac{\lambda_1}{\lambda_2} \right)^{-AAE} \quad (5.3)$$

or, equivalently,

$$\ln \left(\frac{\kappa_{\text{abs},\lambda_1}}{\kappa_{\text{abs},\lambda_2}} \right) = -AAE \cdot \ln \left(\frac{\lambda_1}{\lambda_2} \right) \quad (5.4)$$

In general, the AAE is sensitive to both particle composition and morphology [121,122]. For particles in the Rayleigh limit (i.e., $x = \pi d_p / \lambda \ll 1$ and $x|m_\lambda| \ll 1$, where x and m_λ are the size parameter and refractive index, respectively), the AAE depends only on composition. Under these conditions, the dipoles within the particle experience a uniform electric field fluctuation, making the absorption dependent on solely the number of dipoles in the particle, which is proportional to the particle volume, and the susceptibility of the dipoles, which is conveyed by Eq. (3.14).

Consequently, for particles within the Rayleigh limit, $\kappa_{\text{abs},\lambda} \propto E(m_\lambda)/\lambda$. Furthermore, if the refractive index is wavelength-independent, the AAE is equal to unity. Therefore, any deviation from an AAE of unity may be attributed to the bulk electromagnetic properties of the material rather than variations in particle size or shape. For instance, black carbon (BC) exhibits an AAE close to unity, indicating the $E(m_\lambda)$ of this material is independent of wavelength over the wavelengths of interest, while the AAE of tar brown carbon (brC) is between 2.5 and 6 depending on the wavelength range [123], implying a dispersive behaviour in m_λ as wavelength changes.

The mass absorption coefficient (MAC) of a particle is determined from dividing the aerosol mass concentration (M) by the absorption coefficient (κ_{abs}), while the mass scattering coefficient (MSC) can be found by dividing M by the scattering coefficient (κ_{sca}). A common method for determining M involves utilizing the CPMA-Electrometer Reference Standard (CERMS) [124]. CERMS is composed of a unipolar diffusion aerosol charger (UDAC, Cambustion Ltd.), a CPMA, and a Faraday Cup Aerosol Electrometer (FCAE, TSI Inc., Model 3068B). A schematic of the CERMS is shown in Figure 4-8:

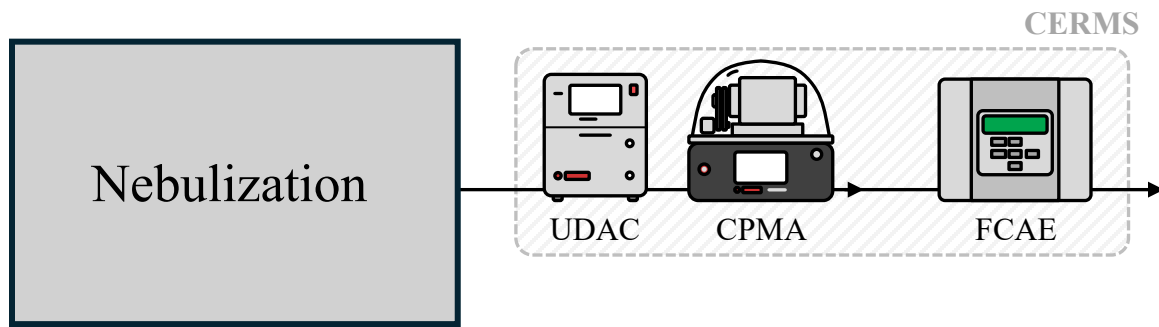


Figure 4-8: Schematic of mass absorption cross-section measurement (CERMS)

The UDAC imparts an electric charge on aerosol particles by generating ions through a high voltage on a fine wire. The ions impart their charge onto the particles, with the charging process controlled by maintaining a constant ion concentration – time product, $ni t$ [125]. The charged particles then pass through the CPMA, which classifies them according to a specific mass-to-charge ratio similar to the

methodology used in the effective density study. The FCAE measures the current resulting from the CPMA selected particles, enabling the determination of the M at a given flow rate using equation [126]:

$$M = M_0 + \frac{m^* I}{v_a e} \quad (5.5)$$

where M_0 is the mass concentration of uncharged particles, m^* is mass-to-charge setpoint, I is the detected current, and v_a is the aerosol flow rate. In this study, M_0 is assumed to be zero due to the high charge rate of a UDAC. The flow rate v_a was calculated to be 1.009 vlp_m. Due to the large number of charges imparted by the UDAC, the previous assumption of $m_p = m^*$ does not hold. Instead, the average single particle mass (\bar{m}) is determined by applying a correction using the interpolated-average charge (INTAC) method. The INTAC method utilizes the n_{it} (5×10^{12} ion·s/m³ in this study) to derive an average charge pre-factor, q_0 , using a power law relationship. The average mass can then be derived from the power law average charge (PLAC) method [127]:

$$\bar{m} = \left(k_c^{-v_c/\zeta} q_0 m^* \right)^{\frac{\zeta}{\zeta - v_c}} \quad (5.6)$$

Where k_c is the mass mobility pre-factor and $v_c \sim 1$ is the exponent describing the increase in average charge with particle mass. The MAC and MSC at 450 nm can be calculated using the M determined via CERMS, along with the $\kappa_{\text{abs}, 450\text{nm}}$ and $\kappa_{\text{sca}, 450\text{nm}}$ measured by the CAPS PM_{SSA, 450nm}. The MAC and MSC are derived by dividing $\kappa_{\text{abs}, 450\text{nm}}$ and $\kappa_{\text{sca}, 450\text{nm}}$ by M , respectively.

A final analysis using a commercial LII device (LII 300) was performed on the aerosolized GO powder to assess whether LII would be applicable for GO. The LII 300 is a two-colour LII device that operates similarly to the four-colour device described in Section 3.2. A Nd:YAG laser at 1064 nm and 20 Hz is used to irradiate incoming GO particles, with an internal optical set-up to focus and magnify both the laser and the subsequent incandescent signal. The laser passes through an initial aperture sized at 1.75 mm × 1.75 mm, then through three 90° mirrors to direct the beam into an aperture wheel, ensuring that

only the image is transmitted. The laser is then attenuated using a filter wheel containing various neutral density (ND) filters. Before the signal reaches the photomultiplier tubes (PMTs), a 510 nm dichroic mirror (Semrock FF5-Di01-25 mm × 36 mm) splits the signal into two optical paths that are filtered using bandpass (BP) filters centered at 446 nm (Semrock FF01-442/46-25) and 720 nm (Semrock FF01-716/40-25), respectively. A schematic of the internal system of the LII 300 is shown in Figure 4-9.

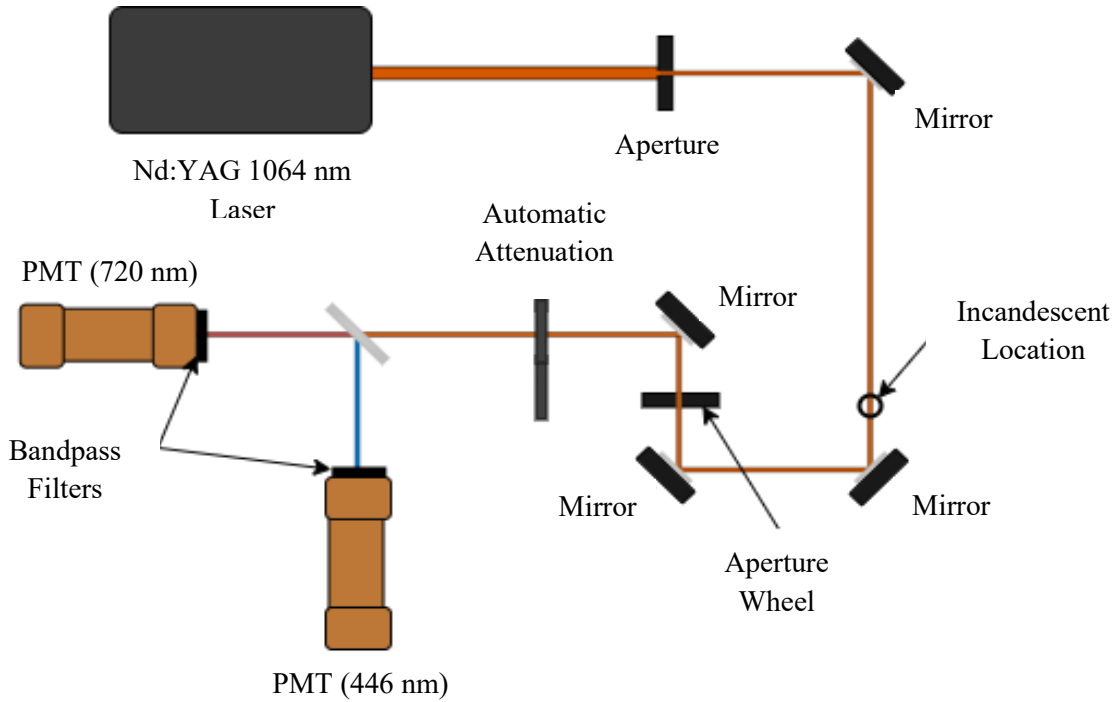


Figure 4-9: Schematic of LII 300 internal workings

The absolute intensity signals were measured and processed externally. Since only two wavelength signals were recorded, the pyrometric temperature was derived using Eq. (3.20). The schematic for LII-300 experimental procedure is shown in Figure 4-10. An SMPS was operated in conjunction with the LII-300 to monitor particle size during this experiment.

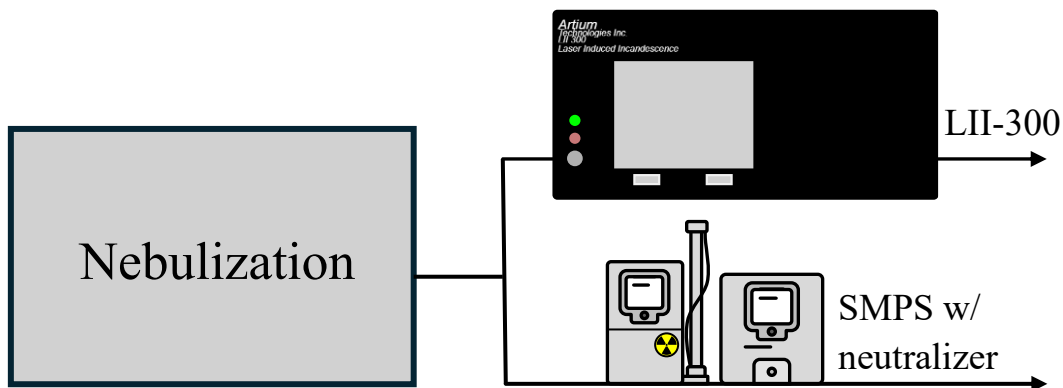


Figure 4-10: Schematic of LII-300 experimental procedure

4.3 Summary

This chapter outlines the experimental apparatus and methodologies used to determine the morphological and optical properties of GO. The process began with the preparation of a stable colloid suspension of GO powder, which was then nebulized into an aerosol. The apparatuses used were described, with emphasis placed upon how they provide information regarding the desired morphological and optical properties. The effective density and mass-mobility coefficient were derived using a combination of the SMPS and the CPMA. Unscaled spectral absorption coefficients were found using the aethalometer and then calibrated with the absolute absorption coefficient at 450 nm provided by the CAPS $PM_{SSA, 450nm}$. A combination of the CERMS and CAPS $PM_{SSA, 450nm}$ gave the mass concentration and absorption/scattering coefficients at 450 nm, which were necessary to calculate the mass absorption cross-section and mass scattering cross-sections. A final study was conducted with a commercial LII system and the four colour LII system presented in Section 3.2 to test whether LII analysis is suitable for GO powder. The outcome of these procedures are reviewed in Chapter 5.

Chapter 5

GO ex-situ results and analysis

The results obtained from the experiments conducted using the apparatuses detailed in Chapter 4 are discussed here. The morphology and optical characteristics were analyzed and compared in a wide range of sizes to establish a foundation for online diagnostics. This study aimed to connect the optical and morphological properties to determine their potential for monitoring and controlling the quality of GO and rGO during synthesis. The results are compared with existing literature, with explanations provided for observed discrepancies. Additionally, references to rGO are made based on literature data to extrapolate its properties due to the limited availability of rGO material.¹

5.1 Particle morphology

5.1.1 TEM results

Transmission electron micrographs are made on GO colloid drop casted onto the holey carbon grid. The images are shown in Figure 5-1. Figure 5-1 (b) shows a magnified subregion of Figure 5-1 (a), while Figure 5-1 (c) shows diffraction patterns arising from electron interaction with the crystalline structure of the GO. In general, the GO exists as large, multiple micrometer diameter, crumpled particles with smaller independent particles, like the one in in Figure 5-1 (b). The SAED diffraction pattern in Figure 5-1 (c) is similar to other GO samples shown in the literature [128]. Clear diffraction spots are seen with a six-fold pattern that is consistent with the hexagonal lattice in sp² carbon. This indicates that the graphitic stacking order is preserved in this sample. Electron energy loss spectroscopy (EELS) analysis conducted on the particles suggest a carbon content of $39.8 \pm 1.4 \%$ and an oxygen content of $60 \pm 2 \%$ with the remainder attributed to hydrogen. A higher-than-normal oxygen content is observed when compared to

¹ This study has been submitted to the Journal of Aerosol Science in the manuscript “Investigation of morphology and optical properties of graphene oxide for online diagnostics”, co-authored by Halil Ibrahim Yazici, Dr. Joel Corbin, Dr. Rym Mehri, Dr. Timothy Sipkens, and Dr. Kyle Daun

literature data [129]. This is likely a result of the water present in the colloid and drop casted sample. Nevertheless, the high oxygen content shows a well oxidized GO sample.

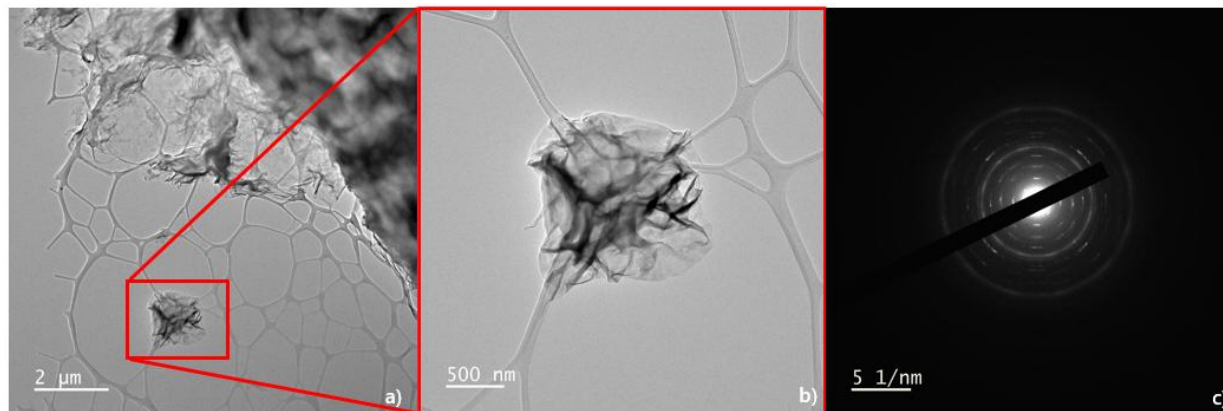


Figure 5-1: TEM image of (a) multiple GO particles, (b) higher magnification of a single GO particle, (c) diffraction pattern from the GO particle

5.1.2 Mobility diameter distribution

An initial test was run using the SMPS as shown in Figure 4-4 to determine the mobility diameter distribution of the aerosolized GO particles. Each study involved eight consecutive runs, with each run recording the particle concentration as the DMA voltage was varied from low to high. Figure 5-2 shows the averaged mobility size distributions for samples containing only deionized (DI) water and those containing the aerosolized GO colloid. In the mobility size distributions of the study containing the aerosolized GO colloid, a bimodal distribution is seen with a smaller mode around 20 nm. This mode was also present in the water-only measurements; consequently, this 20 nm mode can be attributed to residual particles formed from impurities present in the $\sim 1 \mu\text{m}$ water droplets produced by the Collison nebulizer [130]. The volume ratio of water droplets to residual particles is 8×10^{-6} , implying an impurity concentration of 8 ppm. The larger mode corresponds to the aerosolized GO particles, corresponding to a count mean diameter (CMD) of 110 nm and a geometric standard deviation (GSD) of 2.0. These parameters agree well with a similar study conducted by Ma et al. [68] who found a distribution ranging

from 100 to 400 nm with peak concentrations at 150 nm. The similarity in sizes is expected, based on the findings of Marcano et al. [23], as the main difference between the GO produced in this study versus Ma et al. [68] is the synthesis method (improved Hummer’s method and modified Hummer’s method, respectively), which does not lead to significant changes in particle size.

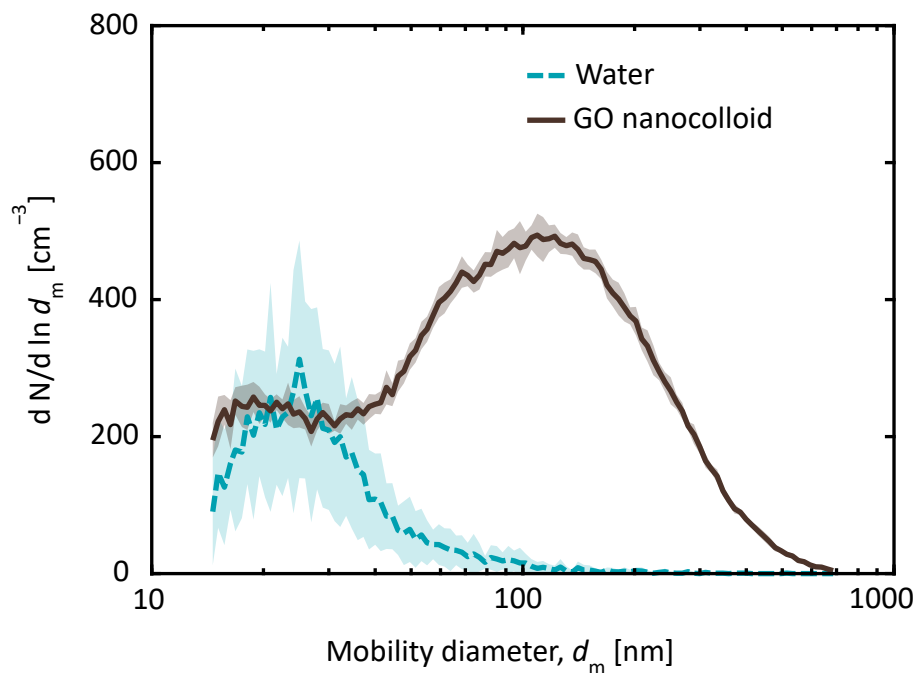


Figure 5-2: Mobility diameter vs number concentration for aqueous aerosolized GO colloid in water

5.1.3 Effective density and mass mobility exponent

The next study looked at determining the effective density as a function of mobility diameter and the mass mobility exponent. This analysis provides insight into the degree of crumpling of the particle and the variability of particle morphology across different sizes. The system outlined in Figure 4-5 was utilized, which combined the SMPS and CPMA. Figure 5-3 shows the effective density over multiple mobility diameters. The vertical error bars represent a conservative estimate of the possible uncertainty in the effective density as only three replicates were possible; the full derivation is present in the supplementary information in Appendix B.2. The effective density found across all mobility diameters has

a mean value of $0.93 \pm 0.06 \text{ g/cm}^3$, with no clear size dependence, as represented by the black dotted line in Figure 5-3. This indicates that the aerosolized GO particles are highly compact, which is further demonstrated with the measured mass-mobility exponent of 2.97 ± 0.06 . This is also consistent with the TEM images in Figure 5-1.

The aerosolized GO particles measured by Ma et al. have an effective density of 0.95 g/cm^3 at 150 nm [15] and a mass-mobility exponent of 2.54 ± 0.04 [68], as shown by the red dotted line in Figure 5-3. While the effective density is comparable to values obtained in the present work, the mass-mobility exponents differ significantly. This discrepancy may originate from different crumpling mechanisms associated with the particle formation process: the modified Hummer's method used by Ma et al. [15] employs acidic solvents, concentrating, and oxidizing agents [131] compared to the improved Hummer's method used in this study. Marcano et al. [23] has shown that the final GO produced by the improved Hummer's method contain a higher oxygen content than that produced using the modified Hummer's method. This may contribute to the increased fractal dimension as it has been shown that higher oxygen content and degree of defects can lead to more compact crumpling [132,133]. Additionally, this study incorporated an extra spray drying step to produce GO powder. Spray drying is known to cause additional crumpling [89], as suggested by the images in Figure 5-1. The combination of spray drying and increased oxygen content could explain the difference in the fractal dimension. However, further investigations are needed to understand the exact mechanisms that led to the increased compactness and assess the repeatability of the process.

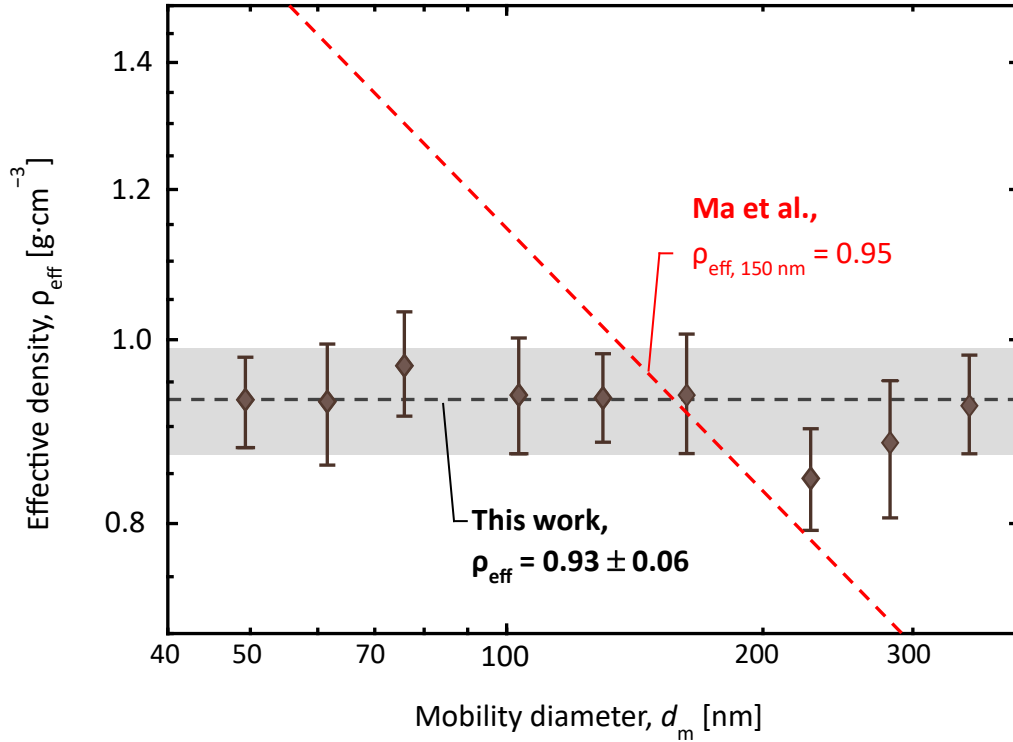


Figure 5-3: Effective density vs mobility diameter of aqueous aerosolized GO: One-dimensional plot with the average effective density

In addition, a bidimensional effective density distribution was derived from the data. This analysis method was first introduced by Rawat et al. [134] and provides both the average effective density and the spread about the mobility diameter. The experimental data is inverted using the kernel with contributions from the DMA [135], CPMA [136], and charger [137]. Inversion is performed using a direct, second-order Tikhonov regularization scheme, with further details provided by Sipkens et al. [109].

The bidimensional effective density-mobility distribution is shown in Figure 5-4, where the colors indicate number concentration present across both mobility diameter and effective density. The solid, brown ellipse represents three standard deviations of the mean of the bivariate lognormal distribution fit, as well as the effective density-mobility relationship. In contrast, the dashed, black ellipse corresponds to soot, as reported by Trivanovic et al. [108]. For GO, the maximum of the bidimensional distribution occurred at $d_m = 110$ nm, aligning with the SMPS results. Compared to soot, GO is more

compact, with lower standard deviations (solid ellipse) when compared to previously recorded soot data (dotted ellipse). This can be quantified by comparing the conditional GSD (i.e., the GSD of vertical “slices” through the distribution), where GO has a standard deviation of 1.20 while soot has a standard deviation of 1.29. This difference stems from the larger number of possible monomer configurations in soot aggregates compared to crumpled GO. Even so, this GSD is sufficiently far from unity, indicating some variability in the morphology of crumpled GO.

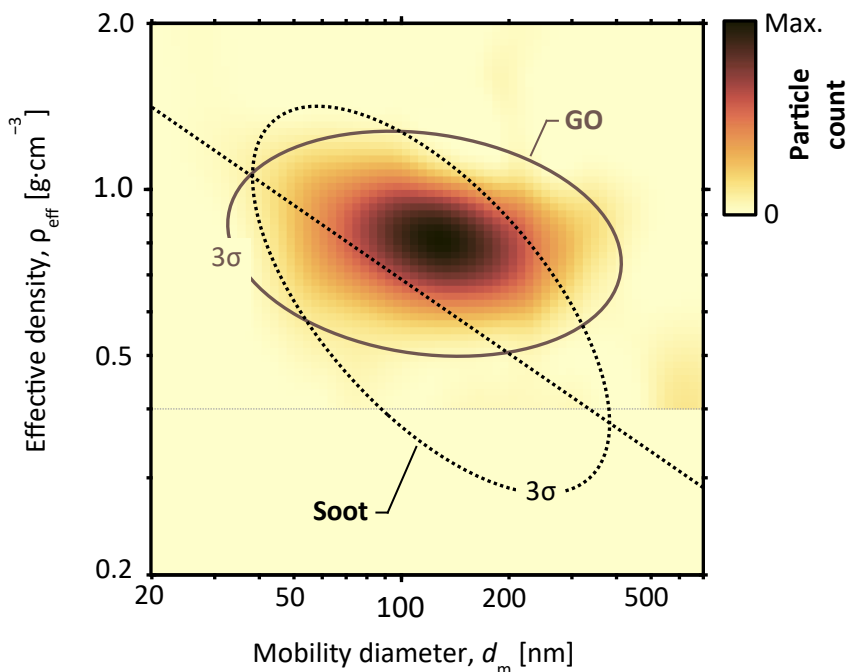


Figure 5-4: Effective density vs mobility diameter of aqueous aerosolized GO: Two-dimensional distribution with ellipses representing standard deviation from the mean bivariate fit (yellow: this study, white: M9 soot data from Trivanovic et al. [108])

5.2 Particle optical characteristics results and discussion

5.2.1 Spectral absorption coefficient and absorption Ångström exponent

Figure 5-5 shows the absorption coefficient as a function of wavelength, obtained by normalizing the relative κ_{abs} given by the aethalometer with the absolute absorption coefficient at 450nm ($\kappa_{\text{abs},450\text{nm}}$) obtained from the CAPS $\text{PM}_{\text{SSA},450\text{nm}}$. The vertical error bars indicate one standard deviation of the

relative κ_{abs} as derived from measurement uncertainty of the aethalometer obtained over fifteen minutes. The AAE_{GO} was determined to be constant with a value 2.48 ± 0.04 , which is similar in magnitude to that of some types of atmospheric brown carbon ($2 < \text{AAE} < 6$) [138]. This AAE is consistent with the brown coloration of the GO powder, indicative of a larger HOMO-LUMO band-gap energy compared to soot ($\text{AAE} \approx 1.0$) [138], rGO ($1.0 < \text{AAE} < 1.3$) [45], or few-layer graphene ($\text{AAE} \approx 0.5$) [139], likely due to the disruption of the conjugated bonding in graphene by oxygen-containing functional groups.

The spectral absorbance data from Li et al [140] elucidates the differences in the AAE between rGO and GO. Both rGO and GO exhibit absorption peaks around 250 nm; however, the rGO shows significant absorption at wavelengths longer than 1 μm while GO exhibit low absorption at wavelengths longer than 500 nm. Consequently, GO primarily absorbs light near its resonant frequencies in the UV range. Due to the lower absorptivity of GO at longer wavelengths compared to rGO, its AAE is higher.

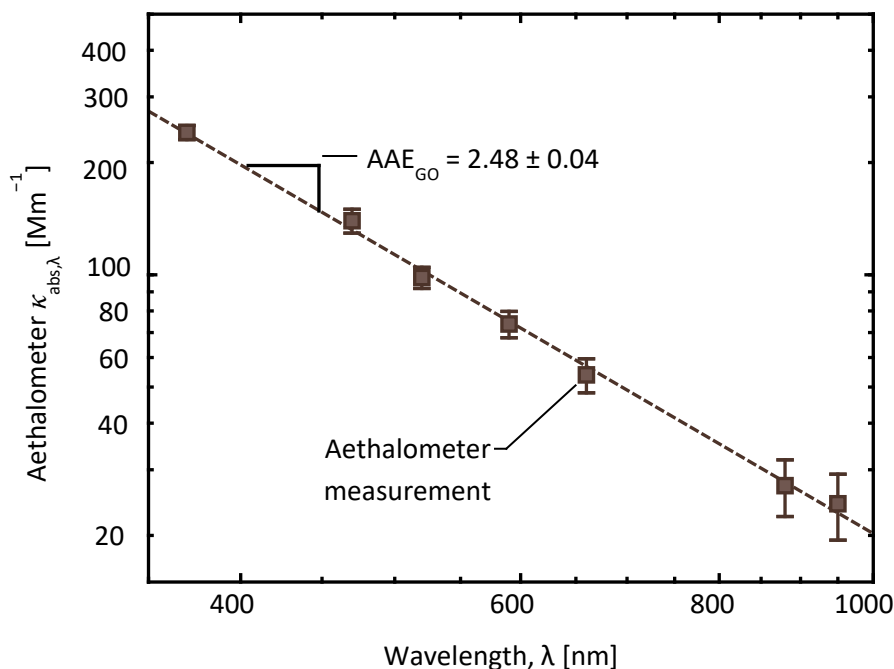


Figure 5-5: Normalized wavelength-resolved absorption coefficient vs wavelength of nebulized GO

5.2.2 Mass absorption cross-section and Mass scattering cross-section

The mass absorption cross-section (MAC) and mass scattering cross-section (MSC) at 450 nm were studied across various particle masses to assess whether the optical properties of the particle change significantly with size. The investigation combined the CERMS and CAPS PM_{SSA, 450nm} as depicted in Figure 4-8. To interpret the observed trends, a theoretical fit based on the absorption efficiencies computed with Mie theory, Eqs. (3.8) - (3.11), and the Rayleigh approximation, Eqs. (3.12) and (3.13), were applied. Using the $Q_{\text{abs}, 450\text{nm}}^{\text{Ray}}$ and $Q_{\text{sca}, 450\text{nm}}^{\text{Ray}}$ the MAC and MSC can be described using

$$\text{MAC}_{\text{Ray}} = \frac{6\pi E(m)}{\lambda \rho_m} \quad (6.1)$$

and

$$\text{MSC}_{\text{Ray}} = \frac{24\pi^5 d_{\text{ve}}^6 F(m_\lambda)}{\rho_m \lambda^4} \quad (6.2)$$

The Mie fit was performed using the derived effective density, ρ_{eff} , for the material density, ρ_m , and the derived mobility diameter, d_m , in place of the volume equivalent diameter, d_{ve} . A refractive index, m_λ , that led to the best fit with the experimental data, was found during this process. In contrast, for the Rayleigh limit model, the ρ_m (1.36 g/cm³) [110] and m_λ (1.70 + 0.055i) [141] used were taken from literature results. The different parameters used may cause discrepancies between the Mie fit and Rayleigh model, with the Mie fit not converging to the Rayleigh model at lower wavelengths as expected. Nonetheless, both results will give an understanding of the trends expected and help elucidate the observed results.

Figure 5-6 and Figure 5-7 shows measured and theoretical MAC and MSC at 450 nm vs. average single particle mass. The $m_{\lambda, \text{Mie}}$ derived from the Mie fitting is 1.43 + 0.027i, in contrast to the $m_{\lambda, \text{Ray}}$. Vertical error bars indicate one standard deviation of the MAC and MSC as derived from measurement

uncertainty of the CAPS PM_{SSA} system obtained over one minute. It is expected that the variation in the signal over time is the dominant source of error as a calibration was done with ammonium sulfate.

Figure 5-6 shows that the MAC is nearly constant at $0.93 \pm 0.20 \text{ m}^2/\text{g}$ for particles having a mass less than or equal to 15 fg. This value aligns with MACs reported in the literature for GO particles of 150 nm that are reduced by a temperature less than 200°C (i.e., constant region $\sim 0.90 \text{ m}^2/\text{g}$) [15]. For particles larger than 15 fg, the MAC increases to $1.08 \pm 0.20 \text{ m}^2/\text{g}$. This change can be attributed to the fact that the larger GO particles no longer fall within the Rayleigh limit [76]. Consequently, the dipoles in the particle experience the incident EM wave at a different phase shift, and couple with each other. This is confirmed by the good degree-of-fit between the experimental MAC and the one calculated from Mie theory. The variations in the fit can be attributed to potential deviation of the fitted $E(m_\lambda)$ from that of the GO particles and the assumption that $\rho_{\text{eff}} = \rho_m$. The material density of GO used in this study is based on the weighting of a regular geometric foil [110]. A separate measurement in a different study used the Archimedes method in water and reported a value of $1.80 \text{ g}/\text{cm}^3$ [111]. Meanwhile, the effective density found in this study was $0.93 \pm 0.06 \text{ g}/\text{cm}^3$. The low effective density compared to the material densities reported in the literature, coupled with the given mass-mobility exponent of three, suggests the presence of voids in the GO particles. Additionally, at high single particle masses (i.e., above 31 fg), the signal to noise ratio decreased significantly due to the lack of appreciable signal, potentially contributing to the discrepancies between the results. However, the good degree-of-fit from Mie theory and the measured data signifies that the GO particles are compact, which supports the inferred mass-mobility exponent of nearly three (2.97 ± 0.06). The MAC for the GO particles is significantly smaller compared to typical values of other carbonaceous particles such as soot ($7.3 \text{ m}^2/\text{g}$), graphene ($8.7 \text{ m}^2/\text{g}$), rGO ($9.1 \text{ m}^2/\text{g}$) [142], and FLG ($12.6 \text{ m}^2/\text{g}$) [139], indicating GO particles have inferior absorption characteristics. This is expected due to the absence of conduction band electrons in GO.

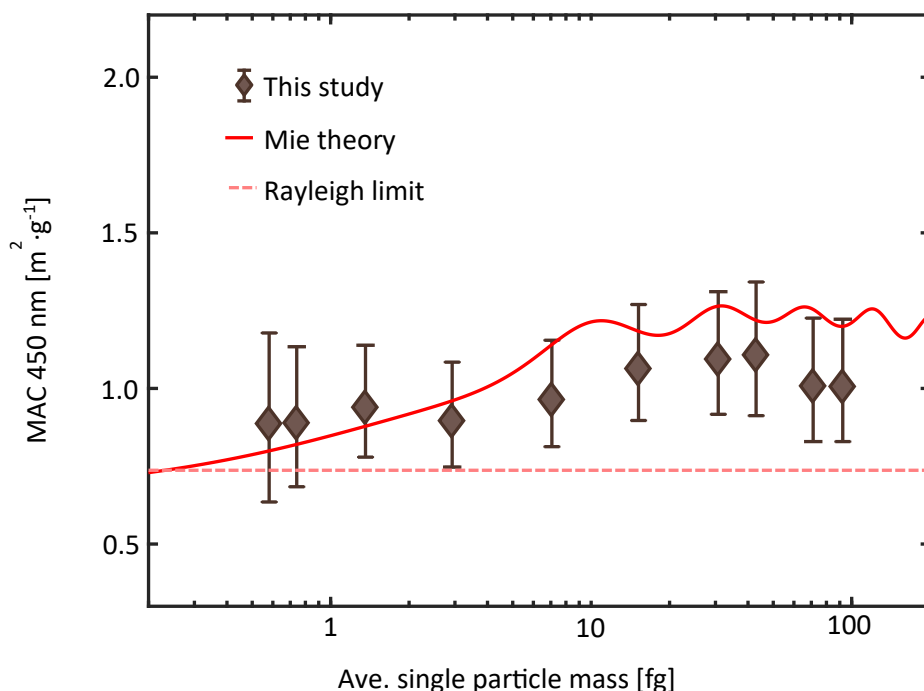


Figure 5-6: MAC at 450nm vs average single particle mass + fitted data using Mie Theory and Rayleigh theory

Figure 5-7 shows that the MSC of GO varies notably with single particle mass, exhibiting a change in the relationship around 15 fg. As is the case for the MAC, this single particle mass corresponds to the scattering regime transitioning outside the Rayleigh limit as the particle size increases. As the particle size exceeds the Rayleigh limit, the scattering cross-section dependence on particle diameter transitions from a power-of-six dependence (Eq. (6.2)) to a power-of-two (the geometric limit) [76,77]. This corresponds to the observed change in the MSC trend with respect to particle mass as shown in Figure 5-7, as an increasing trend would be expected within the Rayleigh limit versus a decreasing trend after the transition to the geometric limit. The MSC predicted by Mie theory shows a similar trend, and as was the case with the MAC, deviations between the experimentally measured MSC and the Mie theory prediction may be attributed to deviation in the fitted m_λ and the lower signal to noise ratio at higher single particle masses. Notably, the MSC consistently exceeds the MAC across all single particle masses,

signifying that scattering-based diagnostics like elastic light scattering (ELS) would be better suited to characterizing GO particles, as opposed to an absorption-based technique like TiRe-LII.

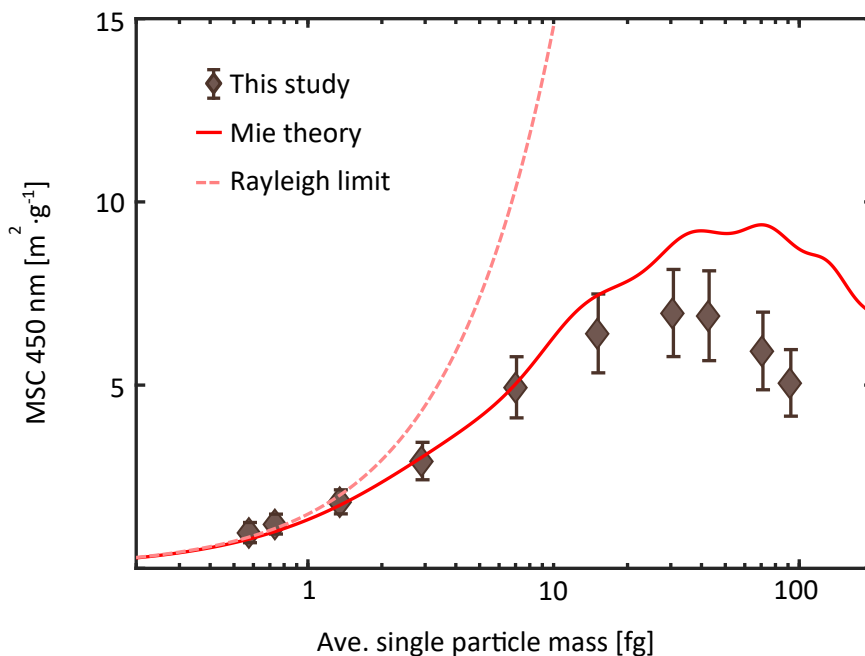


Figure 5-7: MSC at 450nm vs average single particle mass + fitted data using Mie Theory and Rayleigh theory

5.2.3 TiRe-LII validation and verification

Given the low absorption characteristics determined from the MAC study, TiRe-LII is not expected to be a viable optical diagnostic tool for GO. On the contrary, however, LII holds promise for rGO. To evaluate the efficacy of LII for GO and rGO, a preliminary study was run using both the LII 300 at the NRC, as shown in Figure 4-10, and the four-colour LII apparatus at the University of Waterloo, as shown in Figure 3-6. For the LII 300 system, 290 measurements were taken, each capturing signal recordings over 400 ns with a laser fluence of 3.85 mJ/mm². The measurements were averaged to provide two sets of data at wavelengths 446 nm and 720 nm. Analysis revealed that after 160 ns the signals diminished to background levels, indicating no appreciable incandescence. Consequently, the initial 160 ns were analyzed using two colour optical pyrometry, Eq. (3.20), assuming a constant $E(m_\lambda)$. Figure 5-8 presents

the pyrometric temperature and incandescent signal intensity over time. Note the lack of noise present in the data results from internal smoothing of the LII300 system.

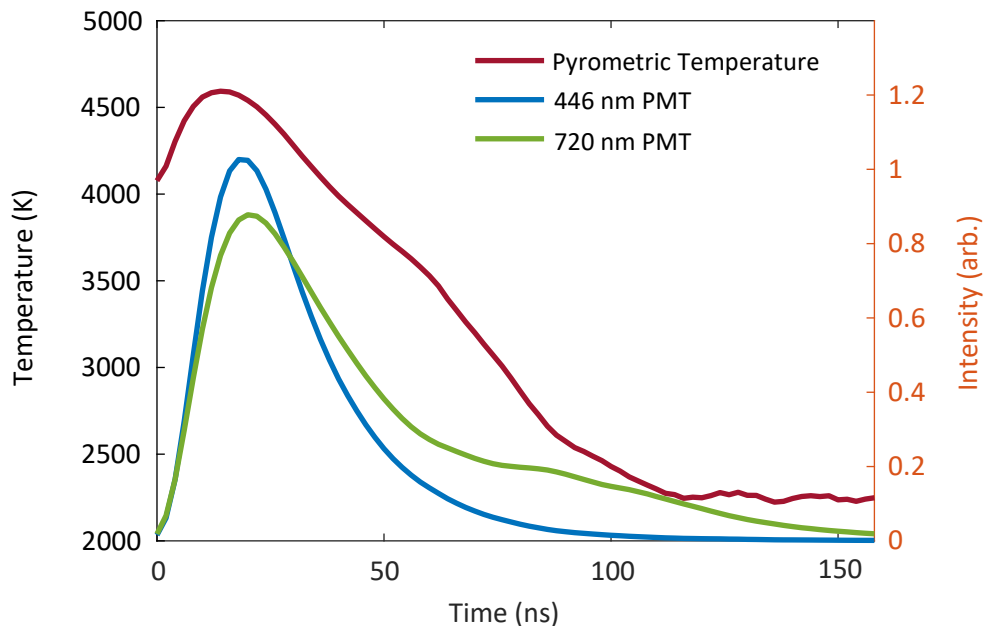


Figure 5-8: Temporal evolution of pyrometric temperature and signal intensity of GO

The duration of incandescence primarily depends on particle size. Particle sizes were determined using the SMPS operated in line with the LII-300 as shown in Figure 4-10. The size distribution of the particle is shown in Figure 5-9, where the GMD is 100.77 nm.

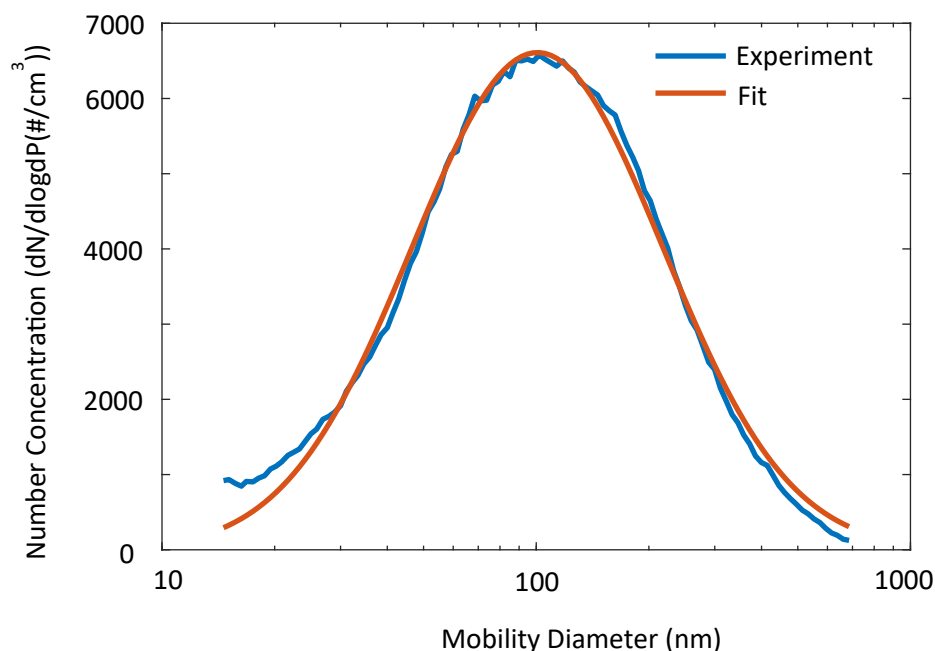


Figure 5-9: Mobility diameter distribution during LII-300 experiment

The particles sizes observed in this study are comparable to those examined Musikhin et al. [58], who investigated the potential efficacy of LII on few-layer graphene (FLG) using the LII-300. Figure 5-10 presents the temporal evolution of normalized temperature for FLG, soot, GO, and rGO from this study. The plot clearly shows that FLG and soot, which are confirmed to be incandescent signals, exhibit much longer decay times compared to GO. However, due to their comparable size, a similar decay time is expected. Consequently, the short signal is hypothesized to result from non-thermal emission originating from the laser pulse (~ 10 ns) [55], which are broadened by internal signal manipulation in the LII-300.

To further investigate the incandescence properties of GO and rGO, the four colour LII set-up at the University of Waterloo was used. This set-up, as shown in Figure 3-6, employs a Collison nebulizer (Model 3076, TSI Inc.) to aerosolize GO and rGO colloids. For GO, a 0.5 wt% colloidal solution was synthesized with water as the solvent, consistent with the LII 300 experiments. The aerosolized GO passed through a diffusion drier before entering the LII measurement chamber. Experiments were

conducted for fluences between $0.7 - 2.75 \text{ mJ/mm}^2$. Similar to the LII-300 system, no appreciable LII signal was detected with GO at any fluence, reinforcing the hypothesis that the signals from the LII-300 originated from non-thermal emissions rather than incandescence.

Conversely, rGO produced clear incandescent signals under the same experimental conditions. The rGO powder used, synthesized via a plasma reduction method as described in Section 3.3, was dispersed in ethanol due to rGO precipitating slower in ethanol compared to water [139]. A 0.5 wt% rGO colloidal solution was prepared and nebulized. Similar to GO, experiments were conducted for fluences between $0.7 - 2.75 \text{ mJ/mm}^2$. A four-colour optical pyrometric procedure was applied to the incandescent signals following the process outlined in Section 2.1.1. Data from the experiment performed at 1.43 mJ/mm^2 is shown in Figure 5-10. While the GO signal from the LII300 plateaus at approximately 75 ns, the rGO continues to cool to 1 μs , similar to the signals reported by Musikhin et al. [58]. Evidently, appreciable LII signals are detected with rGO, indicating the potential in using LII to characterize rGO. To further assess this, the next section will focus on integrating the four-colour TiRe-LII system with the tube furnace thermal reduction system described in Section 3.1 to derive the specific surface area in real time.

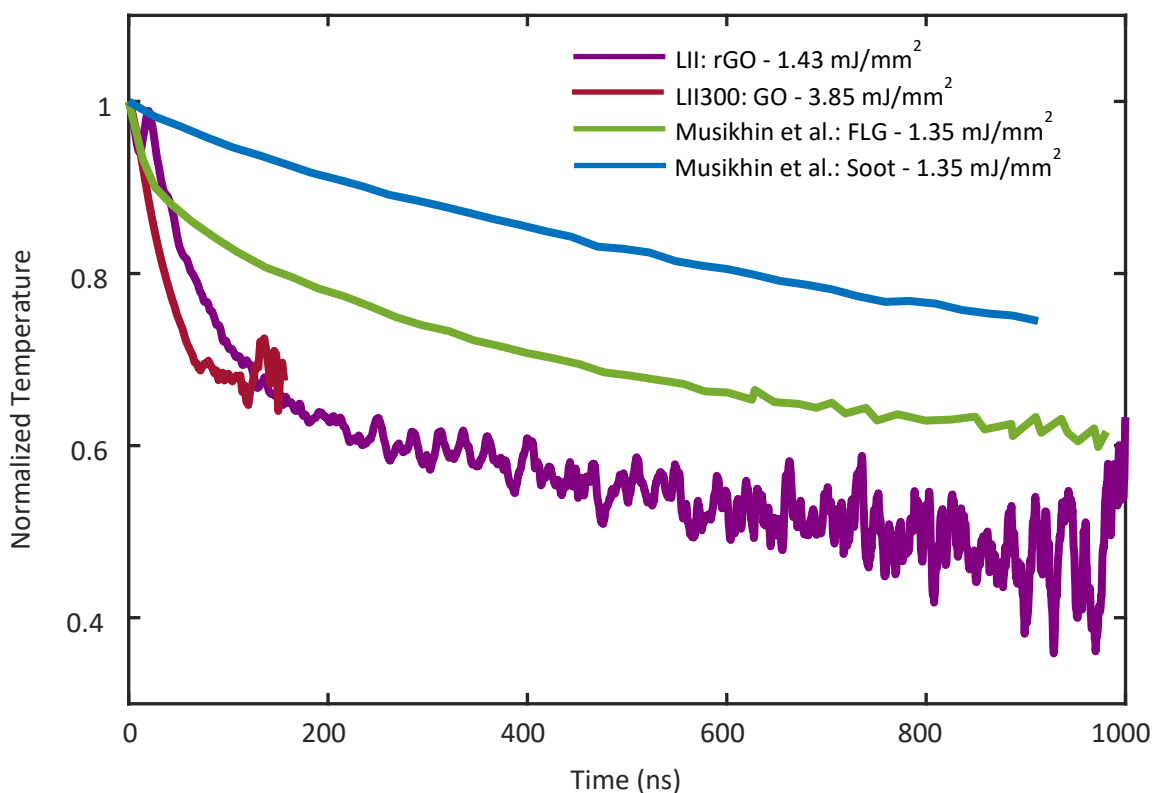


Figure 5-10: Temporal evolution of normalized temperature for GO, rGO, FLG, and Soot [58]

5.3 Summary

This chapter presents the *ex situ* morphological and optical characterization of graphene oxide (GO) conducted at the National Research Council (NRC) of Canada. This study connects the morphological and optical characteristics of GO over a wide range of sizes, establishing the foundation for online optical diagnostics. Morphological parameters analyzed include mobility diameter, effective density, and mass mobility exponent, while optical parameters analyzed include wavelength resolved absorption coefficient, absorption Ångström exponent, mass absorption cross-section (MAC) and mass scattering cross-section (MSC).

The average mobility diameter of the GO was approximately 110 nm with a fractal dimension of 2.97 and a constant effective diameter of 0.93 g/cm³. The derived bidimensional distribution indicates that

GO particles have a more compact size distribution compared to soot. Optical measurements reveal that the GO particles are inefficient light absorbers, exhibiting a high AAE of 2.46, similar to brown carbon, and a MAC ranging from 0.75 – 1.25 m²/g across all particle masses. Conversely, the MSC is significantly higher, ranging from 1.75 – 7.5 m²/g, suggesting the potential of scattering-based characterization techniques, such as elastic light scattering, for online measurements of GO. The ineffectiveness of TiRe-LII in characterizing GO is substantiated by experiments using both the commercial LII-300 and four-colour LII set-up. Neither system detected appreciable incandescent signals from GO. On the other hand, when rGO was analyzed using the four-colour set-up, clear incandescent signals were shown, demonstrating the efficacy of LII in characterizing rGO.

The subsequent chapter will explore the potential of LII for online characterization of rGO by integrating the tube furnace reduction into the four-colour LII system.

Chapter 6

Online TiRe-LII characterization of thermal reduction of rGO

This chapter details a study to verify the suitability of TiRe-LII to provide functional information via online measurement of reduced graphene oxide (rGO) generated using a tube furnace. The primary functional parameter analyzed in this study is the specific surface area (SSA). The analysis method follows the procedure detailed in Section 2.1.3, which involves deriving the SSA from the LII signal decays. Additionally, the synthesized rGO was collected and Brunauer-Emmett-Teller (BET) specific surface area testing was carried out to determine the BET specific surface area of the synthesized rGO particle. Comparison was made between the SSA values derived from LII and BET measurements, and general comments were provided on the applicability of the diagnostic method. References to SSA values of rGO and other carbonaceous particles in the literature were made to contextualize the synthesis results.

6.1 Experimental set-up

Two experimental set-ups were used in this study: a combined system consisting of the tube furnace system detailed in Section 3.1.2 and the four colour TiRe-LII system described in Section 3.2, as well as a commercial Brunauer-Emmett-Teller (BET) specific surface area (SSA) tester. The combined system facilitates real-time SSA measurement by analyzing the incandescent signals emitted from rGO particles upon laser heating. Conversely, the BET-SSA tester provides SSA measurements of the synthesized rGO from a well-established and validated gas adsorption process.

6.1.1 Tube furnace and LII system integration

This section focuses on the integration of the tube furnace and the LII systems, described in Sections 3.1.2 and 3.2, respectively. The LII system was connected downstream of the tube furnace to measure the rGO. It was installed before the collection filter by directing the aerosol flow into the probe volume. Figure 6-1 and Figure 6-2 illustrate the aerosol flow schematic and physical experimental set-up, respectively. This

configuration minimized disturbances to the produced rGO and simplified the set-up by eliminating the need for optical path configurations.

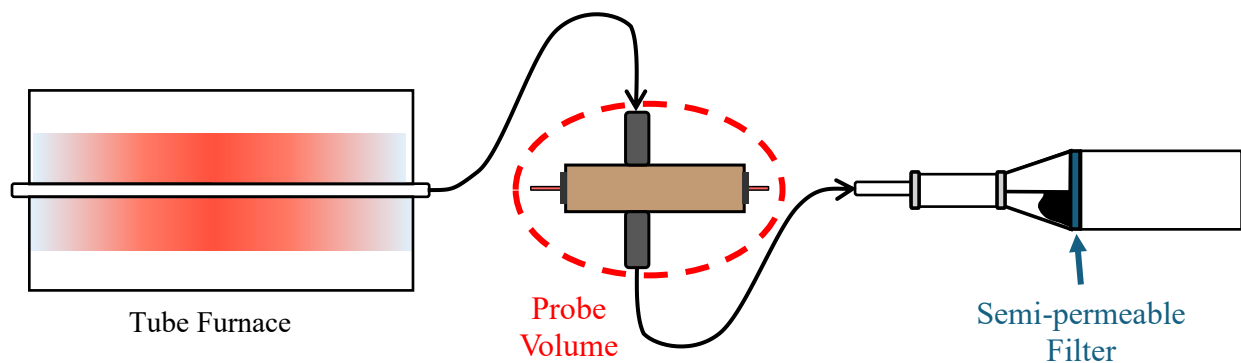


Figure 6-1: Schematic of tube furnace & TiRe-LII set-up. Note, the probe volume is connected to the rest of the system described in Figure 3-6.

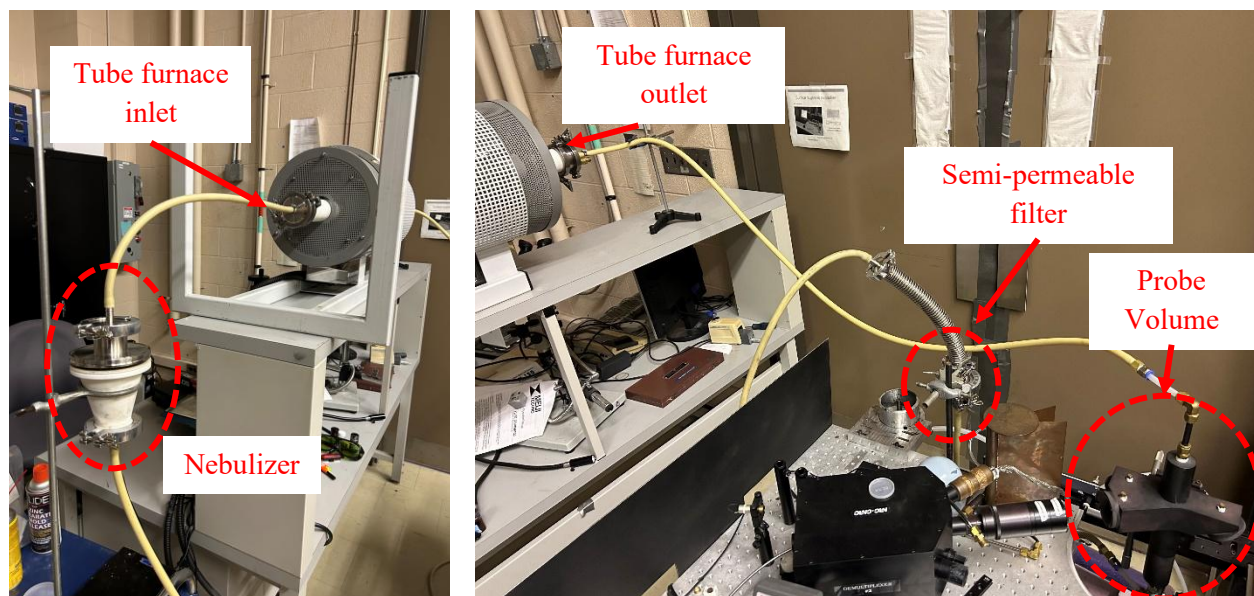


Figure 6-2: Physical image of tube furnace & TiRe-LII set-up

The GO powder was placed on the collection filter within the nebulizer, as shown in Figure 3-3. Nebulization was performed using argon as the carrier gas, released at a gage pressure of 41.37 kPa resulting in a flow rate of 8.50 slpm. A 12V fan was used to help circulate the GO powder within the nebulizer, assisting the argon gas in entraining and carrying the GO powder through the system. The tube

furnace was preheated to a set temperature and maintained for at least 30 minutes before initiating any experiments. Subsequently, the aerosol was directed into the probe volume, where the laser interacted with the particles, creating incandescent signals. These signals were collected using the detection system described in Section 3.2.2. The aerosol is directed to an exhaust equipped with a semi-permeable filter, allowing for powder collection.

6.1.2 Experimental procedures

To assess the capability of TiRe-LII in determining the SSA of rGO, a study was conducted focusing on relative SSA values derived from Eq. (3.30). This approach was taken due to the lack of precise information on key parameters of the studied rGO. The properties of rGO can vary significantly depending on the synthesis process due to the different concentration of oxygen functional groups and defects [37,143–145]. In this study, the specific heat capacity, c_p , and thermal accommodation coefficient, α_T , are unknown, preventing the calculation of absolute SSA values. Instead, a relative study was conducted to compare derived SSA values at various reduction temperatures.

It is established that higher processing temperatures typically lead to greater removal of oxygen-containing groups, resulting in a higher degree of reduction [36,37]. Therefore, the SSA is anticipated to increase as a function of tube furnace set-point temperature due to the restoration of the graphitic structure. To investigate this hypothesis, the tube furnace is set to five different temperatures: 500°C, 700°C, 900°C, 1100°C, 1300°C. For all five temperatures, the laser fluence will be consistent at 0.83 mJ/mm². The voltage gain of the photomultiplier tubes are set according to Table 1. A low fluence is chosen to avoid evaporation or vaporization during the experiments. Additionally, the gas temperature was determined to be 20°C (293.15 K) using a thermocouple placed directly before to the probe volume.

Table 1: Gain values for each PMT

PMT Wavelength	447 nm	550 nm	650 nm	747 nm
-----------------------	--------	--------	--------	--------

Voltage gain	650	600	650	600
--------------	-----	-----	-----	-----

The applicability of the free molecular regime assumption, Eq. (2.32), is assessed by calculating the Knudsen number. Transmission electron microscopy (TEM) images of the rGO were obtained to analyze their characteristic length. The rGO was collected from the semi-permeable filter and dispersed into an ethanol solution. The solution was drop-cast onto a holey carbon grid which was subject to TEM imaging. The images in Figure 6-3 reveal particles of varying sizes. In Figure 6-3 (a), a particle with a characteristic length of approximately 1.5 μm is seen; Figure 6-3 (b) depicts a smaller particle with a characteristic length of 1 μm , with Figure 6-3 (c) showing a smaller particle around 600 nm.

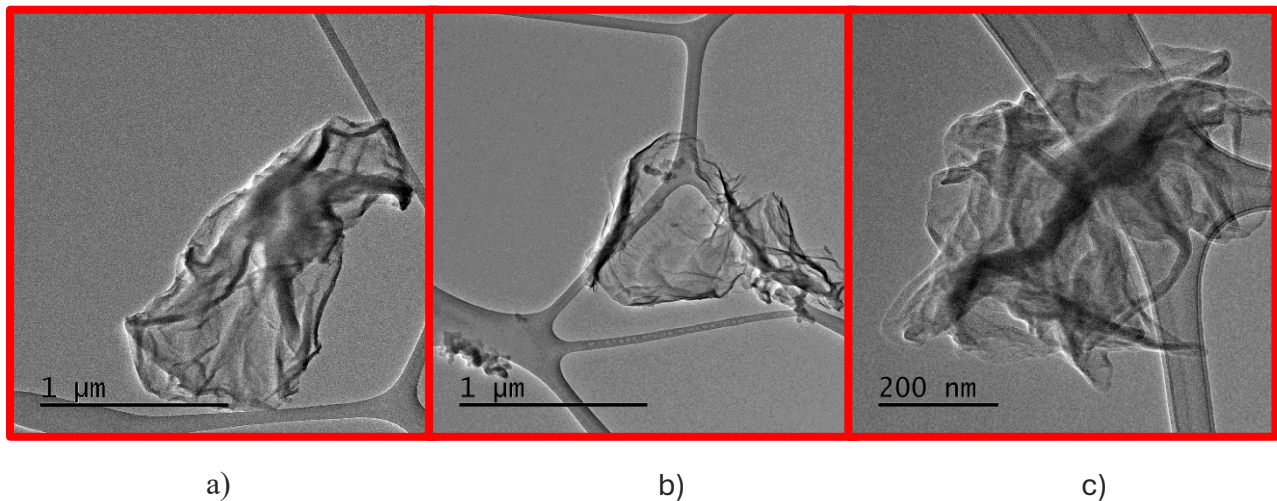


Figure 6-3: TEM images of drop cast tube furnace synthesized rGO

Due to the varying sizes, determining the Kn number is difficult; however, using a nominal characteristic length of 1 μm and applying Eq. (3.22) with argon as the motive gas, the Kn number is approximately 0.35. This is below the threshold as indicated in Figure 2-2. However, for the purpose of analyzing general trends rather than exact values, the conduction cooling will be treated as occurring in the free-molecular regime.

6.1.3 BET-SSA measurements

The rGO powder deposited on the semi-permeable membrane was collected for *ex situ* SSA characterization using a Brunauer-Emmett-Teller specific surface area (BET-SSA) tester. Prior to analysis, the rGO powder was degassed for 17 hours at 150°C to remove impurities. Subsequently, the degassed powder was loaded into the BET-SSA tester (Micromeritics Gemini VII 2390a [146]). The Gemini VII 2390a utilizes the static volumetric technique as outlined by ASTM D6556-21[147]. In brief, the analyzer operates by metering nitrogen gas into a sample tube containing the rGO powder and a reference tube. Transducers maintain equal pressure between the two tubes, allowing nitrogen to adsorb onto the sample's surface. The difference in gas quantity between the tubes is measured to determine the SSA. A schematic of the device is shown in Figure 6-4.

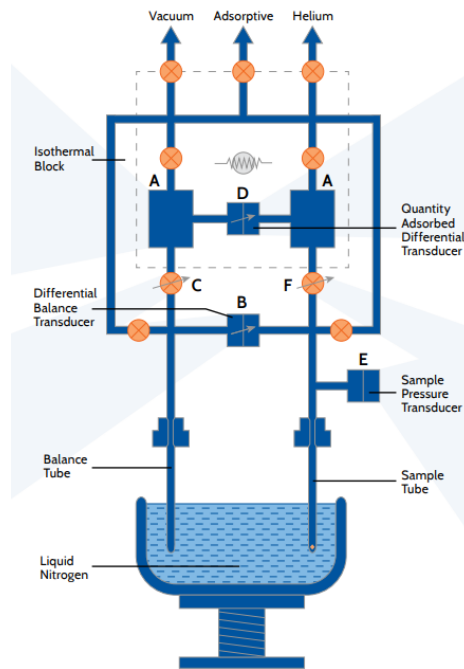


Figure 6-4: Schematic of the Gemini VII 2390a [146]

6.2 SSA results and discussion

6.2.1 TiRe-LII results

From each experiment, 10 runs were performed, with each run averaging 400 signals. The runs were further averaged to provide a single dataset containing intensity signals over time at 447 nm, 550 nm, 650 nm, and 747 nm. The data was then corrected using the calibration values determined through the process detailed in Appendix A.1. The temperature at each time step was then calculated using optical pyrometry according to Eq. (3.18). The temperature vs time curves derived for each experiment is shown in Figure 6-5. The maximum LII particle temperature can be described by equating the rate of internal energy change to the laser heating, assuming no cooling is taking place during the heating:

$$m_p c_p \frac{dT_p}{dt} = \dot{Q}_{\text{abs}} = F_0 F(t) \frac{\pi d_p^2}{4} Q_{\text{abs}, \lambda_{\text{laser}}} \quad (7.1)$$

where $F(t)$ is the laser temporal profile and $Q_{\text{abs}, \lambda_{\text{laser}}}$ is the absorption efficiency of the nanoparticle at the laser wavelength (1064 nm). It can be seen that since the fluence, F_0 , and $F(t)$ are constant over the experiments, the primary factors affecting the maximum particle temperature are the mass of the particle, m_p , the specific heat capacity of the particle, c_p , the diameter of the particle, d_p , and $Q_{\text{abs}, \lambda_{\text{laser}}}$. The particle size for rGO has been found to remain mostly constant across different reduction temperatures [15]; therefore, d_p can be assumed to be constant. Additionally, studies have suggested that the specific heat of graphite remains similar for graphene [148] and GO [149].

For the remaining two parameters, it has been shown that as GO reduces into rGO, m_p decreases due to loss of oxygen functional groups [15], while $Q_{\text{abs}, \lambda_{\text{laser}}}$ rises due to the restoration of the graphitic structure. The mass can decrease to approximately 60% of its original mass [15]; however, $Q_{\text{abs}, \lambda_{\text{laser}}}$ for GO is effectively zero, increasing greatly as it reduces [140]. Therefore, although the mass changes, at

initial degrees of reduction the absorption efficiency is the primary reason for the increase in maximum LII particle temperature. However, at higher degrees of reduction this may not be as pronounced.

In this study, the maximum particle temperature is lowest for a furnace setpoint of 500°C, gradually increasing to the highest temperature at 1100°C, before slightly decreasing at 1300°C. This trend aligns with the hypothesis above, as initial reduction significantly enhances the absorption efficiency. Additionally, the maximum LII temperatures found from reduction temperatures of 900°C, 1100°C, and 1300°C, are very similar with any fluctuations being indistinguishable from noise. This further reinforces the hypothesis, indicating that at higher degrees of reduction, the change in maximum temperature cannot be attributed to solely change in absorption efficiency and likely involves competing effects from mass loss.

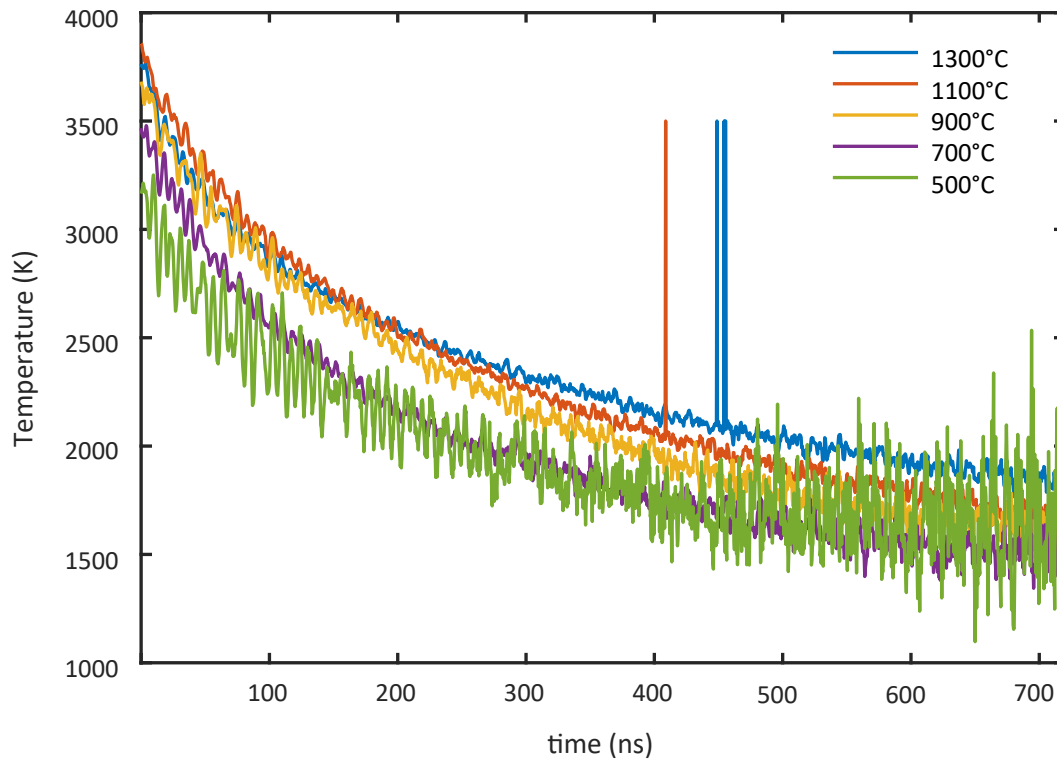


Figure 6-5: Pyrometrically determined temperatures for all five experiments

Following the analysis outlined in Section 2.1.3, a time period during which the cooling rate is dominated by conduction was chosen. It is expected that over this period, $\ln[\theta(t)]$, where $\theta(t)$ is the difference between the particle temperature and gas temperature, is approximately linear due to the exponential decay characteristic of conduction cooling as described in Section 2.1.2. To determine the appropriate time period for analysis, the particle temperature was converted to $\ln[\theta(t)]$ using a gas temperature of 293.15 K and plotted against time. From this plot, a linear relationship was observed between 250 ns and 450 ns, which was consequently chosen as the study region. Figure 6-6 presents the results of the linear regression and the $\ln[\theta(t)]$ versus time plot.

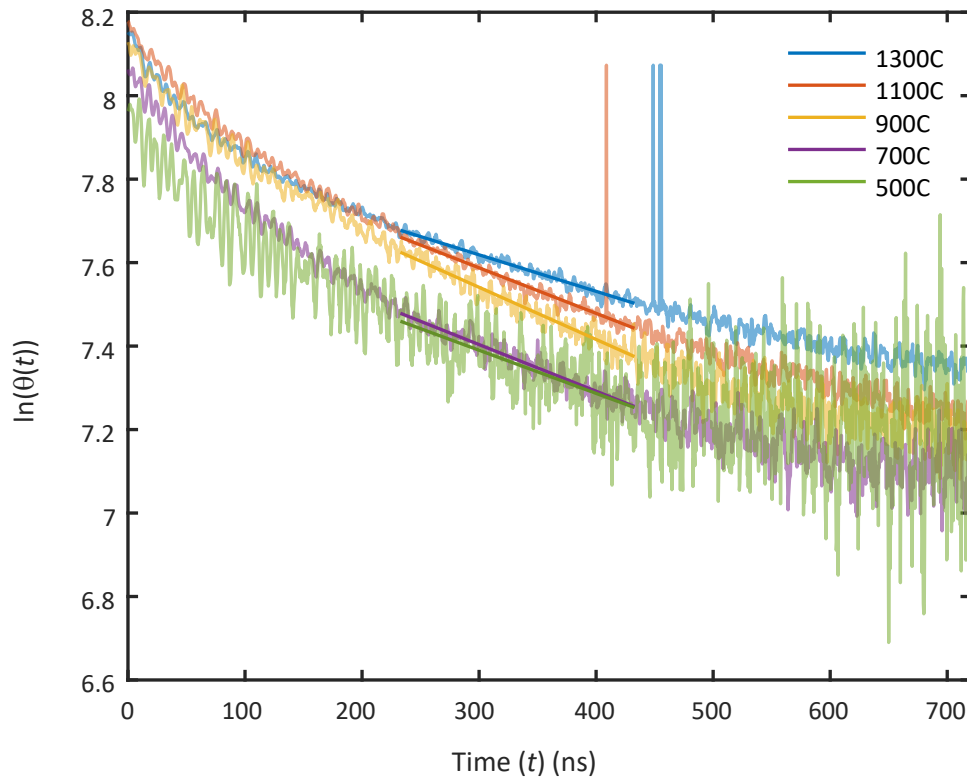


Figure 6-6: Linear regression of $\ln[\theta(t)]$ vs time

Using the slope determined from the linear regression, the SSA is derived from Eq. (3.30). The c_p ($2100 \text{ J kg}^{-1}\text{K}^{-1}$) and α_T (0.41) were sourced from studies by Pop et al. [148] and Daun et al./Snelling et al.

[44,71], respectively. Figure 6-7 shows the SSA as a function of reduction temperature. The vertical error bars represent one standard deviation of slope, as determined by linear regression.

The SSA increases from 187.7 m²/g at 500°C to a maximum value of 226.8 m²/g at 900°C before decreasing at 1100°C and 1300°C to a value of 158.8 m²/g. This trend aligns well with the evolution of rGO as a function of reduction temperature, as reported by Huh [36] and Sengupta et al.[37]. While the reduction temperatures in this study do not perfectly align with those presented by Huh and Sengupta, different thermal reduction processes were used. Both Huh and Sengupta et al. thermally reduced the GO powder in furnaces over an extended period of time (~1 hour), whereas in this study, the tube furnace was preheated, and rGO powder was rapidly passed through it. This difference likely shifted the reduction temperature range; however, the trends remained constant. Note, that the properties of rGO vary significantly with GO synthesis and thermal reduction conditions; therefore, the conclusions reached by Huh and Sengupta et al. may not be universally applicable to all thermally reduced rGO. Nonetheless, the good agreement between the rGO presented by Huh and Sengupta et al. and this work indicates that the rGO formed is similar to those reported by Huh and Sengupta et al. Microscopy can be conducted on the rGO particles produced in this study to verify this hypothesis; however due to the good agreement observed, the trends identified in this work will be discussed in relation to those reported by Huh and Sengupta et al. Additionally, as the trends reported in both literature results are similar, the discussion will primarily refer to the results presented by Huh.

The initial increase in experimental SSA can be attributed to the further removal of oxygen functional groups as the temperature rises. However, as shown by Huh [36], at a reduction temperature of approximately 800°C the lowest concentration of oxygen is present without the formation of structural defects. Therefore, the maximum experimental SSA observed at 900°C is consistent with the trends described by Huh [36]. Beyond 800-1000°C, the structural defects increase, reaching their peak at 1000°C. The rise in structural defects reduces the accessible surface area for adsorption, thereby

decreasing the SSA. Additionally, TEM imaging has shown that at reduction temperatures of 1000°C and above, previously folded or crumpled rGO structures tend to unfold into a flatter configuration [36]. This further reduces the SSA, as flat structures are more prone to restacking or aggregation, diminishing their overall surface area [133]. This phenomenon is reflected in the drop in experimental SSA at 1100°C. Beyond 1000°C, the graphitic lattice restores itself due to thermal annealing; however, rGO sheets begin to restack, increasingly resembling graphite at higher reduction temperatures. As a result, the SSA is expected to continue decreasing, which is evident from the lowest experimental SSA observed at 1300°C.

Additionally, the magnitude of the experimental SSA is consistent with the SSA values reported by Zhao et al [150] and Alazmi et al. [151]. Zhao et al. [150] reduced GO sheets using a horizontal tube furnace with a heating rate of 5°C/min, varying the reduction temperature from 200 to 900°C. Their SSA values ranged from 12 m²/g at a reduction temperature of 150°C to max SSA of 227.05 m²/g at 500°C, before decreasing to 154 m²/g at 900 °C. A clear similarity in the trends of the SSA found in this study is seen, with the SSA increasing to a critical temperature before declining. The difference in critical temperature can be attributed to variations in reduction procedures, similar to Huh [36]. Alazmi et al. [151] hydrothermally reduced GO and derived a SSA of 364 m²/g, again similar in magnitude to the SSA found in this study.

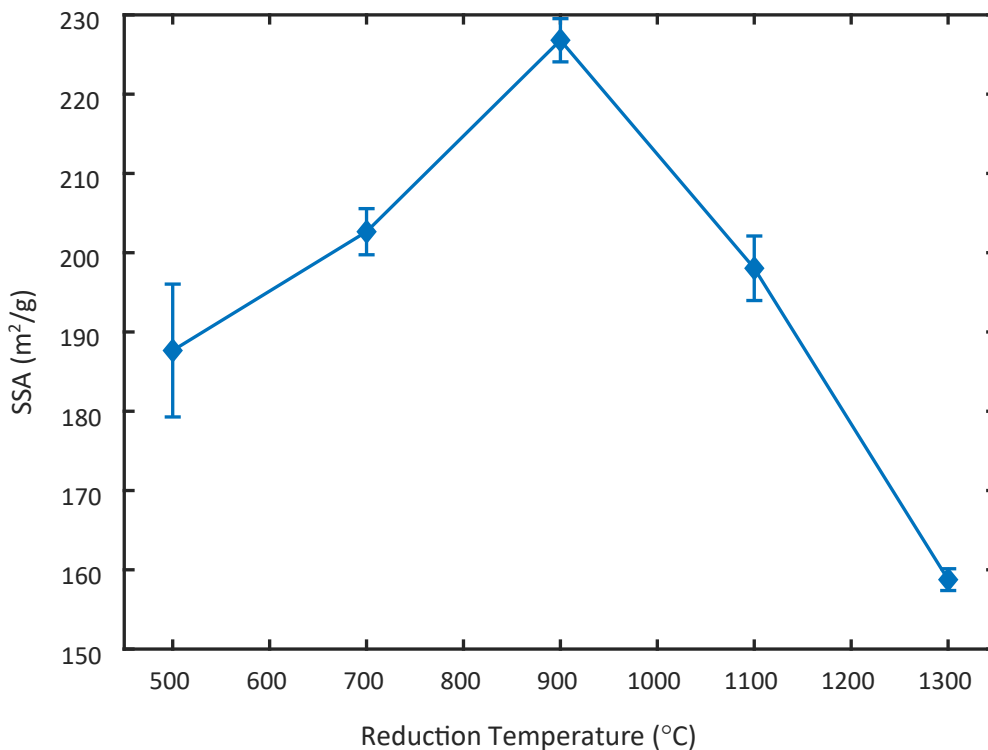


Figure 6-7: LII-inferred SSA vs Reduction temperature

6.2.2 BET-SSA results

Brunauer-Emmett-Teller specific surface area (BET-SSA) testing was performed with sample masses of approximately 0.01 g for all samples. Figure 6-8 shows the SSA results derived from LII and BET measurements. The BET results align extremely well with the LII results, both in trend and magnitude. The critical reduction temperature was found to be 900°C, corresponding to the highest SSA value of 166.30 m²/g. The lowest SSA value of 66.87 m²/g was found at 1300°C, similar to TiRe-LII results. The agreement of the trends further reinforces the conclusions reached in Section 6.2.1. The initial rise in SSA is due to the removal of oxygen functional groups until a critical temperature of around 900°C, at which point the SSA drops significantly due to the introduction of structural defects and unfolding. It is important to note that in other literature results, the SSA of rGO has been shown to reach values of 700-1850 m²/g [35,152]; therefore, the low SSA derived from the rGO indicates that the thermal reduction was

not efficient, with potentially burning occurring due to leaks in the system. Nonetheless, this work still shows the potential for measuring SSA using TiRe-LII.

In the BET samples, the SSA varies more substantially from 500°C to 700°C, as well as between 1100 °C to 1300°C. The discrepancy can be attributed to noise during the experiments and the assumption that the thermal accommodation coefficient, α_T , and specific heat capacity, c_p , remain constant throughout the experiment. Notably, the highest discrepancy occurs between 500°C and 700°C. At 500°C, the highest noise in the data was observed, likely due to the rGO samples exhibiting low absorption as a result of their lower degree of reduction. While this is partially captured by the vertical error bars, additional inaccuracies may have been introduced due to model error when deriving the pyrometric temperature. This issue can be investigated and accounted for in future work.

Furthermore, previous studies have shown that as oxygen content decreases in rGO samples, their optical properties change [16,140,153]. Therefore, assuming a constant α_T and c_p may slightly skew the values relative to one another. A study examining how α_T and c_p change with reduction temperature would be beneficial in deriving a more accurate trend.

Additionally, it is found that the magnitude of the SSA values are similar, indicating that the free-molecular regime is likely a valid assumption for deriving a representative SSA. However, a study should still be conducted to determine whether the transition regime can provide more accurate SSA values. The discrepancies in value can likely be attributed to assumptions made for α_T and c_p . These values were taken from literature data on soot [44,71] and graphite [148] and may slightly differ in rGO. Nonetheless, the good degree of fit of the trends and magnitude clearly demonstrates the applicability of TiRe-LII in deriving a realistic SSA for rGO in real-time.

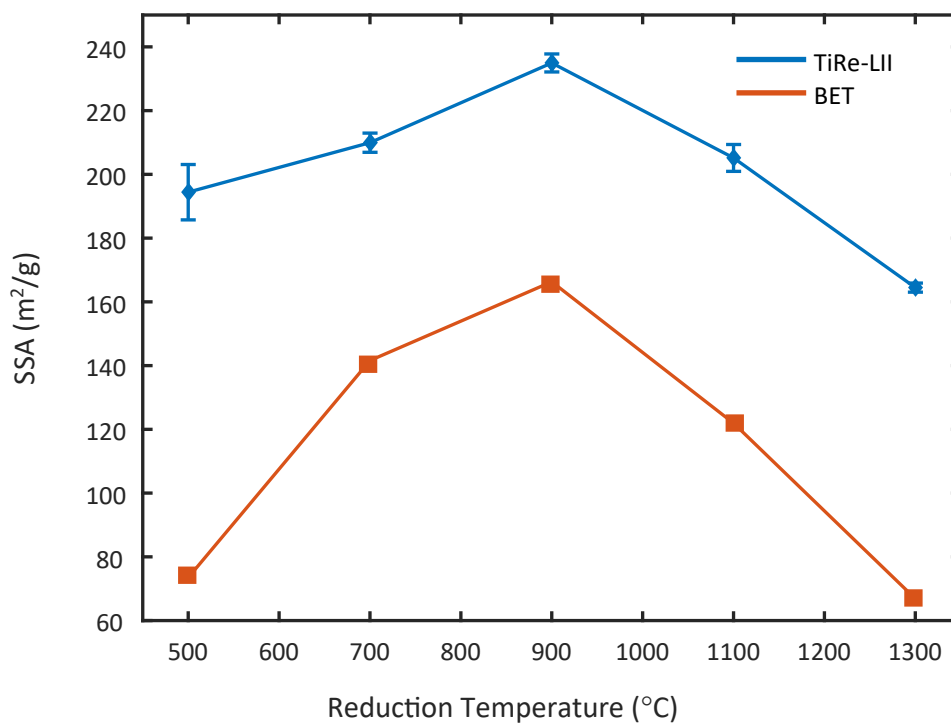


Figure 6-8: SSA vs Reduction temperature comparing TiRe-LII and BET derived results

6.3 Summary

This chapter presents the SSA values for five reduction temperatures (500°C, 700°C, 900°C, 1100°C, 1300°C), derived from online TiRe-LII experiments and *ex situ* BET-SSA measurements. The trends observed from the relative SSA values obtained from TiRe-LII align well with prior work reported by Huh [36], Zhao et al. [150], and Alazmi et al. [151]. The SSA increases to a peak value at 900°C, as higher reduction temperatures lead to lower oxygen content. However, beyond this temperature, the SSA decreases due to the formation of structural defects and unfolding, which results in restacking and reaggregation. The strong agreement with prior work confirms that TiRe-LII is a useful diagnostic tool for determining the relative size and morphology of GO in real-time. Additionally, BET-SSA measurements yielded SSA values with very similar trends and magnitude, further reinforcing the ability of TiRe-LII to derive realistic SSA values in real time.

Further research is needed to define the specific heat capacity and thermal accommodation coefficient of rGO to determine its absolute SSA. Additionally, a more in-depth study of the appropriate conduction regime would be beneficial, as the derived Knudsen number suggests that the physics of conduction cooling follow the transition regime rather than the free-molecular regime used in this study.

Chapter 6 confirms that TiRe-LII can provide real-time information on the specific surface area and morphology of the synthesized rGO particles; however, the electrical conductivity of the derived rGO remains unknown. Chapter 7 will investigate whether LOSA can provide this information in real-time, further enhancing the characterization of rGO.

Chapter 7

Online extinction characterization of plasma reduction of rGO

7.1 Experimental Set-up

To assess the applicability of extinction characterization, two different methods will be employed. The first experimental method uses the apparatus described in Section 3.3 to evaluate the feasibility of online extinction measurements. However, a second experimental method is necessary to validate the Lorentz-Drude model, as there is a limited understanding of how plasma reduction affects the characteristics of the synthesized rGO and because the current LOSA apparatus has a limited wavelength range. In contrast, UV-vis spectrometry on a colloid is well established and can provide spectral data in the UV and infrared wavelengths. Therefore, it will be used to determine the spectrally resolved absorptivity of GO to rGO across multiple reduction steps. The Lorentz-Drude model will then be applied to the data to derive the electrical conductivity.

7.1.1 Gas-phase LOSA measurements

The online extinction measurement of GO and rGO was conducted using the apparatus described in Section 3.3. Graphene oxide powder was placed on a semi-permeable membrane inside the nebulizer. Argon and nitrogen gases were directed into the nebulizer at 1.73 slpm and 0.02 slpm, respectively, to carry the GO into the plasma reactor. Swirl gases, consisting of 6.6 slpm of argon and 0.5 slpm of hydrogen, were used to stabilize the flow, creating a sharp gas stream, as shown in Figure 7-1. A window flush of nitrogen gas, flowing at 4 slpm, is used to keep the windows clear of powder during measurements.

During GO experiments, the swirl gas and microwave power were turned off to prevent any reduction. For rGO experiments, the plasma microwave power was set to 600 W with an operating pressure of 10.23 kPa. The exposure time of the EMCCD was set to 1300 ms, with the grating density of

the spectrometer set to 300 g/mm at a center wavelength of 450 nm, providing a 330 nm – 550 nm spectral range.

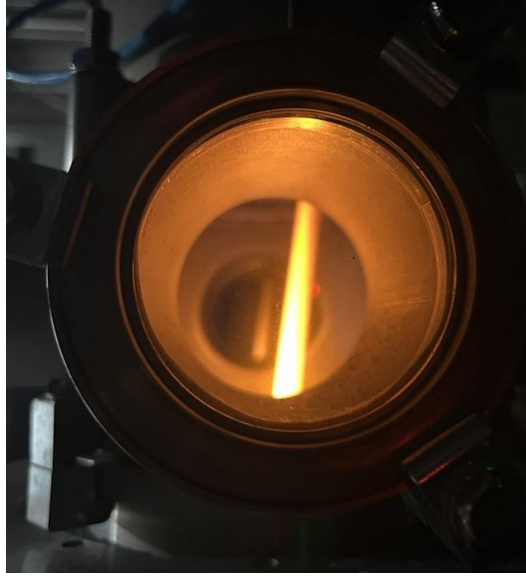


Figure 7-1: Image of heated aerosol flow through plasma reactor

The experiment consisted of four different settings that varied the laser driven light source (LDLS) and the rGO aerosol stream. First, the LDLS was unblocked, with the flow passing through the nebulizer, allowing for the light attenuated by rGO aerosol stream to be recorded ($I_{\lambda, LIP1}$). Next, the LDLS was blocked, and the flow passed through the nebulizer, allowing the thermal emission of the heated particle stream to be recorded ($I_{\lambda, LOP1}$). Then, the LDLS was unblocked, and the flow bypassed the nebulizer, allowing the light attenuated by the carrier gases to be recorded ($I_{\lambda, LIP0}$). Finally, with the LDLS blocked and the flow bypassing the nebulizer, the background light intensity ($I_{\lambda, LOP0}$) was recorded. This set of experiments was conducted once per material (GO and rGO) due to the limited supply of GO available. During this run, the light intensity at each setting was averaged over one minute. Using the averaged signals, the spectral absorbance of the aerosol stream was derived according to:

$$A_{\lambda} = \log_{10} \left(\frac{I_{\lambda}}{I_{\lambda,0}} \right) = \frac{I_{\lambda, LIP1} - I_{\lambda, LIP0}}{I_{\lambda, LOP1} - I_{\lambda, LOP0}} \quad (8.1)$$

The absorptivity can be assessed to determine the viability of using LOSA to measure the spectrally resolved extinction spectrum for gas-phase GO and rGO. However, due to the limited amount of material, the narrow wavelength range, and the difficulty in modifying the degree of reduction, UV-Vis spectroscopic analysis is conducted on GO and rGO colloids to validate the Lorentz-Drude model, which can then be applied to interpret LOSA gas phase measurements.

7.1.2 Colloidal UV-Vis spectroscopic analysis

To perform UV-Vis spectroscopic analysis, colloids of rGO at different reduction steps must be used. This poses a challenge because, while GO is easily dispersed in water, its hydrophilicity decreases as it is reduced and oxygen groups are removed, causing it to precipitate. Consequently, a reduction method that retains the dispersibility of GO in water is required. To achieve this, GO was reduced following the procedure reported by Li et al. [140].

In brief, GO powder synthesized according to Section 3.1.1 was dispersed in 5 ml of Milli-Q (MQ) water to form a 0.5 wt% colloid. The GO colloid was then ultrasonicated using a bath ultrasonicator to ensure the GO was exfoliated. Subsequently, the colloid was subjected to 30 minutes of centrifugation at 3000 rpm to remove any unexfoliated GO. Reduction was carried out using hydrazine and ammonia, with ammonia used to control the pH of the reaction solution, as this has been shown to help rGO remain dispersible in a water-based solution [154]. The GO colloid was mixed with a solution containing 10.0 ml of MQ water, 10.0 μ l of hydrazine solution (35 wt% in MQ water), and 75.0 μ l of ammonia solution (28 wt% in MQ water). The reaction solution was vigorously shaken for a few minutes and then placed into a water bath heated to 100°C for one hour. The degree of reduction of rGO produced using this method primarily depends on the reduction time. Consequently, at various time intervals (2 min, 5 min, 10 min, 15 min, 30 min, and 1 hour), 0.5 ml of the reaction mixture was extracted, diluted with MQ water at a 1:1 ratio, and measured using a UV-Vis spectrometer (ThermoFisher Scientific Evolution 300). Additionally,

the GO colloid prior to reduction was measured. The colloids analyzed, minus the GO, are shown in Figure 7-2.

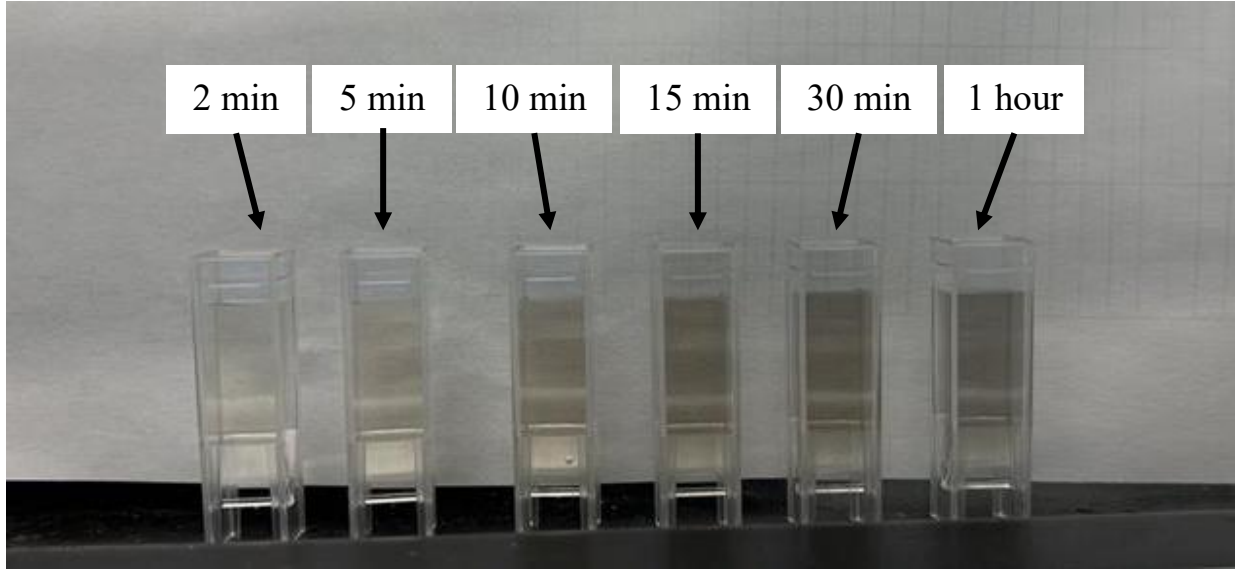


Figure 7-2: rGO colloids after different reduction durations

The UV-Vis spectrometer measures the absorbance of the sample according to:

$$A_{\lambda} = \log_{10} \left(\frac{I_{\lambda,0}}{I_{\lambda}} \right) = -\kappa_{abs} L \quad (8.2)$$

In this study, the absorbance is derived using log base 10 to allow for comparison with literature results. A cuvette containing the sample is placed into the device, with another cuvette containing MQ water serving as a reference. A xenon flash lamp is used to produce broadband light, which is then focused into a specific wavelength by a spectral grating and passed through the two cuvettes [155]. The absorptivity of the medium at that specific wavelength is derived by taking a ratio of the incident ($I_{\lambda,0}$) and transmitted light (I_{λ}). The wavelength is then varied from 200 nm to 800 nm, allowing the formation of a spectral absorbance plot in that range. The measurement was repeated three times at each reduction time, and the results were averaged to derive seven spectral absorbance plots. The next section details the procedure

used to evaluate the credibility of applying the Lorentz-Drude theory to spectral absorbance data to derive the electrical conductivity of rGO.

7.1.3 Lorentz-Drude modelling

To apply the Lorentz-Drude model, the absorbance data can be connected to the dielectric function via the equations and procedure outlined in Section 2.2. The dielectric function, as described by Eq. (3.37) and Eq. (3.38), can be split into its real (ε_{λ}') and imaginary (ε_{λ}'') components:

$$\varepsilon_{\lambda}' = \varepsilon_0 + \frac{e^2}{m_v \gamma_0} \sum_j \frac{n_{bj} (\omega_{bj}^2 - \omega^2)}{(\omega_{bj}^2 - \omega^2)^2 + \omega^2 \gamma_{bj}^2} - \left(\frac{e^2}{m_d \gamma_0} \right) \frac{n_d}{\omega^2 + \gamma_d^2} \quad (8.3)$$

$$\varepsilon_{\lambda}'' = \frac{e^2}{m_v \gamma_0} \sum_j \frac{n_{bj} \omega^2 \gamma_{bj}}{(\omega_{bj}^2 - \omega^2)^2 + \omega^2 \gamma_{bj}^2} + \left(\frac{e^2}{m_d \gamma_0} \right) \frac{n_d \gamma_d}{\omega (\omega^2 + \gamma_d^2)} \quad (8.4)$$

Using Eq. (3.35) and (3.36), the dielectric components are directly related to the complex refractive index (m_{λ}). Assuming the particle is in the Rayleigh regime, Eq. (3.14) can be used to solve for the absorption function, $E(m_{\lambda})$. The absorption function can then be used to determine the absorption cross-section, $C_{\text{abs},\lambda}$, via Eq. (3.12) and (3.34). Finally, using the absorption cross-section, the absorption coefficient, $\kappa_{\text{abs},\lambda}$, can be found using Eq. (3.33). Note that the particle diameter, d_p , and number density of particles, n_p , are unknown and not desired in this solution; as a result, they are combined into a nuisance parameter, C_n . Additionally, it is simpler to express the equation in terms of transmissivity, $\tau = I_{\lambda}/I_{\lambda,0}$; hence, the experimental absorbance will be converted into τ_{exp} . Rearranging Eq. (3.32), a modelled transmissivity (τ_m) can be derived:

$$\tau_m = \frac{I_{\lambda}}{I_{\lambda,0}} = \exp(-\kappa_{\text{abs},\lambda} L) \quad (8.5)$$

Using this model, the maximum likelihood estimation, x_{MLE} , of the dielectric function can be solved for using a least square minimization:

$$x_{\text{MLE}} = \underset{x}{\operatorname{argmin}} \left\| W(\tau_{\text{exp}} - \tau_m) \right\|^2 \quad (8.6)$$

where W is a weighting matrix used to account for heteroskedastic noise in the experimental data.

As an initial test, the GO/rGO will be assumed to have two Lorentz oscillators and a single Drude oscillator, following the Lorentz-Drude models derived for soot [156,157]. With two Lorentz oscillators and a single Drude oscillator, there are ten variables that the solver needs to minimize: C_n , ε_0 , n_{b1} , n_{b2} , n_d , γ_{b1} , γ_{b2} , γ_d , ω_{b1} , and ω_{b2} . To limit the solution space of the model, assumptions are made based on the soot model. It is assumed that ε_0 equals unity, as is commonly done in soot modelling [76,157]. Additionally, n_{b2} will be connected to n_{b1} and n_d following [158]:

$$n_{b2} = 11n_{b1} - n_d \quad (8.7)$$

and γ_d will be defined as [158]:

$$\gamma_d = \frac{3}{4l_0} \sqrt{\frac{2\pi k_B T_p}{m^*}} \quad (8.8)$$

where $l_0 = 1$ nm is the mean free path of conduction electrons, and $T_p = 293.15$ K is the particle temperature. This simplifies the minimization to seven variables. Non-negativity constraints were applied to all variables to prevent non-physical solutions and an upper bound of 250 nm was set for ω_{b1} , based on the resonant frequency observed around this wavelength in rGO samples reported in the literature [140,153]. Additionally, initial tests revealed a high covariance between n_d and ω_{b2} , leading to multiple possible solutions. To address this, either n_d or ω_{b2} can be fixed during the minimization. The number of mobile electrons, n_d , is expected to vary significantly among samples due to different degrees of reduction, while ω_{b2} is expected to remain relatively constant, owing to the minimal variation in resonant frequencies associated with the degree of reduction [140,153]. Therefore, ω_{b2} was fixed at $7.0 \times 10^{15} \text{ s}^{-1}$,

as determined from the initial fit. Using the maximum likelihood estimate, the DC conductivity was calculated by solving for the electrical conductivity at large wavelengths.

7.2 Results and discussion

7.2.1 LOSA online measurement

The raw intensities recorded during the rGO experiment are shown in Figure 7-3. These intensities reveal the effective wavelength range of the LDLS in conjunction with the spectrometer/EMCCD. Analysis of subplots L1P0 and L1P1 indicate that the EMCCD effectively detects high-intensity signals between 350 nm and 560 nm. Consequently, this wavelength range is the primary focus of subsequent analyses. Further examination shows that the intensity counts in subplot L1P0 and L1P1 are comparable. This outcome is expected due to the large probe volume and low particle concentration of the LOSA apparatus, resulting in minimal light attenuation. Nonetheless, the high sensitivity of the spectrometer/EMCCD facilitates the derivation of a spectral absorbance plot within this range.

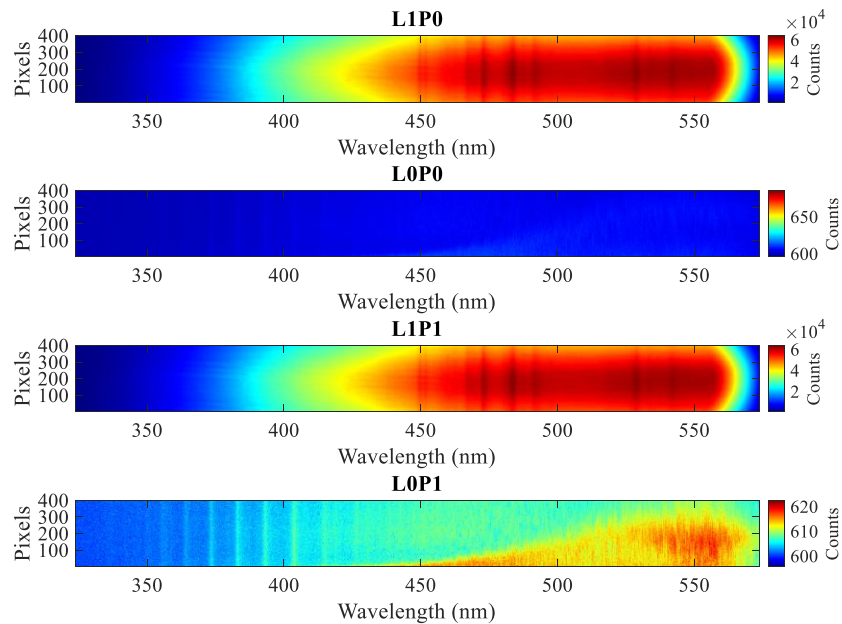


Figure 7-3: Raw intensity images of the four settings: L1P0 (LDLS unblocked, gas only), L0P0 (LDLS blocked, gas only), L1P1 (LDLS unblocked, GO aerosol), L0P1 (LDLS blocked, GO aerosol)

Even with the high sensitivity of the EMCCD, no appreciable attenuation was detected during the GO experiments. This lack of attenuation is likely due to the low absorption of GO compared to rGO between 350 nm and 560 nm [140]. Studies have shown that both rGO and GO dispersions exhibit absorption peaks around 250 nm, with a significant drop in absorption at wavelengths longer than 400 nm, attributed to its insulating nature resulting from oxygen functional groups. In contrast, rGO maintains absorption at longer wavelengths, including the near-infrared region, due to its higher electron mobility and reduced oxygen content.

As expected, rGO exhibits clear attenuation, albeit at a low magnitude due to the low particle concentration. Consequently, instead of absolute absorptivity, the change in absorptivity with respect to wavelength is examined. The spectral absorbance plot of the gas-phase rGO is shown in Figure 7-4. The decreasing trend as the wavelength increases aligns well with literature results, which show that rGO has resonant frequencies around 250 nm and 300 nm [153]. Additionally, the absorbance plateaus around 450 nm, exhibiting broadband absorption, as expected with rGO.

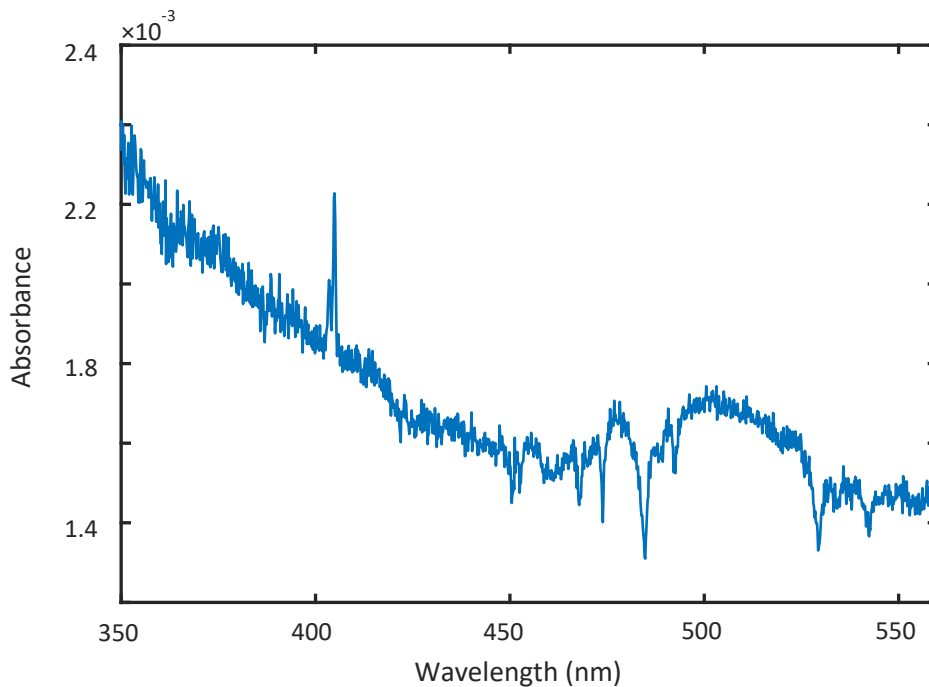


Figure 7-4: Spectral Absorbance plot derived from LOSA of rGO

However, due to the limited wavelength range, it cannot be fully confirmed whether this spectrum is a definitive characteristic of solely rGO. The key identifying features in the absorbance spectrum for rGO and GO are resonant frequencies in the UV range. Therefore, for future LOSA experiments, a spectrometer/EMCCD capable of measuring in the UV wavelength range would provide more information for rGO and/or GO. Nonetheless, the attenuation shows that LOSA is a viable real-time diagnostic for rGO and potentially for GO. With the extinction spectrum provide by LOSA, a Lorentz-Drude model can be applied to derive functional properties. This is demonstrated in the subsequent sections using the extinction spectrum derived from UV-Vis spectroscopy.

7.2.2 Colloidal UV-Vis spectroscopic measurement

Seven spectral absorption plots from 200 nm to 800 nm are derived from the UV-Vis spectroscopic colloidal study. Upon initial visualization, it was observed that the first 10 nm were non-physical and were subsequently removed. Additionally, it was determined that the noise of the plot varied at different wavelengths. To model the noise and smooth the data for model fitting, the plot was divided into five-nanometer-wide bins. Within each bin, the standard deviation (σ_b) and mean (μ_b) were calculated. Figure 7-5 shows the spectral absorbance plot, comparing the binned data to the experimental data derived from the colloid after 60 minutes of reduction.

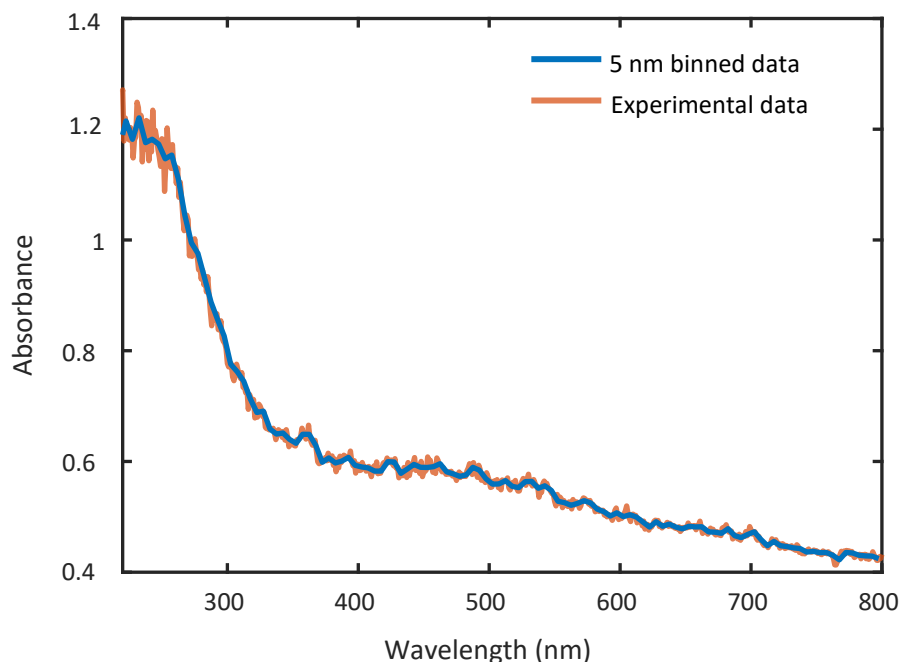


Figure 7-5: Spectral absorbance plot comparing binned data to experimental data – 60 min reduction time

Figure 7-6 shows the spectral absorption plots for the colloids at the seven reduction durations measured in this study, as well as the eight reduction durations measured by Li et al. [140]. The general trends align well between the two studies. The peak absorbance is observed between 200 nm and 300 nm for all reduction durations, as expected due to the resonant frequencies present in that region [153]. Additionally, as the reaction time increases, absorption in the broadband region (> 400 nm) also increases, suggesting restoration of the graphitic lattice and the removal of oxygen functional groups. Furthermore, in both plots, there is little increase in broadband absorption from a reduction duration of 30 minutes to 60 minutes, indicating the completion of the reduction process. Nonetheless, two differences are noted between the plots: the absorbance peak around 250 nm and the change in absorptivity observed in the experimental data (circled in a dotted black line).

In the plot reported by Li et al. [140], there is a clear increase in both the position of the absorbance peak and the magnitude, which is not present in the experimental data derived from this study. The shift in absorbance matches prior studies in the literature [153], suggesting that this shift should be

present in the experimental data. A potential reason for its absence could be that the data was found to be very noisy below 300 nm due to the reduced quantum efficiency near the limits of the detector. Additionally, the magnitude of the peak absorbance remains constant across all reaction times. This may again be a limit of the spectrometer as the transmissivity at this point is approximately 5%, making it difficult to measure higher absorbance. To circumvent this, in subsequent experiments a low concentration of the samples can be studied.

The other significant difference between the two plots is a point of inflection seen at around 500 nm to 550 nm. This is primarily visible in data derived from reaction times of 30 minutes and 60 minutes but is not present in any of the data reported by Li et al [140]. This inflection suggests a change in absorption characteristics due to unknown physical processes. The absence of this inflection in the data presented by Li et al. [140], along with the lack of literature data detailing the physical processes in GO/rGO that would lead to this change, suggests that impurities in the colloid (such as unreacted hydrazine or ammonia) may have caused the inflection; however, further research is necessary to determine the exact cause. Nonetheless, as the general trends were recovered, this data will be used to assess the Lorentz-Drude model.

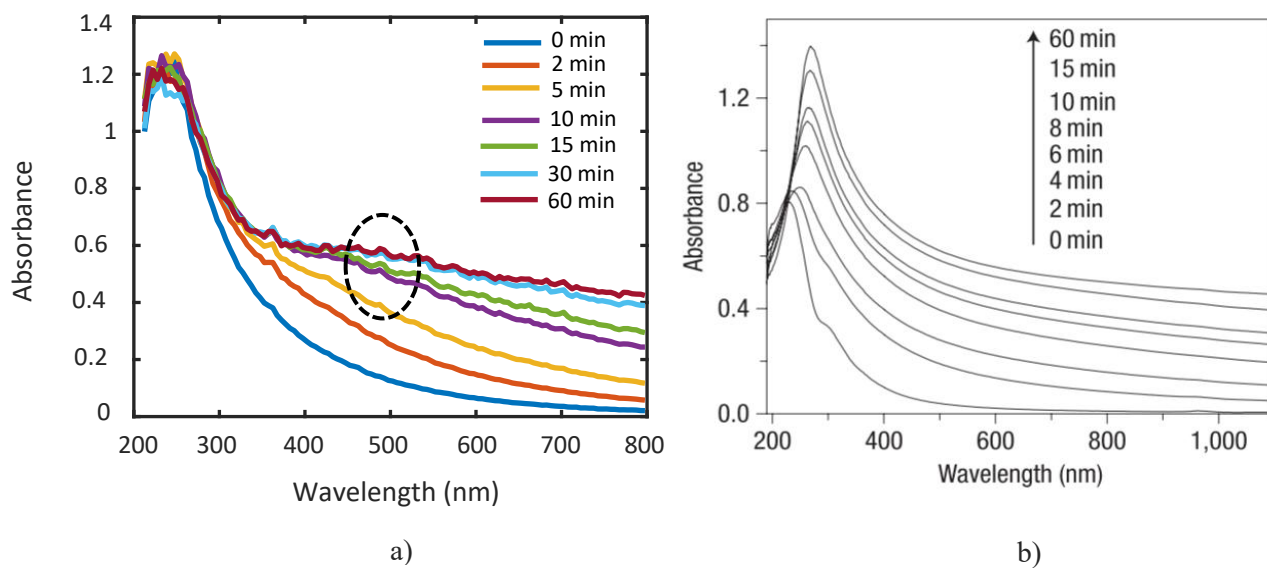


Figure 7-6: Spectral absorbance of GO after different reduction durations: a) from this experiment b) presented by Li et al. [140]

7.2.3 Lorentz-Drude model validation

Figure 7-7 shows examples of the fit for the GO (zero minute) and fully reduced rGO (60 minute) samples. For both datasets, a good degree of fit is observed, with the trends of the experimental data captured well. For the rGO model, there is some slight deviation in the curve around 250 nm and 550 nm; however, the deviations can be attributed to the higher signal to noise ratio, due to a lower change in transmissivity, and model error attributed to the inflection shown in Figure 7-6.

To improve the degree of fit, instead of using fixed values derived from soot studies, experiments can be conducted to determine dielectric parameters for the GO/rGO formed in this study. This can be done through simulation studies, such as density functional theory (DFT) calculations [159], and/or through *ex situ* studies, such as spectroscopic ellipsometry [141,160]. Additionally, further experiments across larger wavelength ranges will provide more accurate model data, and repeated experiments would help to determine whether the inflection is due to impurities in the sample or unknown physical phenomena. If the latter is found to be true, more advanced models, such as the Drude-Smith model [161] or an extended Drude model [162], could be considered. Nonetheless, the strong degree of fit demonstrates that the Lorentz-Drude model can accurately resolve the spectral absorption data and determine the dielectric constants of the material.

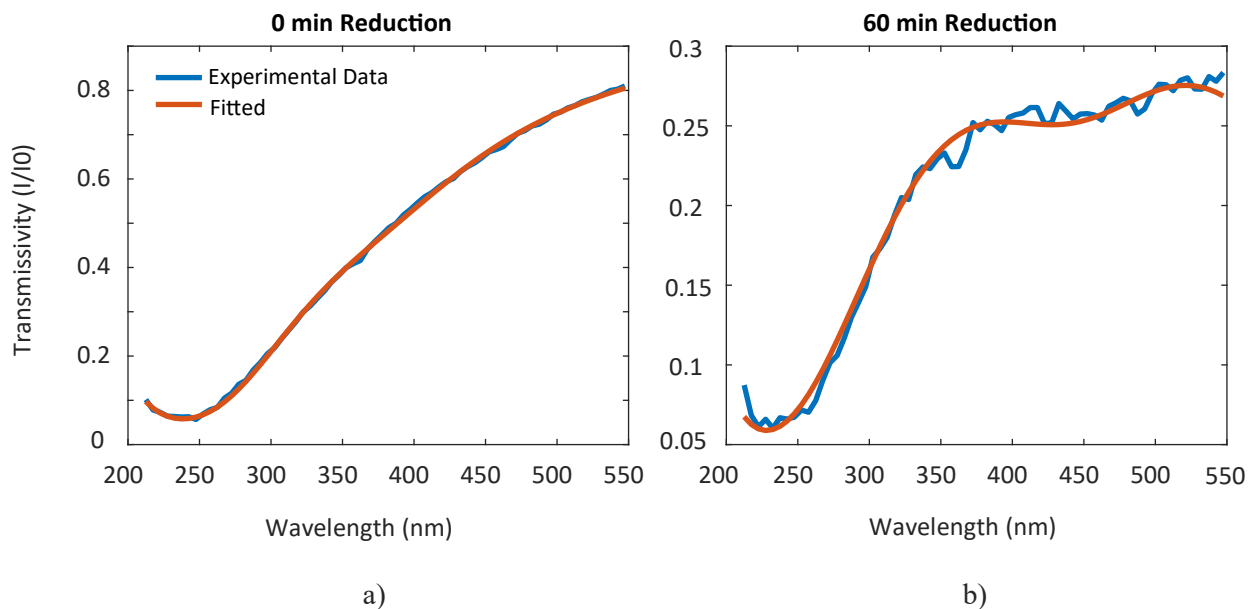


Figure 7-7: Comparison of experimental data vs Lorentz-Drude fit: a) GO (0 min) b) rGO (60 min)

From the Lorentz-Drude model, the derived maximum likelihood estimates (x_{MLE}) for each of the seven parameters are listed in Table 2 below. The values show that the Lorentz oscillators remain relatively constant across all reduction times (n_{b1} , n_{b2} , γ_{b1} , γ_{b2} , and ω_{b1}). This is expected, as results in the literature demonstrate minimal shifting in the resonant frequency as GO reduces into rGO [140,153]. Additionally, as mentioned in Section 7.2.2, the peak of the absorptivity remained similar in both magnitude and spectral position. The peak in absorptivity is due to the resonant frequencies, which have been captured well by the Lorentz oscillators. The primary difference arises from n_d , which denotes the number density of mobile electrons. The fitted results match expected trends, as it is anticipated that this value will increase as the graphitic structure is restored during the reaction process. Note the small value of n_d for the GO (0 min), which signifies little to no effect from the Drude oscillator.

Table 2: Derived Lorenz-Drude Parameters

Reduction	n_{b1}	n_{b2}	n_d	γ_{b1}	γ_{b2}	ω_{b1}	C_n
Duration	($\times 10^{27}m^{-3}$)	($\times 10^{28}m^{-3}$)	($\times 10^{25}m^{-3}$)	($\times 10^{15}s^{-1}$)	($\times 10^{16}s^{-1}$)	($\times 10^{15}s^{-1}$)	

0 min	1.157	1.27	2.23E-14	2.253	0.387	4.845	144.625
2 min	1.890	2.07	8.947	2.286	0.616	4.245	131.224
5 min	1.619	1.75	28.106	1.885	0.538	4.109	125.795
10 min	1.591	1.71	40.868	1.857	0.536	3.977	117.330
15 min	1.462	1.57	42.985	1.825	0.526	4.023	117.549
30 min	1.537	1.64	49.701	2.001	0.544	4.022	106.876
60 min	1.799	1.92	57.857	1.903	0.551	3.909	94.195

From the least square minimization, the Jacobian, J_f , can also be derived. The Jacobian is defined as the local linear transformation of the function and provides information on how the fit will change with respect to each variable. Using J_f , the covariance matrix (Γ_x) of the function can be found by:

$$\Gamma_x = [J_f^T(x_{MLE})J_f(x_{MLE})]^{-1} \quad (8.9)$$

From the covariance matrix, the standard deviation (σ_x) of each parameter can be derived by taking the variance of the parameters (diagonal of the matrix) and compute the square root. Assuming a normal distribution, σ_x and x_{MLE} can then be used to derive a 95% credibility interval (CI) ($2\sigma_x$) for each parameter. Figure 7-8 and Figure 7-9 show a probability density function (PDF) of the possible values with the x_{MLE} and a 95% credibility interval denoted for GO (0 min reduction duration) and rGO (60 min reduction duration), respectively.

For Figure 7-9, all variables have a relatively narrow 95% CI, implying that with the selected fixed values, the model can determine the dielectric function with a good degree of certainty. For Figure 7-8, while this is the case for a majority of the variables, n_d has a wide CI with the x_{MLE} being very small. This implies that either the data provided (i.e., absorbance between 210 nm to 550 nm) is insufficient to resolve n_d with a good degree of credibility, or n_d has little to no effect on the fit. In this case, it is

assumed that n_d has little to no effect. Due to the low broadband absorption shown by GO [140], it is expected that there are few to no mobile electrons present in the material. This will correlate to a low n_d relative to n_{b1} and minimal contribution by the Drude oscillator. Consequently, any $n_d \ll n_{b1}$ can be fit to derive the same spectral absorbance. Due to the high variance of n_d , it will be difficult to derive a credible DC conductivity. However, this is expected, as GO has an experimentally derived DC conductivity much lower than rGO [28]. Additionally, the other six reduction durations show a much less variable n_d , comparable to rGO (Figure 7-9), allowing the determination of a credible DC conductivity.

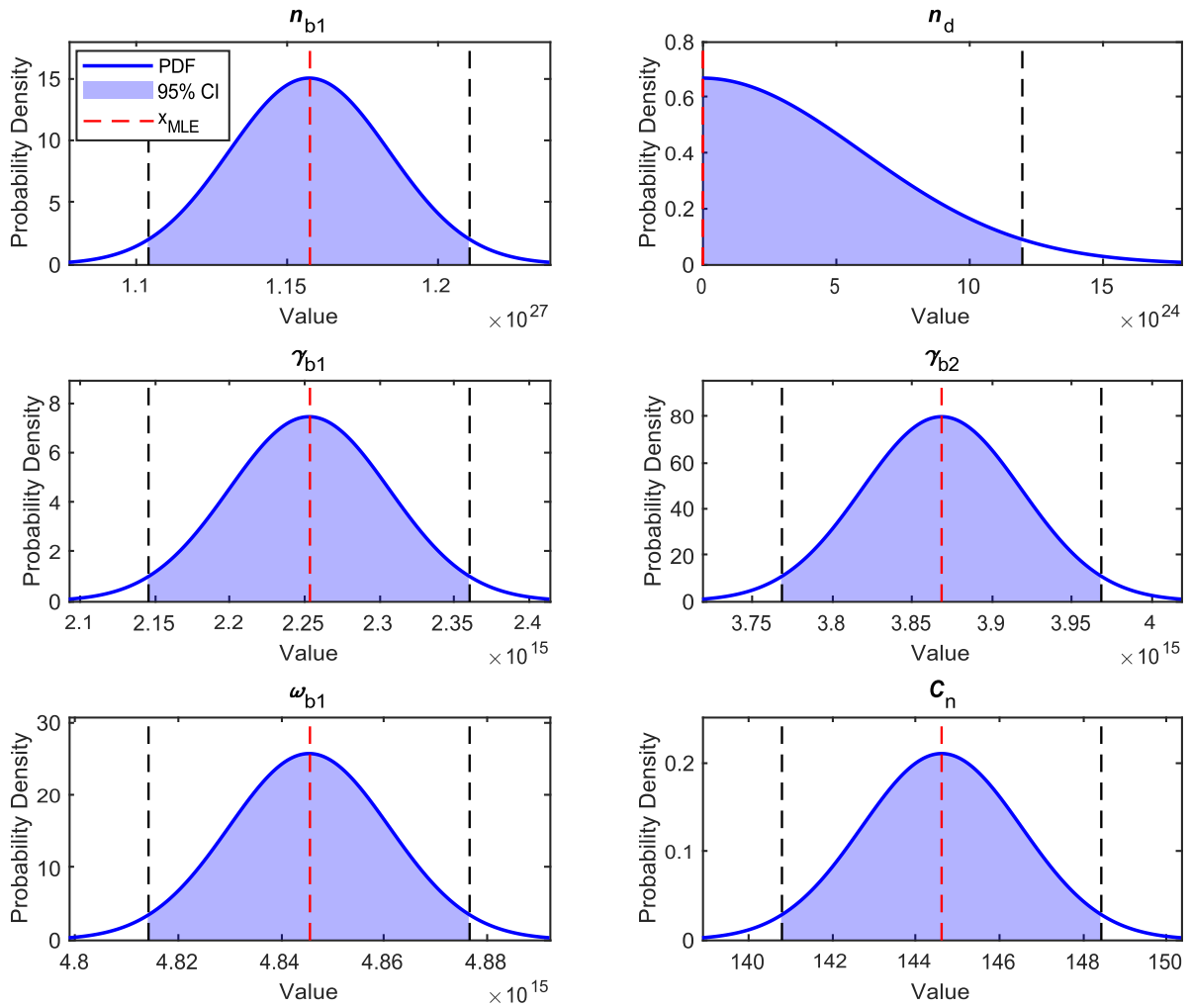


Figure 7-8: Normal distribution of the six fitted parameters with a 95% credibility interval - GO (0 min reduction duration)

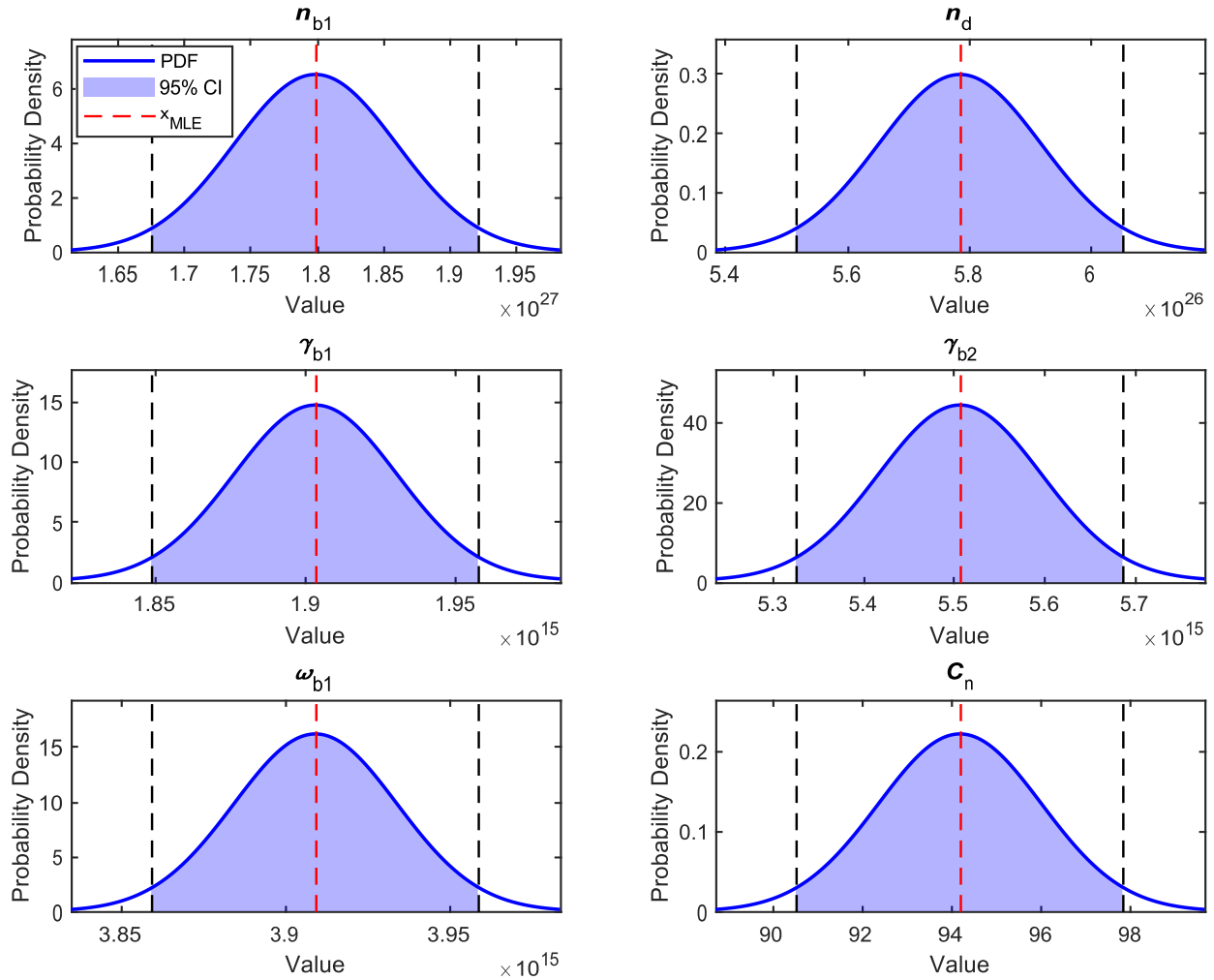


Figure 7-9: Normal distribution of the six fitted parameters with a 95% credibility interval - rGO (60 min reduction duration)

To derive the electrical conductivity as a function of wavelength with the associated error, 100 samples will be taken from the 95% CI interval. With these 100 samples and the x_{MLE} , $\sigma_{\lambda,e}$ can be derived via Eq. (3.42). Figure 7-10 shows an example of the electrical conductivity for rGO (60 min) from $0.2 \mu\text{m}$ to $6 \mu\text{m}$, with the gray lines representing $\sigma_{\lambda,e}$ derived from the 100 generated samples and the solid yellow line representing $\sigma_{\lambda,e}$ derived from x_{MLE} . This characteristic matches well with Hagens-Ruben relation, where, as the wavelength becomes increasingly large, the electrical conductivity converges to a constant DC conductivity (σ_{DC}). This is an important parameter as the DC conductivity is much more easily measured; consequently, the DC conductivity was calculated.

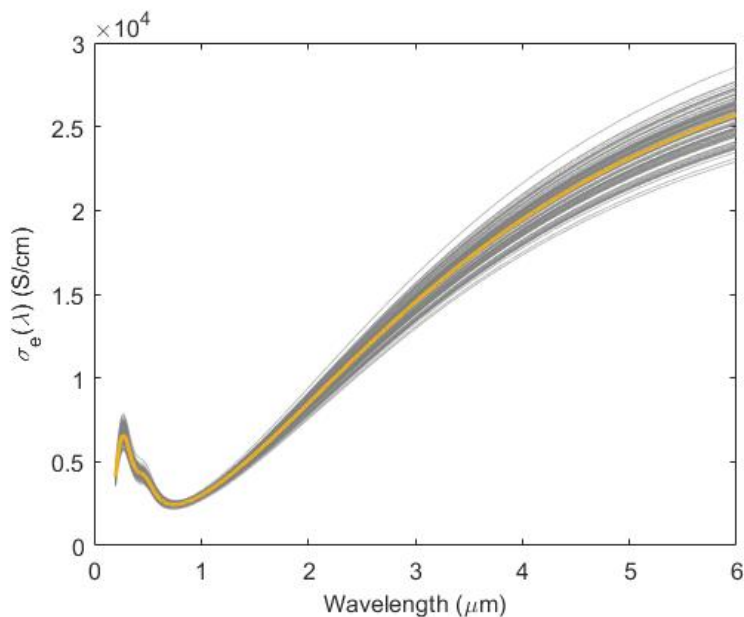


Figure 7-10: Spectral electrical conductivity for rGO (60 min reduction duration)

The DC conductivity was computed for all samples except for GO (0 min) due to high variability. Vertical error bars were determined by finding the standard deviation of the 100 randomly sampled points taken from the 95% credibility interval. Figure 7-11 shows the DC conductivity versus reduction duration. The converging trend aligns well with the absorbance characteristics of the GO samples and with the plot presented by Li et al. [140], as it is expected that initially, oxygen functional groups are rapidly removed from the material recovering the graphitic structure. As the reaction progresses, this process is expected to slow down until 60 minutes, at which the oxygen content of the GO is expected to remain relatively constant.

In the literature, the DC conductivity reported is typically a macroscopic conductivity derived using two-point and four-point probe techniques [150,163]. Macroscopic conductivity refers to a spatially averaged value determined for a film, rather than for a single particle. This method captures bulk properties of the film, such as arrangement of the particles within the film, but does not provide insight on the microscopic features of the particle, such as defects. To elucidate these effects, the electrical conductivity of a single particle is required. The DC conductivity of a single particle can be

experimentally derived via atomic force microscopy (AFM) techniques [164,165]; however, this process is ex-situ, time-consuming, and requires high precision. On the other hand, the Lorentz-Drude model used in this work enables rapid, real-time estimation of the electrical conductivity of a single particle by deriving the complex dielectric function for single particles. In a study conducted by Yan et al. [165], the electrical conductivity of thermally reduced rGO was found to be in the range of $0.5 - 3.7 \times 10^5$ S/m using Kelvin Probe AFM. The lower end of this range agrees well with the electrical conductivity obtained using the Lorentz-Drude model ($\sim 10^4$ S/m), supporting the validity of this approach for assessing single particle electrical conductivity through LOSA and the Lorentz-Drude model.

However, the absolute value may be inaccurate due to simplifying assumptions made in the model. By fixing values that may not fully describe the characteristics of GO/rGO, a higher mobile electron density may have been determined by the solver to account for the difference between modelled and real values. Additionally, unknown physical factors may influence the spectral absorbance, and a more complex Drude model could potentially resolve these discrepancies. Furthermore, due to the limited wavelength range, the Drude oscillator may not be properly captured, as this oscillator primarily affects broadband absorption. Future work should focus on fitting a larger wavelength range, defining more accurate fixed values, and/or exploring more complex Drude models to derive a more accurate DC conductivity. Nevertheless, the observed trend and magnitude of the DC conductivity are well represented, demonstrating the potential of the Lorentz-Drude model as a tool for deriving and comparing the conductivity of rGO samples.

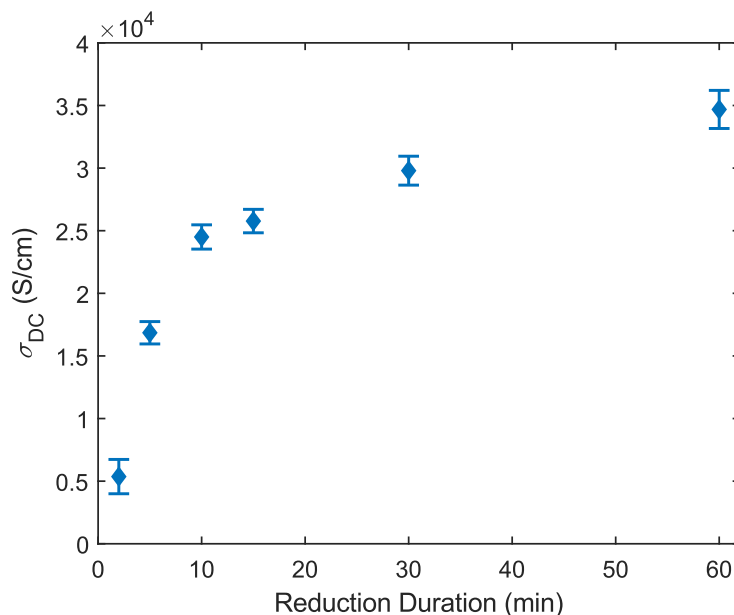


Figure 7-11: DC conductivity versus reduction duration

7.3 Summary

This chapter assessed the applicability of extinction-based measurements to derive the conductivity of GO/rGO particles. A study was conducted using a plasma reactor/LOSA apparatus to validate whether extinction measurements of GO and rGO could be derived in real-time. For the current apparatus, it was found that GO did not absorb light over the detection wavelengths considered here, whereas rGO did. However, it is noted GO primarily absorbs light at UV wavelengths due to the resonant frequencies in this region. This was not captured in this study due to the range of the spectrometer/EMCCD used. It is expected that LOSA is still applicable for GO; however, a wider wavelength range is necessary to record signals from its resonant frequencies. For rGO, the extinction data matched results from the literature, verifying the suitability of using LOSA to measure rGO. However, in this study the magnitude of absorbance was low, likely due to the low concentration of rGO within the measurement probe volume. Additionally, a lack of measurements at the UV wavelengths make it difficult to derive functional

characteristics of rGO. Therefore, for future experiments, a higher column density can be employed alongside measurements at UV wavelengths to improve the results.

To validate the applicability of extinction measurements for rGO, a study was run using a UV-Vis spectrometer to derive spectral absorbance plots from 210 nm to 550 nm at different degrees of reduction. The spectral absorbance was then used to derive parameters for the dielectric function and, subsequently, the DC conductivity, using the Lorentz-Drude model. Assuming two Lorentz oscillators and a single Drude oscillator, a good degree of fit was determined between the model and experimental data. The maximum likelihood estimates derived from the fit were then used to obtain the DC conductivity of the studied material. It was found that as the samples were reduced for longer periods of time, the DC conductivity increased, converging after 60 minutes of reduction. This aligns well with the expected trends, as the oxygen functional groups are expected to be removed quickly during the start of the reduction, then plateau after a long time period. However, the magnitude of the derived DC conductivity was higher than reported literature results. This is hypothesized to be a result of model inaccuracy and a narrow-studied wavelength range. This can be improved by measuring a wider range of wavelengths, defining more material accurate constants, and considering more complex models. Nonetheless, due to the good degree of fit and DC conductivity trends aligning well with literature results, it was concluded that the Lorentz-Drude model can be used to derive the electrical conductivity from spectral absorbance plots.

Based on the conclusion of the two studies, it can be determined that LOSA and the Lorentz-Drude model can be used in conjunction to provide real-time measurements of the electrical conductivity of GO and rGO.

Chapter 8

Conclusion and Future work

Thermal reduction of reduced graphene oxide (rGO) is a promising method of synthesis with high potential for large-scale industrial production. To realize this, *in situ*/online diagnostics are needed to provide real-time measurements of the characteristics of graphene oxide (GO) and rGO to assist in modifying the reduction parameters and to determine the properties of the synthesized material. This thesis assessed the applicability of absorption-based measurements, specifically time-resolved laser-induced incandescence (TiRe-LII) and line-of-sight attenuation (LOSA), in deriving characteristics of GO and rGO. This chapter summarizes and concludes key point from the studies conducted in this work and discusses future work that can investigated.

8.1 Summary and conclusions

This work was motivated by the need for real-time diagnostics of graphene oxide (GO) and reduced graphene oxide (rGO) during tube furnace thermal reduction. Chapter 1 reviewed the literature and demonstrated that absorption-based techniques are widely used to measure various nanomaterials in real-time, such as soot and metals. The two absorption-based techniques that showed the most promise were time-resolved laser-induced incandescence (TiRe-LII) and line-of-sight attenuation (LOSA). Time-resolved laser-induced incandescence is the standard process used to determine size distributions and volume fraction of soot particles [41–45] and has shown success in measuring metals [50–55], carbon nanotubes [56,57], and few-layer graphene [58,59]. Additionally, LOSA is widely used in the combustion community to derive real-time measurements of particle composition [66,67]. Consequently, both TiRe-LII and LOSA showed promise for *in situ* characterization of GO and rGO.

The goal of this thesis was to assess the viability of using TiRe-LII and LOSA to measure the characteristics of GO and rGO in real-time. The details of the measurement models used in this study

were discussed in Chapter 2, which included the heat transfer model used in TiRe-LII, the model to study spectrally resolved LOSA, and the Lorentz-Drude model. Chapter 3 covered the synthesis methods for GO and rGO, which included a two-step process: oxidizing graphite through the improved Hummer's method followed by spray-drying to form GO powder. The powder was then reduced using a tube furnace to form rGO. Additionally, a description of the excitation and detection system of TiRe-LII apparatus, as well as the design of the plasma reactor-LOSA apparatus, was presented. *Ex situ* characterization techniques employed to measure the optical and morphological properties of GO were discussed in Chapter 4.

Chapter 5 discussed the results obtained from the *ex situ* characterization. It was found that GO had a constant effective density of 0.93 g/cm^3 and a fractal dimension of 2.97. This indicated that the GO studied has a highly crumpled morphology with voids, as shown by the effective density being lower than the material densities presented in the literature [110,111]. Additionally, GO was found to have inferior absorption characteristics, with a low mass absorption cross-section (MAC) of 0.7 to $1.25 \text{ m}^2/\text{g}$ across a wide range of sizes. Instead, GO exhibited good scattering characteristics due to its much higher mass scattering cross-section (MSC), ranging from $1.75 - 7.5 \text{ m}^2/\text{g}$. This indicated that absorption-based techniques, such as TiRe-LII, would not be suitable for GO. This conclusion was reinforced by experiments conducted using a commercial LII device (LII 300) and the TiRe-LII apparatus presented in Chapter 3. No incandescent signals were recorded by GO; however, rGO showed clear incandescent signals, thus being the focus of the next chapter.

In Chapter 6, the tube furnace reduction apparatus present in Section 3.1.2 was connected to the four-colour TiRe-LII apparatus detailed in Section 3.2. Graphene oxide powder was aerosolized and directed into the tube furnace to be reduced at different reduction temperatures. Downstream of the tube furnace, the TiRe-LII apparatus was connected to measure the incandescent signals produced. From these signals, the specific surface area (SSA) of the produced rGO was measured. The derived SSA was found

to match well with results presented in the literature [36,150]. The magnitude was comparable, and the trends aligned well with the SSA increasing alongside the reduction temperature until a critical temperature was reached, after which the SSA dropped due to the formation of structural defects and refolding. The strong degree of fit demonstrates that the SSA of rGO at different degrees of reduction can be derived from TiRe-LII. Additionally, BET-SSA measurements yielded SSA values that aligned with TiRe-LII results. The magnitude and trends closely matched, with slight differences attributed to experimental noise, which led to model error, as well as assumptions made for the thermal accommodation coefficient (α_T) and specific heat capacity (c_p). Therefore, investigating α_T and c_p for rGO at different reduction temperatures, along with potential model error, would be beneficial for deriving absolute SSA values.

Chapter 7 presented a final study conducted to determine the feasibility of using LOSA and the Lorentz-Drude model to derive the electrical conductivity of GO/rGO particles in real time. It was determined that, due to the wavelength range of the spectrometer/EMCCD used for LOSA measurements (350 nm to 560 nm), GO did not provide any extinction signals. On the other hand, rGO generated signals that matched prior extinction measurements conducted in the literature via UV-Vis spectroscopy using a colloidal sample [140]. Nonetheless, due to the limited wavelength range key characteristics of the rGO extinction spectrum were missing. It was concluded that LOSA is viable for GO and rGO measurements; however, the wavelength range should include the UV region, and the column density should be higher to improve the signals derived.

Additionally, to assess whether the Lorentz-Drude model could derive the electrical conductivity from the extinction measurements, UV-vis spectroscopy on colloidal samples of GO and rGO were carried out to provide absorbance data in the UV region. Graphene oxide was chemically reduced using hydrazine and measured at different reduction durations. The spectral absorbance was then fitted against the Lorentz-Drude model to derive the dielectric constants. It was found that with two Lorentz oscillators

and a single Drude oscillator, the characteristics of the absorbance plot could be well described. Using the derived maximum likelihood estimates, the DC conductivity was computed over the reduction durations. It was found that the DC conductivity increase with the reaction time, with a sharp initial increase, followed by the conductivity converging at 60 minutes. This matched well with literature results, as it has been reported that the reaction initially reduces the oxygen content significantly, restoring much of the graphitic structure, before eventually reaching a point where no other oxygen functional groups can be removed [140]. However, the magnitude of the DC conductivity was found to be higher than results presented in the literature. This is attributed to incorrect assumptions made to simplify and constrain the model, as well as model error due to unknown physics. Nonetheless, the good degree of fit between the model and experimental data, along with the trend of the DC conductivity aligning with literature results, demonstrates the applicability of the Lorentz-Drude model to derive electrical conductivity from spectral extinction measurements.

From the conclusions derived in this study, a schematic of a potential *in situ* and online diagnostic set-up is presented in Figure 8-1. Line-of-sight attenuation can be used to derive the electrical conductivity of the GO prior to, and after reduction. This will provide an understanding of the degree of reduction along with a relative DC conductivity of the synthesized rGO. Additionally, TiRe-LII measurements can provide a good estimate of the SSA, offering information on the morphology and degree of reduction. If improved, LOSA can provide the absolute DC conductivity and TiRe-LII can provide the absolute SSA, which would offer functional information about the particle in real-time.

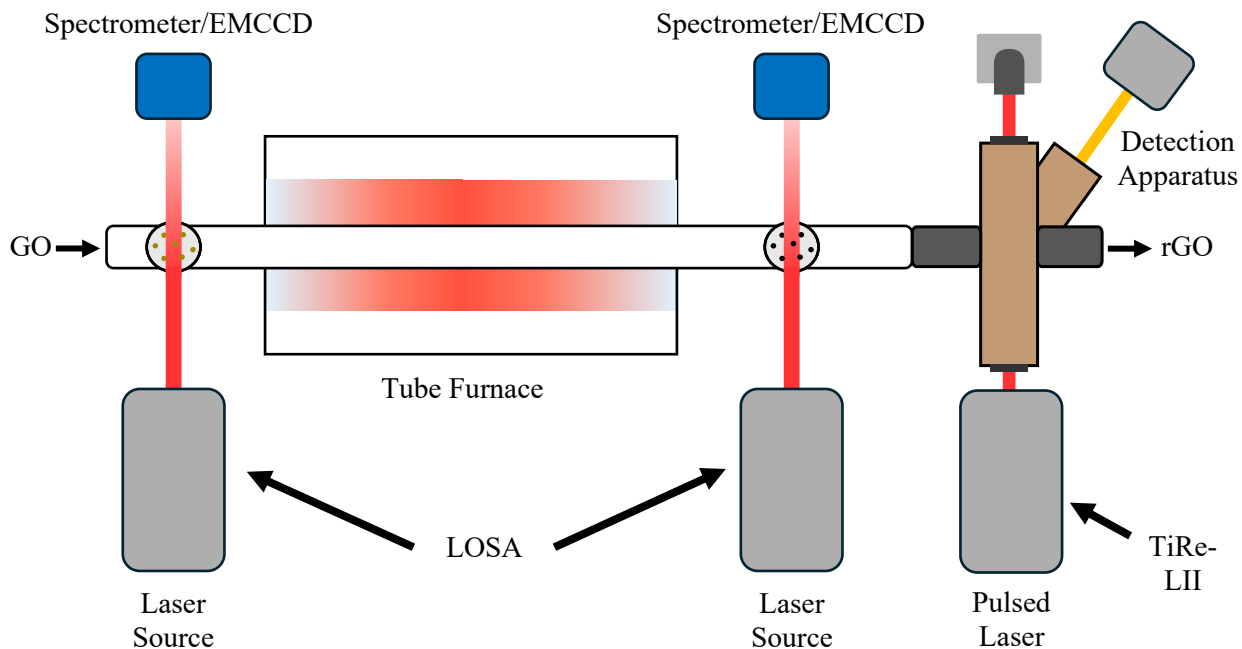


Figure 8-1: Schematic of in situ and online diagnostics of rGO synthesis

8.2 Future Work

The suggested directions for future work are categorized into improvements that can be made for TiRe-LII, and LOSA characterization methods and for additional optical diagnostics that may be applied to characterize this material.

8.2.1 TiRe-LII improvements

To improve the TiRe-LII diagnostic, three avenues of study can be employed: identifying whether a transition regime model is more appropriate, characterizing the thermal accommodation coefficient (α_T) and specific heat capacity (c_p) of rGO, and exploring the possibility of deriving volume fraction using the spectroscopic model.

As mentioned in the study, the Knudsen number was found to be 0.35, placing it on the boundary between the transition regime and the free-molecular regime. As an initial approach, the free-molecular

regime model appeared to work well for deriving the SSA; however, the transition regime model should be investigated, as it may provide a more accurate SSA. Additionally, to derive a reliable, absolute SSA, α_T and c_p should be measured for reduced graphene oxide at different reduction temperatures. While it may not be feasible to establish a universal set of constants due to the dependence of rGO properties on oxygen functional groups and defect concentration, a rough estimate would likely provide better agreement than assuming constant properties taken from soot and graphite.

Finally, another common application of TiRe-LII is deriving the volume fraction [43,166,167] using the spectroscopic model [73]. This would require the absolute calibration of the optical system, and an understanding of the general size of the particles formed, making it difficult to implement. Nonetheless, if volume fraction is desired, TiRe-LII is a strong candidate and should be considered.

8.2.2 LOSA improvements

As discussed in Chapter 7, there are improvements that can be made for both the LOSA measurement apparatus and the Lorentz-Drude model. The current LOSA apparatus only measures wavelengths between 330 nm to 560 nm; consequently, the peak in absorption around 250 nm for both GO and rGO is not captured, reducing the information provided by the spectrum. This limitation also prevents sufficient data from being provided to apply the Lorentz-Drude model. Therefore, further experiments should be run with a spectrometer/EMCCD that can measure in the UV region. Additionally, the magnitude of absorbance was low, likely due to the column density being too low. To increase the absorbance, the column density should be increased by increasing the concentration of particles within the probe volume.

Additionally, to improve the Lorentz-Drude fit, investigations should be made to derive more appropriate fixed values. This can be done through density functional theory (DFT) calculations [159], and *ex situ* measurements, such as spectroscopic ellipsometry [141,160]. Furthermore, model error should be characterized and accounted for. New models, such as the Drude-Smith model [161] or the enhanced Drude model [162], can be considered to address and account for unknown or unresolved physics.

Additional experiments can also be conducted at wider wavelength ranges to determine whether the inflection found at 550 nm is caused by impurities in the sample or unknown physics. These improvements will help derive a more accurate DC conductivity. *Ex situ* experiments, such as a two- or four-point probe method [28,150,163], can be conducted on the synthesized rGO to obtain the real DC conductivity and assess the degree of error between the real and derived DC conductivity from the Lorentz-Drude model.

8.2.3 Additional diagnostics

To further characterize the GO and rGO, additional diagnostic methods can be investigated. One in particular that shows promise is elastic light scattering (ELS). From the *ex situ* studies carried out in Chapter 5, it was determined that GO exhibits stronger scattering characteristics than absorption. This makes ELS a potentially viable diagnostic for GO, and potentially rGO. Yazici et al. has shown through discrete dipole approximation (DDA) simulations that morphological characteristics can be derived from angled ELS studies [168]. Additionally, experiments have been carried out using a wide-angle light scattering (WALS) apparatus on soot, demonstrating the potential of WALS to be used to measure GO and rGO particles [169].

8.3 Impact

This work has derived a general framework that can be used to obtain information on the specific surface area (SSA), electrical conductivity, morphology, and degree of reduction of the synthesized rGO in real-time. Additionally, the optical diagnostics presented in this study can assist in sensitivity experiments, where tube furnace parameters can be studied and modified in real-time to determine how furnace parameters affect the characteristics of the final product. The *ex-situ* optical characterization of GO also demonstrates that other optical diagnostic tools, such as elastic light scattering, may be suitable to provide additional information. Further development of these systems, in conjunction with the tube furnace

reduction apparatus, will enable the creation of a high yield rGO synthesis process that can produce well-defined rGO material for a wide variety of applications.

References

- [1] Novoselov KS, Geim AK, Morozov S V., Jiang D, Zhang Y, Dubonos S V., et al. Electric field in atomically thin carbon films. *Science* (1979) 2004;306:666–9. <https://doi.org/10.1126/science.1102896>.
- [2] Ji L, Meduri P, Agubra V, Xiao X, Alcoutlabi M. Graphene-Based Nanocomposites for Energy Storage. *Adv Energy Mater* 2016;6. <https://doi.org/10.1002/aenm.201502159>.
- [3] Karthick R, Chen F. Free-standing graphene paper for energy application: Progress and future scenarios. *Carbon N Y* 2019;150:292–310. <https://doi.org/10.1016/j.carbon.2019.05.017>.
- [4] Chung C, Kim YK, Shin D, Ryoo SR, Hong BH, Min DH. Biomedical applications of graphene and graphene oxide. *Acc Chem Res* 2013;46:2211–24. <https://doi.org/10.1021/ar300159f>.
- [5] Wang J, Jin X, Li C, Wang W, Wu H, Guo S. Graphene and graphene derivatives toughening polymers: Toward high toughness and strength. *Chemical Engineering Journal* 2019;370:831–54. <https://doi.org/10.1016/j.cej.2019.03.229>.
- [6] Nguyen Bich H, Nguyen Van H. Promising applications of graphene and graphene-based nanostructures. *Advances in Natural Sciences: Nanoscience and Nanotechnology* 2016;7. <https://doi.org/10.1088/2043-6262/7/2/023002>.
- [7] Du W, Geng H, Yang Y, Zhang Y, Rui X, Li CC. Pristine graphene for advanced electrochemical energy applications. *J Power Sources* 2019;437. <https://doi.org/10.1016/j.jpowsour.2019.226899>.
- [8] Abbas Q, Shinde PA, Abdelkareem MA, Alami AH, Mirzaeian M, Yadav A, et al. Graphene Synthesis Techniques and Environmental Applications. *Materials* 2022;15. <https://doi.org/10.3390/ma15217804>.
- [9] Shao G, Lu Y, Wu F, Yang C, Zeng F, Wu Q. Graphene oxide: The mechanisms of oxidation and exfoliation. *J Mater Sci* 2012;47:4400–9. <https://doi.org/10.1007/s10853-012-6294-5>.
- [10] Lee S, Eom SH, Chung JS, Hur SH. Large-scale production of high-quality reduced graphene oxide. *Chemical Engineering Journal* 2013;233:297–304. <https://doi.org/10.1016/j.cej.2013.08.050>.
- [11] Alam SN, Sharma N, Kumar L. Synthesis of Graphene Oxide (GO) by Modified Hummers Method and Its Thermal Reduction to Obtain Reduced Graphene Oxide (rGO)*. *Graphene* 2017;06:1–18. <https://doi.org/10.4236/graphene.2017.61001>.
- [12] Liu C, Hu G. Highly efficient reduction of graphene oxide by sub/supercritical water and their application for thermal interface materials. *Appl Therm Eng* 2015;90:193–8. <https://doi.org/10.1016/j.applthermaleng.2015.07.011>.
- [13] El Rouby WMA. Crumpled graphene: preparation and applications. *RSC Adv* 2015;5:66767–96. <https://doi.org/10.1039/c5ra10289h>.
- [14] Luo J, Jang HD, Sun T, Xiao L, He Z, Katsoulidis AP, et al. Compression and aggregation-resistant particles of crumpled soft sheets. *ACS Nano* 2011;5:8943–9. <https://doi.org/10.1021/nn203115u>.
- [15] Ma X, Zachariah MR, Zangmeister CD. Reduction of suspended graphene oxide single sheet nanopaper: The effect of crumpling. *Journal of Physical Chemistry C* 2013;117:3185–91. <https://doi.org/10.1021/jp400237m>.

- [16] Ray SC. Application and Uses of Graphene Oxide and Reduced Graphene Oxide. Applications of Graphene and Graphene-Oxide Based Nanomaterials, Elsevier; 2015, p. 39–55. <https://doi.org/10.1016/b978-0-323-37521-4.00002-9>.
- [17] Michelsen HA, Schulz C, Smallwood GJ, Will S. Laser-induced incandescence: Particulate diagnostics for combustion, atmospheric, and industrial applications. *Prog Energy Combust Sci* 2015;51:2–48. <https://doi.org/10.1016/j.pecs.2015.07.001>.
- [18] Migliorini F, Thomson KA, Smallwood GJ. Investigation of optical properties of aging soot. *Appl Phys B*, vol. 104, 2011, p. 273–83. <https://doi.org/10.1007/s00340-011-4396-4>.
- [19] Twynstra MG, Daun KJ, Waslander SL. Line-of-sight-attenuation chemical species tomography through the level set method. *J Quant Spectrosc Radiat Transf* 2014;143:25–34. <https://doi.org/10.1016/j.jqsrt.2013.09.015>.
- [20] Brodie B. Xiii. On the atomic weight of graphite. *Philos Trans R Soc Lond* 1859;149:249–59.
- [21] Staudenmaier L. Verfahren zur Darstellung der Graphitsäure. *Berichte Der Deutschen Chemischen Gesellschaft* 1898;31:1481–99.
- [22] Hummers WS, Offeman RE. Preparation of Graphitic Oxide. *J Am Chem Soc* 1958;80:1339–1339. <https://doi.org/10.1021/ja01539a017>.
- [23] Marcano DC, Kosynkin D V., Berlin JM, Sinitskii A, Sun Z, Slesarev A, et al. Improved synthesis of graphene oxide. *ACS Nano* 2010;4:4806–14. <https://doi.org/10.1021/nn1006368>.
- [24] Yu H, Zhang B, Bulin C, Li R, Xing R. High-efficient Synthesis of Graphene Oxide Based on Improved Hummers Method. *Sci Rep* 2016;6. <https://doi.org/10.1038/srep36143>.
- [25] Boehm HP, Clauss A, Hofmann U. Graphite Oxide and Its Membrane Properties. *J Chim Phys Physicochim Biol* 1961;58:141–7.
- [26] Titelman GI, Gelman V, Bron S, Khalfin RL, Cohen Y, Bianco-Peled H. Characteristics and microstructure of aqueous colloidal dispersions of graphite oxide. *Carbon N Y* 2005;43:641–9. <https://doi.org/10.1016/j.carbon.2004.10.035>.
- [27] Stankovich S, Dikin DA, Dommett GHB, Kohlhaas KM, Zimney EJ, Stach EA, et al. Graphene-based composite materials. *Nature* 2006;442:282–6. <https://doi.org/10.1038/nature04969>.
- [28] Stankovich S, Dikin DA, Piner RD, Kohlhaas KA, Kleinhammes A, Jia Y, et al. Synthesis of graphene-based nanosheets via chemical reduction of exfoliated graphite oxide. *Carbon N Y* 2007;45:1558–65. <https://doi.org/10.1016/j.carbon.2007.02.034>.
- [29] Guoxiu W, Juan Y, Jinsoo P, Xinglong G, Bei W, Hao L, et al. Facile synthesis and characterization of graphene nanosheets. *Journal of Physical Chemistry C* 2008;112:8192–5. <https://doi.org/10.1021/jp710931h>.
- [30] Fan X, Peng W, Li Y, Li X, Wang S, Zhang G, et al. Deoxygenation of exfoliated graphite oxide under alkaline conditions: a green route to graphene preparation. *Advanced Materials* 2008;20:4490–3. <https://doi.org/10.1002/adma.200801306>.
- [31] Shin HJ, Kim KK, Benayad A, Yoon SM, Park HK, Jung IS, et al. Efficient reduction of graphite oxide by sodium borohydride and its effect on electrical conductance. *Adv Funct Mater* 2009;19:1987–92. <https://doi.org/10.1002/adfm.200900167>.

- [32] Dreyer DR, Park S, Bielawski CW, Ruoff RS. The chemistry of graphene oxide. *Chem Soc Rev* 2010;39:228–40. <https://doi.org/10.1039/b917103g>.
- [33] Agarwal V, Zetterlund PB. Strategies for reduction of graphene oxide – A comprehensive review. *Chemical Engineering Journal* 2021;405. <https://doi.org/10.1016/j.cej.2020.127018>.
- [34] Zhou M, Wang Y, Zhai Y, Zhai J, Ren W, Wang F, et al. Controlled synthesis of large-area and patterned electrochemically reduced graphene oxide films. *Chemistry - A European Journal* 2009;15:6116–20. <https://doi.org/10.1002/chem.200900596>.
- [35] Schniepp HC, Li JL, McAllister MJ, Sai H, Herrera-Alonson M, Adamson DH, et al. Functionalized single graphene sheets derived from splitting graphite oxide. *Journal of Physical Chemistry B* 2006;110:8535–9. <https://doi.org/10.1021/jp060936f>.
- [36] Huh SH. Thermal Reduction of Graphene Oxide. *Physics and Applications of Graphene - Experiments*, IntechOpen; 2011. <https://doi.org/10.5772/14156>.
- [37] Sengupta I, Chakraborty S, Talukdar M, Pal SK, Chakraborty S. Thermal reduction of graphene oxide: How temperature influences purity. *J Mater Res* 2018;33:4113–22. <https://doi.org/10.1557/jmr.2018.338>.
- [38] Weeks RW, Duley WW. Aerosol-particle sizes from light emission during excitation by TEA CO₂ laser pulses. *J Appl Phys* 1974;45:4661–2. <https://doi.org/10.1063/1.1663111>.
- [39] Eckbreth AC. Effects of laser-modulated particulate incandescence on Raman scattering diagnostics. *J Appl Phys* 1977;48:4473–9. <https://doi.org/10.1063/1.323458>.
- [40] Melton LA. Soot diagnostics based on laser heating. *Appl Opt* 1984;23:2201–8. <https://doi.org/10.1364/AO.23.002201>.
- [41] Schulz C, Kock BF, Hofmann M, Michelsen H, Will S, Bougie B, et al. Laser-induced incandescence: Recent trends and current questions. *Appl Phys B* 2006;83:333–54. <https://doi.org/10.1007/s00340-006-2260-8>.
- [42] Snelling DR, Thomson KA, Smallwood GJ, Gülder ÖL. Two-dimensional imaging of soot volume fraction in laminar diffusion flames. *Appl Opt* 1999;38:2478–85. <https://doi.org/10.1364/AO.38.002478>.
- [43] Snelling DR, Thomson KA, Smallwood GJ, Gülder L, Weckman EJ, Fraser RA. Spectrally resolved measurement of flame radiation to determine soot temperature and concentration. *AIAA Journal* 2002;40:1789–95. <https://doi.org/10.2514/2.1855>.
- [44] Snelling DR, Liu F, Smallwood GJ, Gülder ÖL. Determination of the soot absorption function and thermal accommodation coefficient using low-fluence LII in a laminar coflow ethylene diffusion flame. *Combust Flame* 2004;136:180–90. <https://doi.org/10.1016/j.combustflame.2003.09.013>.
- [45] Michelsen HA, Liu F, Kock BF, Bladh H, Boiarciuc A, Charwath M, et al. Modeling laser-induced incandescence of soot: A summary and comparison of LII models. *Appl Phys B* 2007;87:503–21. <https://doi.org/10.1007/s00340-007-2619-5>.
- [46] Stephens M, Turner N, Sandberg J. Particle identification by laser-induced incandescence in a solid-state laser cavity. *Appl Opt* 2003;42:3726–36.
- [47] Kock BF, Schulz C, Roth P. Time-resolved laser-induced incandescence applied to in-cylinder Diesel particle sizing. *International Bunsen Discussion Meeting: Laser-Induced Incandescence*,

Quantitative interpretation, modelling, application, Duisburg, Germany: CEUR Workshop Proceedings; 2005.

- [48] Will S, Schraml S, Leipertz A. Two-dimensional soot-particle sizing by time-resolved laser-induced incandescence. *Optical Letters* 1995;20:2342–4. <https://doi.org/10.1364/OL.20.002342>.
- [49] Woiki D, Giesen A, Roth P. Time-resolved laser-induced incandescence for soot particle sizing during acetylene pyrolysis behind shock waves. *Proceedings of the Combustion Institute* 2000;28:2531–7. [https://doi.org/10.1016/S0082-0784\(00\)80669-4](https://doi.org/10.1016/S0082-0784(00)80669-4).
- [50] Sipkens TA, Menser J, Dreier T, Schulz C, Smallwood GJ, Daun KJ. Laser-induced incandescence for non-soot nanoparticles: recent trends and current challenges. *Appl Phys B* 2022;128. <https://doi.org/10.1007/s00340-022-07769-z>.
- [51] Vander Wal RL, Ticich TM, West JR. Laser-induced incandescence applied to metal nanostructures 1999;38:5867–79. <https://doi.org/10.1364/AO.38.005867>.
- [52] Filippov A V, Markus MW, Roth P. In-situ characterization of ultrafine particles by laser-induced incandescence: sizing and particle structure determination. *Journal Aerosol Sci* 1999;30:71–87. [https://doi.org/10.1016/S0021-8502\(98\)00021-4](https://doi.org/10.1016/S0021-8502(98)00021-4).
- [53] Robinson-Enebeli S, Schulz C, Daun KJ. Investigating the absorption properties of metal nanoparticle aggregates during time-resolved laser-induced incandescence. *J Quant Spectrosc Radiat Transf* 2024;322. <https://doi.org/10.1016/j.jqsrt.2024.109009>.
- [54] De Iuliis S, Migliorini F, Dondè R. Laser-induced emission of TiO₂ nanoparticles in flame spray synthesis. *Appl Phys B* 2019;125. <https://doi.org/10.1007/s00340-019-7324-7>.
- [55] Talebi Moghaddam S, Daun KJ. Plasma emission during time-resolved laser-induced incandescence measurements of aerosolized metal nanoparticles. *Appl Phys B* 2018;124. <https://doi.org/10.1007/s00340-018-7028-4>.
- [56] Vander Wal RL, Berger GM, Ticich TM, Patel PD. Application of laser-induced incandescence to the detection of carbon nanotubes and carbon nanofibers. *Appl Opt* 2002;41:5678–90. <https://doi.org/10.1364/AO.41.005678>.
- [57] Cau M, Dorval N, Attal-Trétout B, Cochon JL, Foutel-Richard A, Loiseau A, et al. Formation of carbon nanotubes: In situ optical analysis using laser-induced incandescence and laser-induced fluorescence. *Phys Rev B Condens Matter Mater Phys* 2010;81. <https://doi.org/10.1103/PhysRevB.81.165416>.
- [58] Musikhin S, Fortugno P, Corbin JC, Smallwood GJ, Dreier T, Daun KJ, et al. Characterization of few-layer graphene aerosols by laser-induced incandescence. *Carbon N Y* 2020;167:870–80. <https://doi.org/10.1016/j.carbon.2020.05.052>.
- [59] López-Cámara CF, Fortugno P, Asif M, Musikhin S, Prindler C, Wiggers H, et al. Evolution of particle size and morphology in plasma synthesis of few-layer graphene and soot. *Combust Flame* 2023. <https://doi.org/10.1016/j.combustflame.2023.112713>.
- [60] Howell JR, Pinar Mengüç M, Daun KJ. *Thermal Radiation: An Introduction*. 1st ed. Boca Raton: CRC Press; 2023.
- [61] Beer A. Bestimmung der Absorption des rothen Lichts in farbigen Flüssigkeiten. *Ann Phys* 1852;162:78–88.

- [62] Hottel HC, Broughton FP. Determination of True Temperature and Total Radiation from Luminous Gas Flames Use of Special Two-Color Optical Pyrometer. *Industrial & Engineering Chemistry Analytical Edition* 1932;4:157–246.
- [63] Greenberg PS, Ku JC. Soot volume fraction imaging. *Appl Opt* 1997;36:5514–22. <https://doi.org/10.1364/AO.36.005514>.
- [64] Thomson KA, Johnson MR, Snelling DR, Smallwood GJ. Diffuse-light two-dimensional line-of-sight attenuation for soot concentration measurements. *Appl Opt* 2008;47:694–703. <https://doi.org/10.1364/AO.47.000694>.
- [65] Thomson KA, Johnson MR, Snelling DR, Smallwood GJ. One-Dimensional Spectral Line-of-Sight Attenuation for Soot Optical Property Measurement. 2008.
- [66] Liu G, Asif M, Menser J, Dreier T, Mohri K, Schulz C, et al. Spatial distribution of gas-phase synthesized germanium nanoparticle volume-fraction and temperature using combined in situ line-of-sight emission and extinction spectroscopy. *Opt Express* 2021;29:8387. <https://doi.org/10.1364/oe.418922>.
- [67] Asif M, Menser J, Endres T, Dreier T, Daun K, Schulz C. Phase-sensitive detection of gas-borne Si nanoparticles via line-of-sight UV/VIS attenuation. *Opt Express* 2021;29:21795. <https://doi.org/10.1364/oe.426528>.
- [68] Ma X, Zachariah MR, Zangmeister CD. Crumpled nanopaper from graphene oxide. *Nano Lett* 2012;12:486–9. <https://doi.org/10.1021/nl203964z>.
- [69] Talebi-Moghaddam S, Sipkens TA, Daun KJ. Laser-induced incandescence on metal nanoparticles: validity of the Rayleigh approximation. *Appl Phys B* 2019;125. <https://doi.org/10.1007/s00340-019-7325-6>.
- [70] Polyakov S V. Photomultiplier Tubes. *Experimental Methods in the Physical Sciences*, vol. 45, Academic Press; 2013, p. 69–82. <https://doi.org/10.1016/B978-0-12-387695-9.00003-2>.
- [71] Daun KJ, Smallwood GJ, Liu F. Investigation of thermal accommodation coefficients in time-resolved laser-induced incandescence. *J Heat Transfer* 2008;130:1–9. <https://doi.org/10.1115/1.2977549>.
- [72] Sipkens TA, Singh NR, Daun KJ. Time-resolved laser-induced incandescence characterization of metal nanoparticles. *Appl Phys B* 2017;123. <https://doi.org/10.1007/s00340-016-6593-7>.
- [73] Menser J, Daun K, Dreier T, Schulz C. Laser-induced incandescence from laser-heated silicon nanoparticles. *Appl Phys B* 2016;122. <https://doi.org/10.1007/s00340-016-6551-4>.
- [74] Robinson-Enebeli SC. Investigating laser-nanoparticle interactions using time-resolved laser-induced incandescence. 2020.
- [75] Liu F, Stagg BJ, Snelling DR, Smallwood GJ. Effects of primary soot particle size distribution on the temperature of soot particles heated by a nanosecond pulsed laser in an atmospheric laminar diffusion flame. *Int J Heat Mass Transf* 2006;49:777–88. <https://doi.org/10.1016/j.ijheatmasstransfer.2005.07.041>.
- [76] Bohren CF, Huffman DR. Absorption and scattering of light by small particles. Hoboken, NJ: John Wiley & sons; 1983.

- [77] Sorensen CM. Light scattering by fractal aggregates: A review. *Aerosol Science and Technology* 2001;35:648–87. <https://doi.org/10.1080/02786820117868>.
- [78] Daun KJ, Huberman SC. Influence of particle curvature on transition regime heat conduction from aerosolized nanoparticles. *Int J Heat Mass Transf* 2012;55:7668–76. <https://doi.org/10.1016/j.ijheatmasstransfer.2012.07.076>.
- [79] Liu F, Daun KJ, Snelling DR, Smallwood GJ. Heat conduction from a spherical nano-particle: Status of modeling heat conduction in laser-induced incandescence. *Appl Phys B* 2006;83:355–82. <https://doi.org/10.1007/s00340-006-2194-1>.
- [80] Daun KJ. Thermal accommodation coefficients between polyatomic gas molecules and soot in laser-induced incandescence experiments. *Int J Heat Mass Transf* 2009;52:5081–9. <https://doi.org/10.1016/j.ijheatmasstransfer.2009.05.006>.
- [81] Fuchs N. Über die Verdampfungsgeschwindigkeit kleiner Tröpfchen in einer Gasatmosphäre. *Phys Z Sowjet* 1934;6:225–43.
- [82] Kennard Earle H. *Kinetic Theory of Gases*. 1st ed. New York: McGraw-Hill; 1938.
- [83] Goodman FO, Wachman HY. *Dynamics of Gas-Surface Scattering*. 1st ed. New York: Academic Press; 1976.
- [84] Lehre T, Suntz R, Bockhorn H. Time-resolved two-color LII: Size distributions of nano-particles from gas-to-particle synthesis. *Proceedings of the Combustion Institute* 2005;30:2585–93. <https://doi.org/10.1016/j.proci.2004.08.113>.
- [85] Mohan VB, Jayaraman K, Bhattacharyya D. Brunauer–Emmett–Teller (BET) specific surface area analysis of different graphene materials: A comparison to their structural regularity and electrical properties. *Solid State Commun* 2020;320. <https://doi.org/10.1016/j.ssc.2020.114004>.
- [86] Stoller MD, Park S, Yanwu Z, An J, Ruoff RS. Graphene-Based ultracapacitors. *Nano Lett* 2008;8:3498–502. <https://doi.org/10.1021/nl802558y>.
- [87] Modest MF. *Radiative Heat Transfer*. 3rd ed. Academic Press; 2013.
- [88] She Z, Gad M, Ma Z, Li Y, Pope MA. Enhanced cycle stability of crumpled graphene-encapsulated silicon anodes via polydopamine sealing. *ACS Omega* 2021;6:12293–305. <https://doi.org/10.1021/acsomega.1c01227>.
- [89] Parviz D, Metzler SD, Das S, Irin F, Green MJ. Tailored crumpling and unfolding of spray-dried pristine graphene and graphene oxide sheets. *Small* 2015;11:2661–8. <https://doi.org/10.1002/smll.201403466>.
- [90] Carbolite. *Installation, Operation & Maintenance Instructions STF & TZF Models*. 2018.
- [91] Big Sky Laser Technologies Inc. *User’s Manual Ultra CFR Nd:YAG Laser Manual*. 1999 n.d.
- [92] Liu F, Rogak S, Snelling DR, Saffaripour M, Thomson KA, Smallwood GJ. Effects of laser fluence non-uniformity on ambient-temperature soot measurements using the auto-compensating laser-induced incandescence technique. *Appl Phys B* 2016;122. <https://doi.org/10.1007/s00340-016-6553-2>.
- [93] Polyakov S V., Migdall A, Fan J, Bienfang JC. Chapter 3 - Photomultiplier Tubes. *Experimental Methods in the Physical Sciences*, vol. 45, Academic Press; 2013, p. 69–82.

- [94] Mansmann R, Sipkens TA, Menser J, Daun KJ, Dreier T, Schulz C. Detector calibration and measurement issues in multi-color time-resolved laser-induced incandescence. *Appl Phys B* 2019;125. <https://doi.org/10.1007/s00340-019-7235-7>.
- [95] Mansmann R, Dreier T, Schulz C. Performance of photomultipliers in the context of laser-induced incandescence. *Appl Opt* 2017;56:7849. <https://doi.org/10.1364/ao.56.007849>.
- [96] Sipkens TA, Mansmann R, Daun KJ, Petermann N, Titantah JT, Karttunen M, et al. In situ nanoparticle size measurements of gas-borne silicon nanoparticles by time-resolved laser-induced incandescence. *Appl Phys B* 2014;116:623–36. <https://doi.org/10.1007/s00340-013-5745-2>.
- [97] Energetiq. Laser-Driven Light Source (LDLS®) Models: EQ-77 & EQ-77X Operation Manual. 2024.
- [98] Princeton Instruments. IsoPlane SCT 320 Manual. 2013.
- [99] Princeton Instruments. ProEM System Manual. 2009.
- [100] Paredes JI, Villar-Rodil S, Martínez-Alonso A, Tascón JMD. Graphene oxide dispersions in organic solvents. *Langmuir* 2008;24:10560–4. <https://doi.org/10.1021/la801744a>.
- [101] Laengert SE, Kwon YJ, Corbin JC, Sipkens TA, Morkus P, LaRue RJ, et al. Aerosol charge neutralization and its impact on particle filtration efficiency of common face mask materials. *J Aerosol Sci* 2023;173. <https://doi.org/10.1016/j.jaerosci.2023.106189>.
- [102] Perma Pure. PD - Series Gas Dryer User Manual. 2021.
- [103] Catalytic Instruments. Catalytic Stripper: Model CS015 Catalytic Stripper 2025.
- [104] Williams DB, Carter CB. Transmission Electron Microscope. *Transmission Electron Microscopy*, Boston, MA: Springer US; 1996, p. 3–17. https://doi.org/10.1007/978-1-4757-2519-3_1.
- [105] University of Waterloo. JEOL S/TEM operational and service now available. University of Waterloo 2023.
- [106] Sioutas C, Abt E, Wolfson JM, Koutrakis P. Evaluation of the Measurement Performance of the Scanning Mobility Particle Sizer and Aerodynamic Particle Sizer. *Aerosol Science and Technology* 1999;30:84–92. <https://doi.org/10.1080/027868299304903>.
- [107] TSI Inc. Particle Detectors FUNDAMENTALS OF CONDENSATION PARTICLE COUNTERS (CPC) AND SCANNING MOBILITY PARTICLE SIZER™ (SMPS™) SPECTROMETERS. 2014.
- [108] Trivanovic U, Sipkens TA, Kazemimanesh M, Baldelli A, Jefferson AM, Conrad BM, et al. Morphology and size of soot from gas flares as a function of fuel and water addition. *Fuel* 2020;279. <https://doi.org/10.1016/j.fuel.2020.118478>.
- [109] Sipkens TA, Boies A, Corbin JC, Chakrabarty RK, Olfert J, Rogak SN. Overview of methods to characterize the mass, size, and morphology of soot. *J Aerosol Sci* 2023;173. <https://doi.org/10.1016/j.jaerosci.2023.106211>.
- [110] Torrisi L, Cutroneo M, Torrisi A, Silipigni L. Measurements on Five Characterizing Properties of Graphene Oxide and Reduced Graphene Oxide Foils. *Physica Status Solidi (A) Applications and Materials Science* 2022;219:2100628. <https://doi.org/10.1002/pssa.202100628>.

- [111] Dikin DA, Stankovich S, Zimney EJ, Piner RD, Dommett GHB, Evmenenko G, et al. Preparation and characterization of graphene oxide paper. *Nature* 2007;448:457–60. <https://doi.org/10.1038/nature06016>.
- [112] Cambustion. CPMA Centrifugal Particle Mass Analyzer. n.d.
- [113] Perraud V, Smith JN, Olfert J. High-accuracy effective density measurements of sodium methanesulfonate and ammonium chloride nanoparticles using a particulate calibration standard. *Aerosol Science and Technology* 2023;57:355–66. <https://doi.org/10.1080/02786826.2023.2176739>.
- [114] Onasch TB, Massoli P, Keegan PL, Hills FB, Bacon FW, Freedman A. Single scattering albedo monitor for airborne particulates. *Aerosol Science and Technology* 2015;49:267–79. <https://doi.org/10.1080/02786826.2015.1022248>.
- [115] Modini RL, Corbin JC, Brem BT, Irwin M, Bertò M, Pileci RE, et al. Detailed characterization of the CAPS single-scattering albedo monitor (CAPS PMssa) as a field-deployable instrument for measuring aerosol light absorption with the extinction-minus-scattering method. *Atmos Meas Tech* 2021;14:819–51. <https://doi.org/10.5194/amt-14-819-2021>.
- [116] Drinovec L, Močnik G, Zotter P, Prévôt ASH, Ruckstuhl C, Coz E, et al. The “dual-spot” Aethalometer: An improved measurement of aerosol black carbon with real-time loading compensation. *Atmos Meas Tech* 2015;8:1965–79. <https://doi.org/10.5194/amt-8-1965-2015>.
- [117] Collaud Coen M, Weingartner E, Apituley A, Ceburnis D, Fierz-Schmidhauser R, Flentje H, et al. Atmospheric Measurement Techniques Minimizing light absorption measurement artifacts of the Aethalometer: evaluation of five correction algorithms. *Atmos Meas Tech* 2010;3:457–74. <https://doi.org/10.5194/amt-3-457-2010>.
- [118] Drinovec L, Jagodič U, Pirker L, Škarabot M, Kurtjak M, Vidović K, et al. A dual-wavelength photothermal aerosol absorption monitor: design, calibration and performance. *Atmos Meas Tech* 2022;15:3805–25. <https://doi.org/10.5194/amt-15-3805-2022>.
- [119] Corbin JC, Pieber SM, Czech H, Zanatta M, Jakobi G, Massabò D, et al. Brown and Black Carbon Emitted by a Marine Engine Operated on Heavy Fuel Oil and Distillate Fuels: Optical Properties, Size Distributions, and Emission Factors. *Journal of Geophysical Research: Atmospheres* 2018;123:6175–95. <https://doi.org/10.1029/2017JD027818>.
- [120] Yus-Díez J, Bernardoni V, Močnik G, Alastuey A, Ciniglia D, Ivančič M, et al. Determination of the multiple-scattering correction factor and its cross-sensitivity to scattering and wavelength dependence for different AE33 Aethalometer filter tapes: a multi-instrumental approach. *Atmos Meas Tech* 2021;14:6335–55. <https://doi.org/10.5194/amt-14-6335-2021>.
- [121] Liu C, Chung CE, Yin Y, Schnaiter M. The absorption Ångström exponent of black carbon: From numerical aspects. *Atmos Chem Phys* 2018;18:6259–73. <https://doi.org/10.5194/acp-18-6259-2018>.
- [122] Moosmüller H, Chakrabarty RK, Ehlers KM, Arnott WP. Absorption Ångström coefficient, brown carbon, and aerosols: Basic concepts, bulk matter, and spherical particles. *Atmos Chem Phys* 2011;11:1217–25. <https://doi.org/10.5194/acp-11-1217-2011>.
- [123] Corbin JC, Czech H, Massabò D, de Mongeot FB, Jakobi G, Liu F, et al. Infrared-absorbing carbonaceous tar can dominate light absorption by marine-engine exhaust. *NPJ Clim Atmos Sci* 2019;2:12. <https://doi.org/10.1038/s41612-019-0069-5>.

- [124] Corbin JC, Moallemi A, Liu F, Gagné S, Olfert JS, Smallwood GJ, et al. Closure between particulate matter concentrations measured ex situ by thermal–optical analysis and in situ by the CPMA–electrometer reference mass system. *Aerosol Science and Technology* 2020;1293–309. <https://doi.org/10.1080/02786826.2020.1788710>.
- [125] Cambustion. UDAC Mk2. 2024.
- [126] Symonds JPR, Reavell KSJ, Olfert JS. The CPMA-electrometer system - A suspended particle mass concentration standard. *Aerosol Science and Technology* 2013;47. <https://doi.org/10.1080/02786826.2013.801547>.
- [127] Sipkens TA, Johnson T, Nishida R, Smallwood GJ, Corbin JC. Technical note: Simplified approaches to estimate the output of particle mass analyzers paired with unipolar chargers. *J Aerosol Sci* 2023;173:106195. <https://doi.org/10.1016/j.jaerosci.2023.106195>.
- [128] Krishnamoorthy K, Veerapandian M, Yun K, Kim SJ. The chemical and structural analysis of graphene oxide with different degrees of oxidation. *Carbon N Y* 2013;53:38–49. <https://doi.org/10.1016/j.carbon.2012.10.013>.
- [129] Wang H, Hu YH. Effect of oxygen content on structures of graphite oxides. *Ind Eng Chem Res* 2011;50:6132–7. <https://doi.org/10.1021/ie102572q>.
- [130] Sheehan MJ, Peters TM, Cena L, O’Shaughnessy PT, Gussman RA. Generation of nanoparticles with a nebulizer-cyclone system. *Aerosol Science and Technology* 2009;43:1091–8. <https://doi.org/10.1080/02786820903173687>.
- [131] Zangmeister CD. Preparation and evaluation of graphite oxide reduced at 220°C. *Chemistry of Materials* 2010;22:5625–9. <https://doi.org/10.1021/cm102005m>.
- [132] Liao Y, Li Z, Fatima, Xia W. Size-dependent structural behaviors of crumpled graphene sheets. *Carbon N Y* 2021;174:148–57. <https://doi.org/10.1016/j.carbon.2020.12.006>.
- [133] Cranford SW, Buehler MJ. Packing efficiency and accessible surface area of crumpled graphene. *Phys Rev B Condens Matter Mater Phys* 2011;84:205451. <https://doi.org/10.1103/PhysRevB.84.205451>.
- [134] Rawat VK, Buckley DT, Kimoto S, Lee MH, Fukushima N, Hogan CJ. Two dimensional size-mass distribution function inversion from differential mobility analyzer-aerosol particle mass analyzer (DMA-APM) measurements. *J Aerosol Sci* 2016;92:70–82. <https://doi.org/10.1016/j.jaerosci.2015.11.001>.
- [135] Knutson EO, Wmby KT. Aerosol classification by electric mobility: apparatus, theory, and applications. *J Aerosol Sci* 1975;6:443–51. [https://doi.org/10.1016/0021-8502\(75\)90060-9](https://doi.org/10.1016/0021-8502(75)90060-9).
- [136] Song Y, Pei X, Liu H, Zhou J, Wang Z. Characterization of tandem aerosol classifiers for selecting particles: implication for eliminating the multiple charging effect. *Atmos Meas Tech* 2022;15:3513–26. <https://doi.org/10.5194/amt-15-3513-2022>.
- [137] Wiedensohler A. An approximation of the bipolar charge distribution for particles in the submicron size range. *J Aerosol Sci* 1988;19:387–9. [https://doi.org/10.1016/0021-8502\(88\)90278-9](https://doi.org/10.1016/0021-8502(88)90278-9).
- [138] Yang M, Howell SG, Zhuang J, Huebert BJ. Atmospheric Chemistry and Physics Attribution of aerosol light absorption to black carbon, brown carbon, and dust in China-interpretations of atmospheric measurements during EAST-AIRE. *Atmos Chem Phys* 2009;9:2035–50. <https://doi.org/10.5194/acp-9-2035-2009>.

- [139] Musikhin S, Talebi-Moghaddam S, Corbin JC, Smallwood GJ, Schulz C, Daun KJ. Crumpled few-layer graphene: Connection between morphology and optical properties. *Carbon N Y* 2021;182:677–90. <https://doi.org/10.1016/j.carbon.2021.06.052>.
- [140] Li D, Müller MB, Gilje S, Kaner RB, Wallace GG. Processable aqueous dispersions of graphene nanosheets. *Nat Nanotechnol* 2008;3:101–5. <https://doi.org/10.1038/nnano.2007.451>.
- [141] Schöche S, Hong N, Khorasaninejad M, Ambrosio A, Orabona E, Maddalena P, et al. Optical properties of graphene oxide and reduced graphene oxide determined by spectroscopic ellipsometry. *Appl Surf Sci* 2017;421:778–82. <https://doi.org/10.1016/j.apsusc.2017.01.035>.
- [142] Zangmeister CD, You R, Lunny EM, Jacobson AE, Okumura M, Zachariah MR, et al. Measured in-situ mass absorption spectra for nine forms of highly-absorbing carbonaceous aerosol. *Carbon N Y* 2018;136:85–93. <https://doi.org/10.1016/j.carbon.2018.04.057>.
- [143] Acik M, Lee G, Mattevi C, Pirkle A, Wallace RM, Chhowalla M, et al. The role of oxygen during thermal reduction of graphene oxide studied by infrared absorption spectroscopy. *Journal of Physical Chemistry C* 2011;115:19761–81. <https://doi.org/10.1021/jp2052618>.
- [144] Sieradzka M, Ślusarczyk C, Fryczkowski R, Janicki J. Insight into the effect of graphite grain sizes on the morphology, structure and electrical properties of reduced graphene oxide. *Journal of Materials Research and Technology* 2020;9:7059–67. <https://doi.org/10.1016/j.jmrt.2020.05.026>.
- [145] Dao TD, Jeong HM. Graphene prepared by thermal reduction-exfoliation of graphite oxide: Effect of raw graphite particle size on the properties of graphite oxide and graphene. *Mater Res Bull* 2015;70:651–7. <https://doi.org/10.1016/j.materresbull.2015.05.038>.
- [146] Micromeritics. Gemini ® VII 2390. 2016.
- [147] ASTM. Test Method for Carbon Black Total and External Surface Area by Nitrogen Adsorption. West Conshohocken, PA: ASTM International; 2021. <https://doi.org/10.1520/D6556-21>.
- [148] Pop E, Varshney V, Roy AK. Thermal properties of graphene: Fundamentals and applications. *MRS Bull* 2012;37:1273–81. <https://doi.org/10.1557/mrs.2012.203>.
- [149] Al-Douri Y. Graphene, Nanotubes and Quantum Dots-Based Nanotechnology. 1st ed. Kidlington: Woodhead Publishing; 2022.
- [150] Zhao B, Liu P, Jiang Y, Pan D, Tao H, Song J, et al. Supercapacitor performances of thermally reduced graphene oxide. *J Power Sources* 2012;198:423–7. <https://doi.org/10.1016/j.jpowsour.2011.09.074>.
- [151] Alazmi A, El Tall O, Rasul S, Hedhili MN, Patole SP, Costa PMFJ. A process to enhance the specific surface area and capacitance of hydrothermally reduced graphene oxide. *Nanoscale* 2016;8:17782–7. <https://doi.org/10.1039/c6nr04426c>.
- [152] McAllister MJ, Li JL, Adamson DH, Schniepp HC, Abdala AA, Liu J, et al. Single sheet functionalized graphene by oxidation and thermal expansion of graphite. *Chemistry of Materials* 2007;19:4396–404. <https://doi.org/10.1021/cm0630800>.
- [153] Tene T, Guevara M, Benalcázar Palacios F, Morocho Barrionuevo TP, Vacacela Gomez C, Bellucci S. Optical properties of graphene oxide. *Front Chem* 2023;11:1214072. <https://doi.org/10.3389/fchem.2023.1214072>.
- [154] Everett DH. Basic Principles of Colloid Science. London: The Royal Society of Chemistry; 1988.

- [155] ThermoFisher Scientific. Evolution 300 and Evolution 600 UV-Vis Spectrophotometers. 2007.
- [156] Yon J, Lemaire R, Therssen E, Desgroux P, Coppalle A, Ren KF. Examination of wavelength dependent soot optical properties of diesel and diesel/rapeseed methyl ester mixture by extinction spectra analysis and LII measurements. *Appl Phys B*, vol. 104, Springer Verlag; 2011, p. 253–71. <https://doi.org/10.1007/s00340-011-4416-4>.
- [157] Stagg BJ, Charalampopoulos TT. Refractive Indices of Pyrolytic Graphite, Amorphous Carbon, and Flame Soot in the Temperature Range 25 ° to 600°C. *Combust Flame* 1993;94:381–96. [https://doi.org/10.1016/0010-2180\(93\)90121-I](https://doi.org/10.1016/0010-2180(93)90121-I).
- [158] Lee SC, Tien CL. Optical constants of soot in hydrocarbon flames. *Symposium (International) on Combustion* 1981;18. [https://doi.org/10.1016/S0082-0784\(81\)80120-8](https://doi.org/10.1016/S0082-0784(81)80120-8).
- [159] Nasehnia F, Mohammadpour Lima S, Seifi M, Mehran E. First principles study on optical response of graphene oxides: From reduced graphene oxide to the fully oxidized surface. *Comput Mater Sci* 2016;114:112–20. <https://doi.org/10.1016/j.commatsci.2015.12.010>.
- [160] Politano GG, Versace C. Electrical and Optical Characterization of Graphene Oxide and Reduced Graphene Oxide Thin Films. *Crystals (Basel)* 2022;12. <https://doi.org/10.3390/cryst12091312>.
- [161] Smith N V. Classical generalization of the Drude formula for the optical conductivity. *Phys Rev B Condens Matter Mater Phys* 2001;64. <https://doi.org/10.1103/PhysRevB.64.155106>.
- [162] Jung E, Lee S, Roh S, Hwang E, Lee J, Lee H, et al. Optical properties of graphite oxide and reduced graphite oxide. *J Phys D Appl Phys* 2014;47. <https://doi.org/10.1088/0022-3727/47/26/265306>.
- [163] Su Q, Pang S, Alijani V, Li C, Feng X, Müllen K. Composites of graphene with large aromatic molecules. *Advanced Materials* 2009;21:3191–5. <https://doi.org/10.1002/adma.200803808>.
- [164] Korkh Y V., Rinkevich AB, Klepikova AS, Tolmacheva EA, Pankrushina EA. Characterization of CVD-synthesized graphene films transferred on different substrates using the scanning probe microscopy electrical techniques. *Physica E Low Dimens Syst Nanostruct* 2022;138. <https://doi.org/10.1016/j.physe.2021.115101>.
- [165] Yan L, Punckt C, Aksay IA, Mertin W, Bacher G. Local voltage drop in a single functionalized graphene sheet characterized by Kelvin probe force microscopy. *Nano Lett* 2011;11:3543–9. <https://doi.org/10.1021/nl201070c>.
- [166] Quay B, Lee T-W, Ni T, Santoro RJ. Spatially Resolved Measurements of Soot Volume Fraction Using Laser-Induced Incandescence. *Combust Flame* 1994;97:384–92. [https://doi.org/10.1016/0010-2180\(94\)90029-9](https://doi.org/10.1016/0010-2180(94)90029-9).
- [167] Rabello de Castro R, Figueira da Silva LF. Soot Volume Fraction and Temperature of Laminar Non-Premixed Ethylene-Air Flame, *Associação Brasileira de Engenharia e Ciências Mecânicas - ABCM*; 2019. <https://doi.org/10.26678/abcm.cobem2019.cob2019-0468>.
- [168] Yazıcı Hİ, Schulz C, Daun KJ. Feasibility of online optical diagnostics during gas-phase synthesis of few-layer graphene based on elastic light scattering measurements. *J Aerosol Sci* 2025;184. <https://doi.org/10.1016/j.jaerosci.2024.106497>.
- [169] Huber FJT, Altenhoff M, Will S. A mobile system for a comprehensive online-characterization of nanoparticle aggregates based on wide-angle light scattering and laser-induced incandescence. *Review of Scientific Instruments* 2016;87. <https://doi.org/10.1063/1.4948288>.

- [170] Goulay F, Schrader PE, Lopez-Yglesias X, Michelsen HA. A data set for validation of models of laser-induced incandescence from soot: Temporal profiles of LII signal and particle temperature. *Appl Phys B* 2013;112:287–306. <https://doi.org/10.1007/s00340-013-5504-4>.
- [171] Köylü UO, Faeth GM. Spectral Extinction Coefficients of Soot Aggregates From Turbulent Diffusion Flames. *J Heat Transfer* 1996;118:415.

Appendices

This section of the thesis provides supplemental information referenced in the thesis chapters. Appendix A details the calibration processes for the TiRe-LII apparatus and the LOSA apparatus. Appendix B details the correction and statistical analysis applied to the data in Chapter 5.

Appendix A

Calibration Procedures

A.1 TiRe-LII relative calibration

For this work, the TiRe-LII system was calibrated for relative intensity as opposed to absolute intensity. Absolute intensity calibration refers to calibrating the system for exact intensity values, whereas relative intensity calibration ensures the intensities of each component. Absolute intensity calibration is not required when deriving the pyrometric temperature of the particle; instead, relative calibration between the photomultiplier tubes (PMTs) is needed to ensure the intensities align. Additionally, calibration of each optical component and the PMT responses is needed. This was carried out by another student, Stephen Robinson-Enebeli, and is presented in his thesis [74]. The same optical equipment and PMTs were used in this study and the calibration results reported by Robinson-Enebeli were used. However, the system was modified to a four-colour PMT system from a three-colour PMT system to improve accuracy. Due to the modification of the system, new calibration constants were determined for relative sensitivity. The following section details the calibration procedure performed.

A.1.1 Calibration procedure

The calibration procedure followed the approach defined by Mansmann et al. [94]. Each PMT was calibrated for sensitivity using a calibration light source and for gain across multiple gain levels. The procedure involved using a well-defined light source to direct light into the detection system. The PMT intensities were then calibrated using the defined spectral light intensity of the light source.

Two well-defined light sources were compared and tested to determine the ideal calibration constants: a halogen-tungsten light source (SLS201L/M, Thorlabs) and a laser-driven light source (LDLS, EQ-99X-FC-S, Energetiq). These light sources were chosen due to their differences in applicable range. The halogen-tungsten light source produced relatively lower light intensity compared to the LDLS.

Consequently, it provided calibration values only at higher gains (650 to 950), whereas the LDLS could provide calibration values across all gains.

The calibration setup involved directing light produced by the light source into a fiber optic cable, which led to an integrating sphere ($\varnothing 2''$ IS200-4, Thorlabs) designed to create a uniform light source. The integrating sphere was positioned at probe volume, as shown in Figure 3-6, eliminating the need for further realignment.

Photomultiplier tubes are highly sensitive; therefore, care must be taken to prevent damage. As the PMTs were connected to an oscilloscope with a 50Ω coupling, precautions were taken according to Table A-1 to ensure that the PMT output voltages did not exceed the recommended maximum output voltages.

Table A-1 PMT maximum output voltage ratings

Illumination Time	Max Output Voltage (50Ω coupling)	Max Repetition Frequency
DC	5 mV	-
100 μ s	50 mV	100 Hz
1 μ s	500 mV	10 Hz
10 ns	5 V	1 Hz

To prevent damage to the PMT, the illumination time is reduced using an optical chopper. The optical chopper is placed between the integrating sphere and collection optics, increasing the maximum repetition frequency and subsequently allowing a higher voltage readout. Additionally, it creates distinct periods for the background signal and the combined background-plus-light signal. This enables the light signal to be determined by subtracting the background signal from the combined signal. Figure A-1 and Figure A-2 show a schematic and physical image of the calibration setup, respectively.

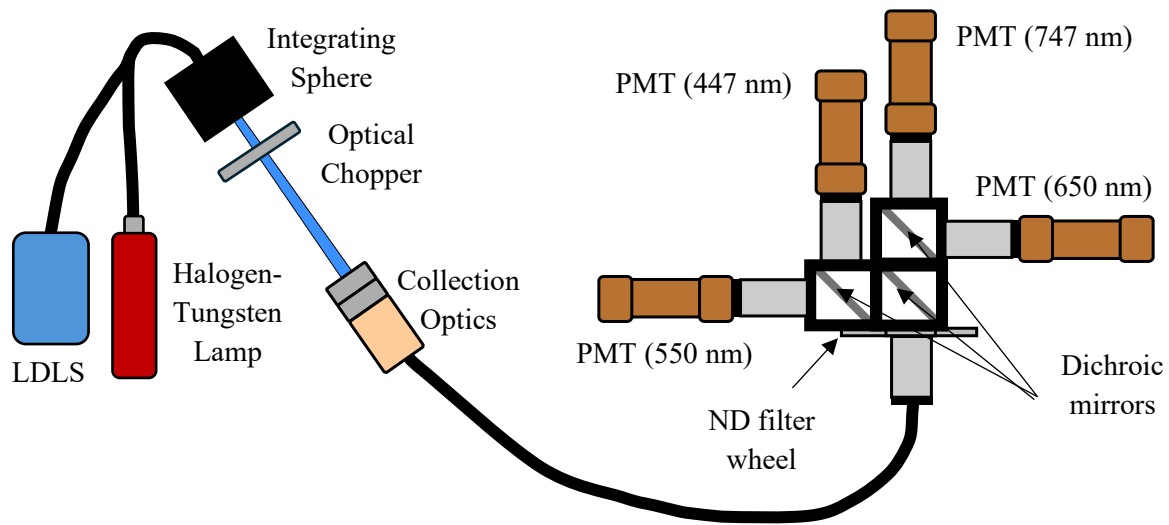


Figure A-1: Schematic of calibration setup

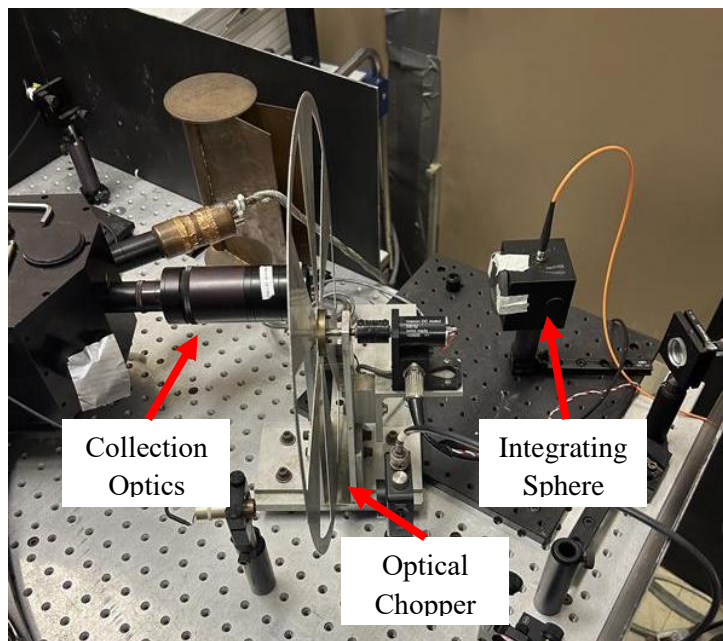


Figure A-2: Physical image of calibration setup

For both light sources, the calibration factors were determined using the same procedure. The primary objective was to establish a relationship between the induced voltage on a PMT and a known amount of incident irradiation, as well as to examine how this relationship varies across different PMT

gains. The irradiance (E_i^{ref}) incident on the i th PMT within a wavelength bandwidth $\Delta\lambda$ can be computed as follows [94]:

$$E_i^{\text{ref}} = \int_{\Delta\lambda_i} E^{\text{ref}}(\lambda) d\lambda \quad (\text{A.1})$$

where E^{ref} is the intensity of the light source. The light source has a well-defined intensity spectrum, allowing for an easy derivation of this value. A voltage (V_i^{meas}) will be induced on the PMT that can be used to derive an intensity calibration factor (D_i) as defined by:

$$D_i = \frac{\tau_i E_i^{\text{ref}}}{V_i^{\text{meas}}} \quad (\text{A.2})$$

where τ_i is the transmission for the i th PMT of the neutral density (ND) filter used. Subsequently, D_i can be normalized against a single PMT to derive a relative intensity calibration factor (D_i^{rel}).

The voltage applied on the voltage divider circuit of a PMT is controlled by gain controllers. This allows the PMT to measure a wide range of light levels, thereby increasing the dynamic range. However, although the general relationship between voltage gain and the induced PMT signal is well defined, a correction must be applied to derive the exact relationship due to variations in components. This correction can be achieved by determining a gain correction factor (G_i), defined as:

$$G_i(V_i^{\text{gain}}) = \left(\frac{V_i^{\text{gain}}}{V_i^{\text{gain,ref}}} \right)^{A_i} \quad (\text{A.3})$$

where V_i^{gain} is the gain voltage for an i th PMT, $V_i^{\text{gain,ref}}$ is a reference gain voltage at an i th PMT, and $A_{g,i}$ is a coefficient that can be found by solving a weighted minimization:

$$A_{g,i} = \operatorname{argmin}_{A_{g,i}} \left\| \frac{V_i^{\text{meas}} - V_i^{\text{meas,ref}} \left(\frac{V_i^{\text{gain}}}{V_i^{\text{gain,ref}}} \right)^{A_{g,i}}}{\sigma_i^{\text{gain}}} \right\|^2 \quad (\text{A.4})$$

Using the gain correction factor and relative intensity calibration factor, at the i th PMT with an applied voltage (V_i^{gain}), the experimental signal ($J_{\text{exp},i}$) can be adjusted as follows:

$$J_{\text{corr},i} = D_i G_i (V_i^{\text{gain}}) J_{\text{exp},i} \quad (\text{A.5})$$

To simplify the description in the remainder of the section, the four PMTs will now be denoted according to Table A-2.

Table A-2: PMT naming convention

PMT Name	PMT 1	PMT 2	PMT 3	PMT 4
Spectral bandwidth	431 to 463 nm	512 to 577 nm	600 to 690 nm	722 to 782 nm

Due to the lower intensity of the halogen-tungsten lamp, calibration could not be performed across the whole gain range (0 to 1000 gain). Instead, it was conducted from 650 to 900 in increments of 25 gain for PMT 1 and PMT 2, while for PMT 3 and PMT4, calibration was performed from 500 to 750 in increments of 25. The change in measured voltage as a function of gain for PMT1 is shown in Figure A-3. The derived A_i and D_i^{rel} , normalized by PMT1, for each PMT is shown in Table A-3.

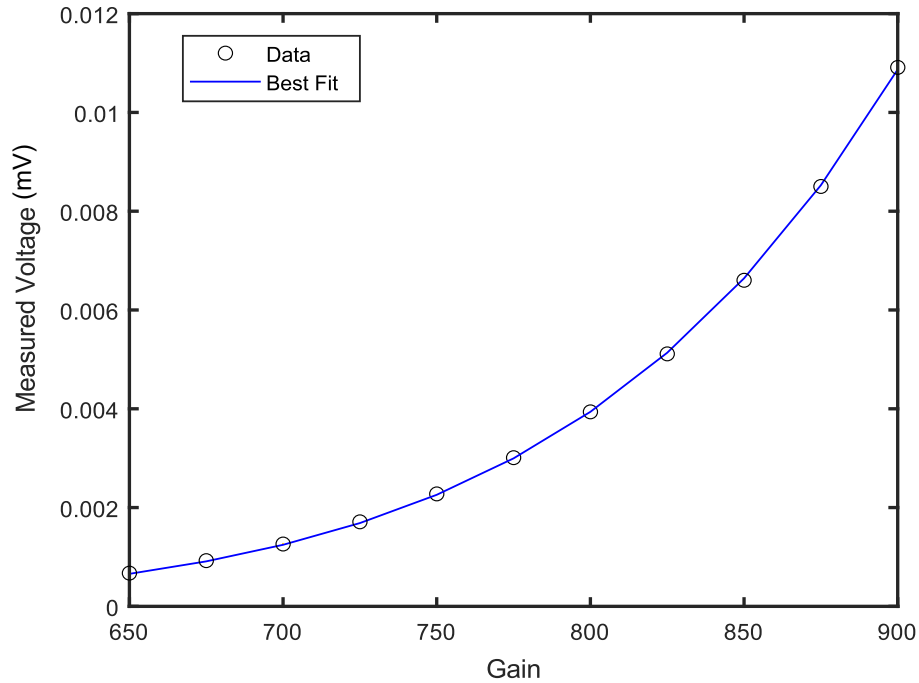


Figure A-3: Measured voltage vs gain for PMT 1 – Halogen-Tungsten lamp

Table A-3: Calibration constants derived at each PMT – Halogen-Tungsten lamp

PMTS	PMT1	PMT2	PMT3	PMT4
A_i	8.5492	6.8132	6.9645	7.2768
D_i^{rel}	1	6.2665	7.2036	5.1968

With the LDLS, the light intensity was much higher, allowing gains from 250 to 950 to be characterized. However, this required the use of ND filters at higher gains, which introduced discrepancies in the gain-to-voltage relationship, as shown in Figure A-4. These discrepancies resulted from high light intensity, which caused non-linearity in the PMT response [95]. To generate an applicable correction constant for all ND filters, the effective calibration range was restricted to gains between 250 to 500. The gain was measured in increments of 25 gain at all ND filters. The change in measured voltage as a function of gain for PMT1 is shown in Figure A-5. Compared to the halogen-tungsten lamp, the fit is less accurate in describing the relationship, which is assumed to be due to the high intensity of the LDLS.

Table A-4: Calibration constants derived at each PMT – LDLS

PMTS	PMT1	PMT2	PMT3	PMT4
A_i	9.8022	6.6047	7.3163	7.1171
D_i^{rel}	1	0.8914	0.3424	0.3047

A commonly used method to validate the derived calibration constants is to measure the maximum pyrometric temperature of soot from a co-flow laminar burner over a wide range of fluences. It is expected that the temperature will plateau at the sublimation temperature of carbon dimers (C_2) (4456 K) [170]. The subsequent section will detail the design and fabrication of a Gülder burner used for calibration.

A.1.2 Gülder burner fabrication

To validate the derived calibration constants, a Gülder burner was constructed. A Gülder burner is a standard device commonly used for laser-induced incandescence (LII) calibration [41]. The design of the Gülder burner followed specifications detailed in Rabello et al. [167]. The burner featured a cylindrical body with an outer diameter of 101.6 mm (4 inches) and an inner diameter of 88.90 mm (3.5 inches). The overall height of the cylinder was 127 mm (5 inches), with an additional 25.40 mm (1 inches) tall and 25.40 (1 inches) wide cylinder attached to the bottom. Two protruding lips, measuring 86.36 mm (3.4 inches) and 83.82 mm (3.3 inches) in diameter, were positioned at heights of 88.90 mm (3.5 inches) and 50.80 mm (2 inches), respectively. A \varnothing 3/8-inch NPT opening was drilled on the side of the burner, while a \varnothing 1/2-inch NPT opening was drilled through the smaller cylinder. Figure A-6 presents a technical drawing of the burner.

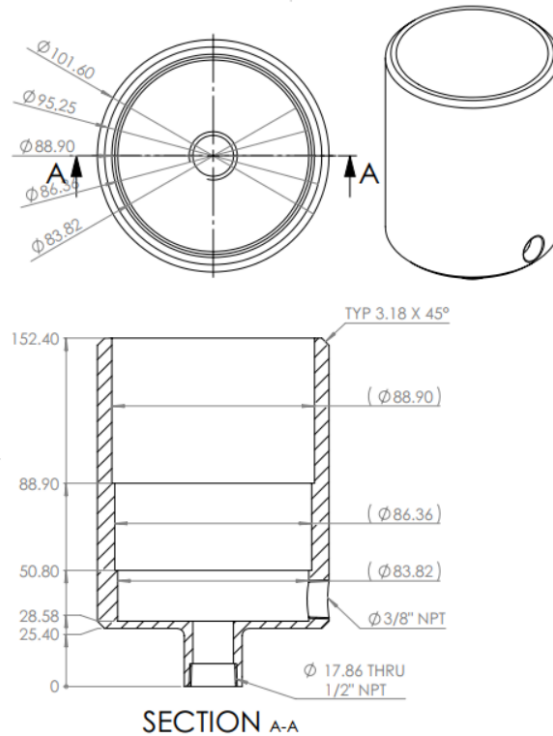


Figure A-6: Technical drawing of the burner

The 3/8-inch and 1/2-inch openings serve to connect to burner to air and ethylene gas lines, respectively. A 12.70 mm (0.5-inch) steel pipe, connected to an ethylene cylinder, passes through the Ø 1/2-inch NPT opening and attached so that it sits in line with the top of the large cylinder. A compressed air line is attached to the burner via the 3/8-inch NPT opening. To stabilize the airflow around the central pipe, a combination of 5 mm stainless steel balls and a steel mesh are used. The lips at 2 inches and 3.5 inches each hold a circular steel foam with the sections between them filled with stainless steel balls. A wireframe mesh is attached to the 3/8-inch NPT opening to prevent any balls from entering the air line. This design allows an ethylene stream to flow out of the center of the steel pipe, while the surrounding air is directed around it in a stable manner, stabilizing both the ethylene stream and the resulting flame. A stable, consistent flame is produced by igniting the ethylene stream. Figure A-7 shows a physical image of the burner.

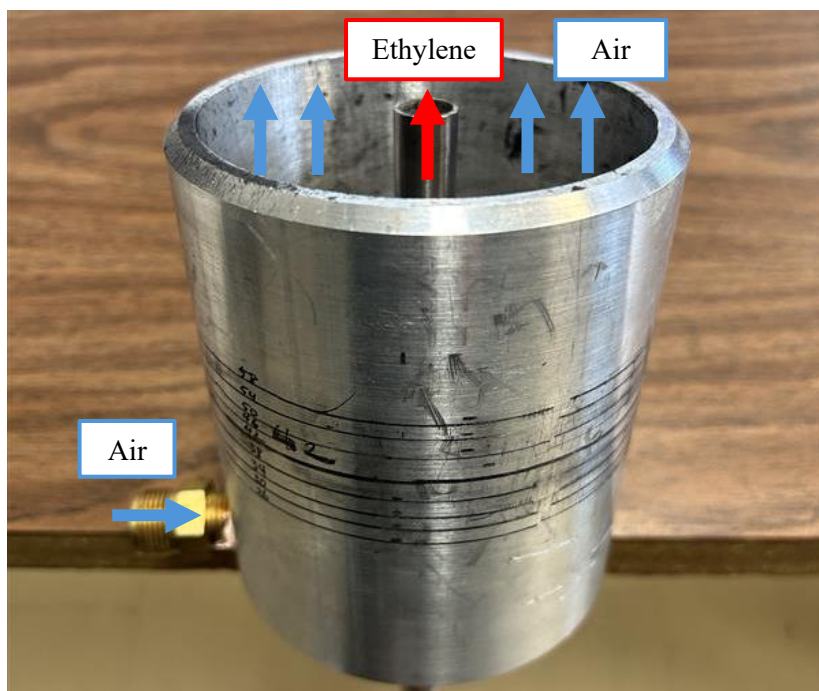


Figure A-7: Physical image of Gülder Burner

For calibration, a set of standard flow rates and operating conditions are followed [41,167]. The air and ethylene flow rates are set to 273 slpm and 0.2 slpm, respectively, using two mass flow controllers (5800 Series E&I, Brooks). This setup produces a flame with a stable, visible height of 65 mm. The burner, similar to the integrating sphere in Figure A-1, replaces the probe volume in the TiRe-LII excitation system. The calibration is performed at atmospheric pressure and room temperature, with the laser and collection optics focused on the center of the flame, 42 mm above the tip of the nozzle (HAB, height above burner). The resulting incandescent signals can then be analyzed and compared to results from the literature.

A.1.3 Calibration constants validation

To validate the calibration constants derived from the halogen-tungsten lamp and LDLS, TiRe-LII experiments were conducted using the Gülder burner across 12 different fluences, ranging from 0.075 J/cm² to 0.350 J/cm² in increments of 0.025 J/cm². This range was chosen based on the limitations of the

system and does not match the range presented in Goulay et al. [170]. However, as shown in Figure A-8, the characteristic plateau of soot is observed within the studied region. This plateau corresponds to the sublimation temperature of carbon dimers (C_2) (4456 K). At this temperature, the mass loss due to vaporization leads to a stabilization of the maximum temperature. In Figure A-8, the gray line represents results derived from studies using a 1064 nm laser and a refractive index given by Köylü et al. [171]. This will be the basis of the comparison.

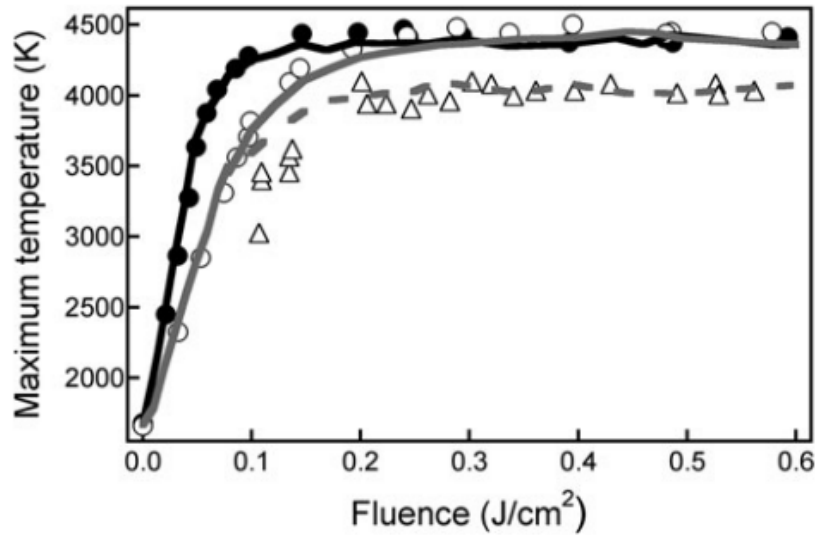


Figure A-8: Maximum temperature vs fluence: Gray solid line and open circles are studies at 1064 nm [170]

For this study, a gain of 330 was used for PMT 1 and PMT 2 and a gain of 300 for PMT 3 and PMT 4, with stacked ND filters at 57% transmissivity and 11% transmissivity, respectively. The ND filter constants used were derived by Robinson-Enebeli [74] and are shown in Table A-5.

Table A-5: ND filter constants

ND Filter	PMT 1	PMT 2	PMT 3	PMT 4
57%	0.5934	0.5846	0.5648	0.5490
11%	0.1376	0.1193	0.1031	0.0940

The transmissivity (τ_i) for the i th PMT can be found by multiplying the constants at each filter. Using the transmissivity, two sets of calibration constants can be determined based on the Halogen-Tungsten (H-T) lamp and the LDLS. By applying the calibration constants and solving for the pyrometric temperature, following the procedure outlined in Section 2.1.1, the maximum temperature versus fluence plot for both sets of calibration constants can be derived, as shown in Figure A-9. Additionally, the sublimation temperature of carbon dimers (C_2) is also shown as a reference for where the plateau should occur. It can be seen that the calibration constants for the LDLS plateau at much higher maximum temperatures. Additionally, the plateau occurs at a larger fluence than what was observed by Goulay et al. [170]. The difference in plateau temperature and fluence indicates the calibration is not successful in connecting the intensities of the four PMTs.

In contrast, the plateau temperature and fluence match well for the H-T lamp constants. The fluence at which the plateau first appears is approximately 0.25 J/cm^2 , similar to the gray line shown in Figure A-8. Additionally, the plateau temperature is similar, though slightly higher, plateauing around 4650 K. This slight increase can be attributed to the assumption regarding $E(m_\lambda)$. The gray line shown in Figure A-8 is derived using a m_λ derived by Köylü et al. [171], which would cause changes in the pyrometric temperature and lead to differences in plateau temperature. Nonetheless, the close degree of fit in magnitude and plateau fluence indicates that the calibration constants derived from the H-T lamp are accurate. Therefore, the results from the H-T lamp calibration were used throughout this thesis.

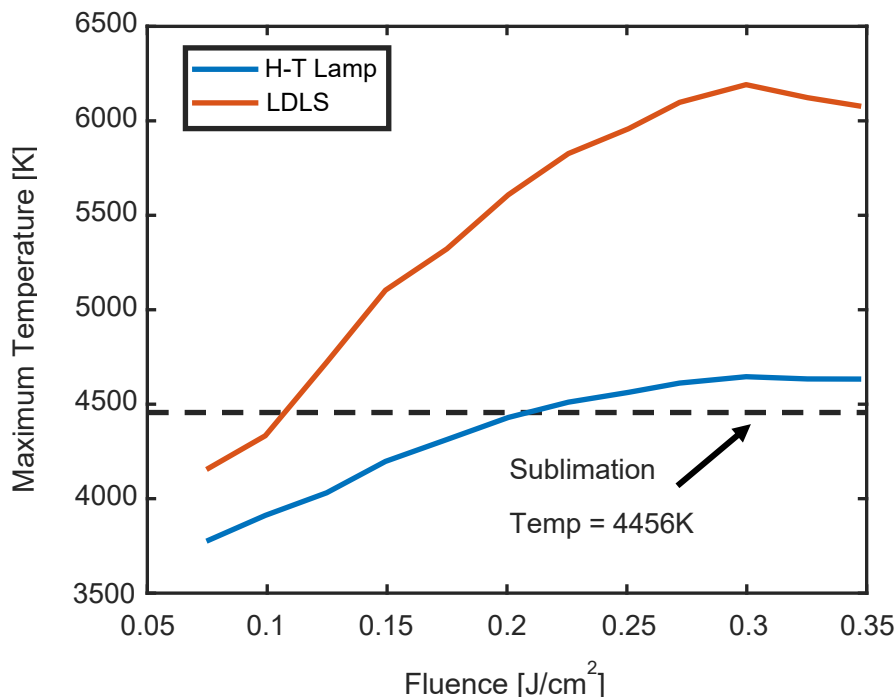


Figure A-9: Maximum temperature vs Fluence: Halogen-Tungsten Lamp vs LDLS

A.2 LOSA calibration

To calibrate the line-of-sight absorption (LOSA) system, a Mercury-Argon pen-ray lamp was used. Pen-ray lamps are light sources with well-defined intensities at specific wavelengths. They are used to calibrate spectrometers and electron-multiplying charge-coupled device (EMCCD) cameras by providing light intensities at sharp wavelength. The pen-ray lamp used in this study, is positioned in front of the spectrometer/EMCCD, and a pixel map is created, as shown in Figure A-10. From the observed intensities, the x-axis of the image can be calibrated by assigning wavelengths to the pixels based on the lamp's defined spectrum. These points are then linearly extrapolated, transforming the x-axis from pixel positions to wavelengths. It is important to note that there is slight curvature in the intensity distribution, indicating that the spectral gratings may cause some intensities to bleed into neighbouring wavelengths. However, this curvature is minor and is subsequently ignored. Consequently, during the LOSA

experiments, the wavelengths are treated as independent, and intensities are averaged over all y-pixels to derive an intensity at each wavelength.

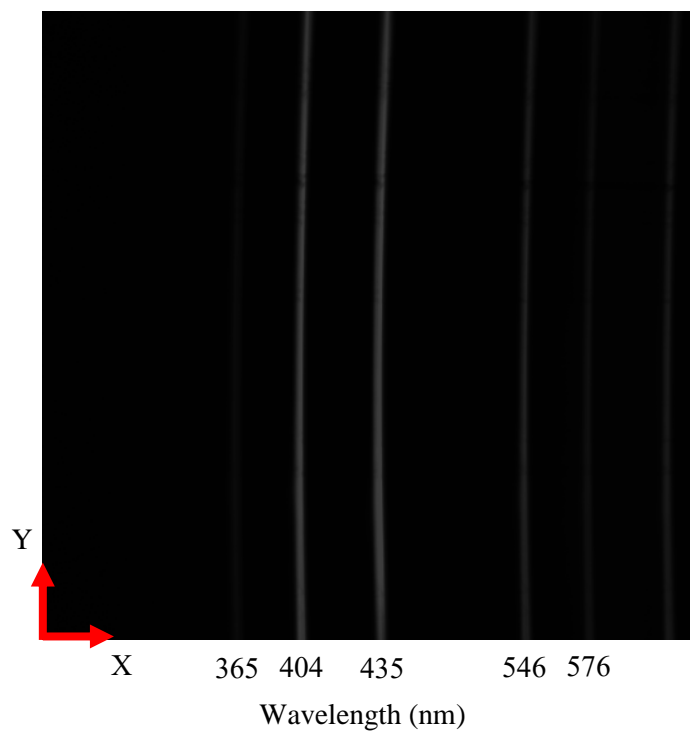


Figure A-10: Pixel image of pen-ray lamp

Appendix B

B.1 Effective density calibration

To derive the effective density (ρ_{eff}) of the graphene oxide (GO) sample, a combined centrifugal particle mass analyzer (CPMA) and scanning mobility particle sizer (SMPS) were used. The calibration of this system was performed using Santovac 5P Diffusion Pump Fluid (Chromatographic Specialties Inc.), a material with a known material density of 1.198 g/cm^3 at $25 \text{ }^\circ\text{C}$. This choice was made because Santovac 5P particles are perfectly spherical, ensuring that their effective density matches their material density allowing any observed deviation to be attributed to inaccuracies in the CPMA and SMPS. The study was carried out at mass-to-charge (m^*) of 0.02 fg, 0.05 fg, 0.1 fg, 0.2 fg, 0.5 fg, 1.0 fg, 2.0 fg, 5.0 fg, 10.0 fg, and 20.0 fg. The experiment was repeated three times, and the average effective density was used. A curve was fitted to the experimental data using a two-term power law fit ($a_s(d_p)^{b_s} + c_s$) with outliers excluded at 0.02 and 0.2 fg, as shown in Figure B-1.

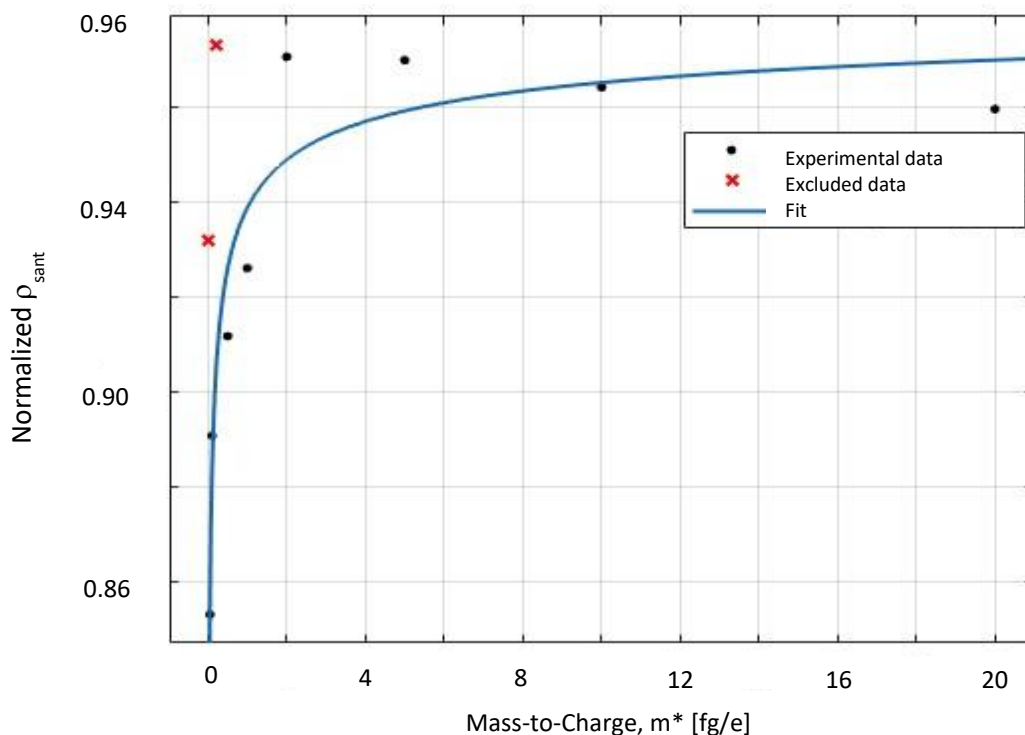


Figure B-1: Fitted Santovac calibration curve

The fit constants derived were $a_s = -0.04965$, $b_s = -0.3288$, and $c_s = 0.9884$. The derived power-law relationship will be used to calibrate the effective density of the GO sample by:

$$\rho_{\text{eff,GO}}^{\text{corr}} = \frac{\rho_{\text{eff,GO}}^{\text{raw}}}{a_s (d_p)^{b_s} + c_s} \quad (8.6)$$

B.2 Vertical error bar determination

The effective density study was run three times; due to the low number of runs, a standard deviation could not be reliably calculated. Instead, the variance in the effective density was conservatively accounted for by taken the maximum and minimum effective density from the three runs. Additionally, the error found from the power-law fit for the Santovac calibration was determined by taking the variance of the dataset from the fit. The total variance was found by summing the two variances. The vertical error bars represent the total variance in Figure 5-3.